ULB Université Libre de Bruxelles

Faculté des Sciences Appliquées

MR-fluid brake design and its application to a portable muscular rehabilitation device

More Thomas AVRAAM

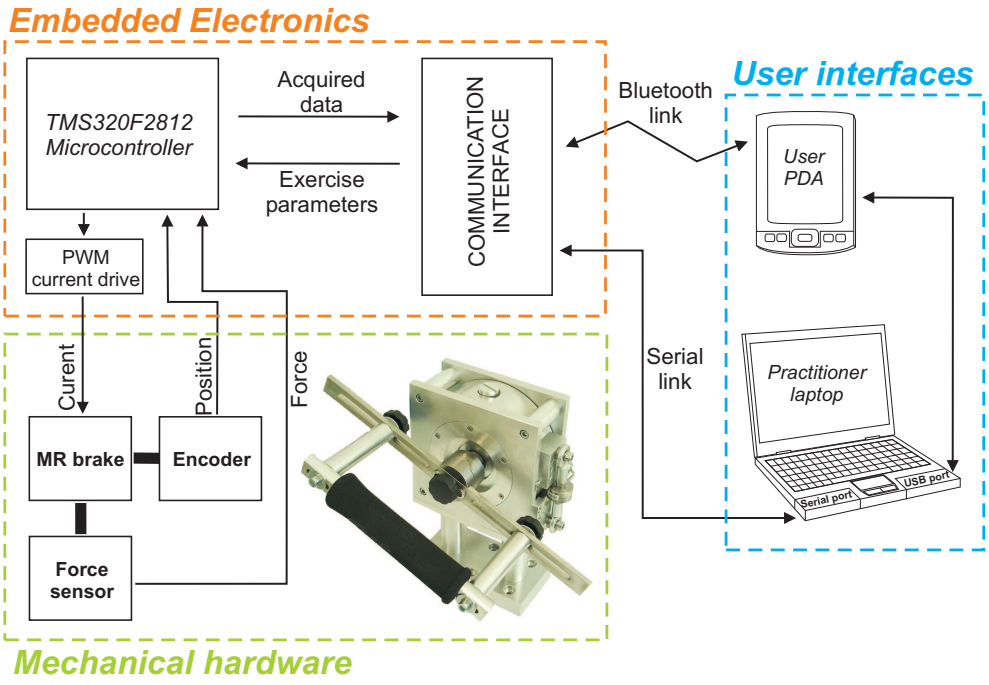

Thesis submitted in candidature for the degree of Doctor in Engineering Sciences

November 2009

Active Structures Laboratory
Department of Mechanical Engineering and Robotics

Jury

President : Prof. Alain Delchambre (ULB)

Supervisor : Prof. André Preumont (ULB)

Members :

Dr. J. David Carlson (LORD Corporation - USA)

Prof. Johan Gyselinck (ULB)

Prof. Maurice Hinsenkamp (ULB)

Prof. Steen Krenk (Technical University - Denmark)

Prof. Hendrik Van Brussel (KUL - Leuven)

Acknowledgements

First of all, I would like to thank my supervisor, Professor André Preumont, for giving me the opportunity to join the Active Structures Laboratory. The five years I spent there were very enriching under many aspects. Without his permanent support, many advice, suggestions and inspiring ideas, this work would not have reached the level it did.

My gratitude also goes to my colleagues and friends of the ASL for their helpful technical support and encouragements. I owe a lot to Iulian Romanescu and Mihaita Horodinca whose expertise and manufacturing skills highly contributed to the development and successful implementation of the various MR-brake prototypes. I also wish to thank Pierre Letier for his help and the many discussions we had about technical aspects of this work.

I also acknowledge the help of Micromega dynamics and, in particular, Jean-Philippe Verschueren for his advice and patience for the implementation of the embedded electronics. A particular thanks also goes to all my master students who participated in the development of the various prototypes throughout these five years. I also would like to thank Dr Böse from the Fraunhofer institute ISC for kindly providing the MR-fluid used in this work.

I am also grateful to Alain Weymeersch as well as the other members of the ULB Technology Transfer Office for their help in identifying the market and in writing the patent of the rehabilitation device. My thanks also go to the team of EEBIC for their support while conducting interviews of potential users. I also would like to thank Pascal Remy for helping me to understand the needs of physiotherapists and initiating me to isokinetics and muscular rehabilitation.

Last but not least, I would like to thank all my friends and family, and especially Sophie, for their trust, endless support and encouragements throughout all these years.

This work was supported by the Walloon region in the framework of the *FIRST spin-off* program (*MR-tech* project, contract number 616358). The early MR-brake prototypes were developed within the ESA contract *Exostation* (contract 18408/04/NL/CP) on haptic feedback.

Abstract

Many devices are available on the market for the evaluation and rehabilitation of patients suffering from muscular disorders. Most of them are small, low-cost, passive devices based on the use of springs and resistive elements and exhibit very limited (or even not any) evaluation capabilities; extended muscular force evaluation is only possible on stationary, expensive, multi-purpose devices, available only in hospitals, which offer many exercise modes (e.g. isokinetic mode) that are not available on other devices.

The objective of this thesis is to make the functionalities currently only implemented on bulky multi-purpose devices available at a lower cost and in a portable fashion, enabling their use by a large number of independent practitioners and patients, even at home (tele-medecine applications).

In order to achieve this goal, a portable rehabilitation device, using a magneto-rheological fluid brake as actuator, has been designed. This particular technology was selected for its high level of compactness, simple mechanical design, high controllability, smooth and safe operation. The first part of this thesis is devoted to the design of MR-fluid brakes and their experimental validation. The second part is dedicated to the design of the rehabilitation device and the comparison of its performances with a commercial multi-purpose device (CYBEX).

Contents

Chapter 1

Introduction

1.1 Muscular rehabilitation devices: market overview

The market of muscular rehabilitation devices is composed of three major categories (Figure 1.1), described in further details in the following subsections.

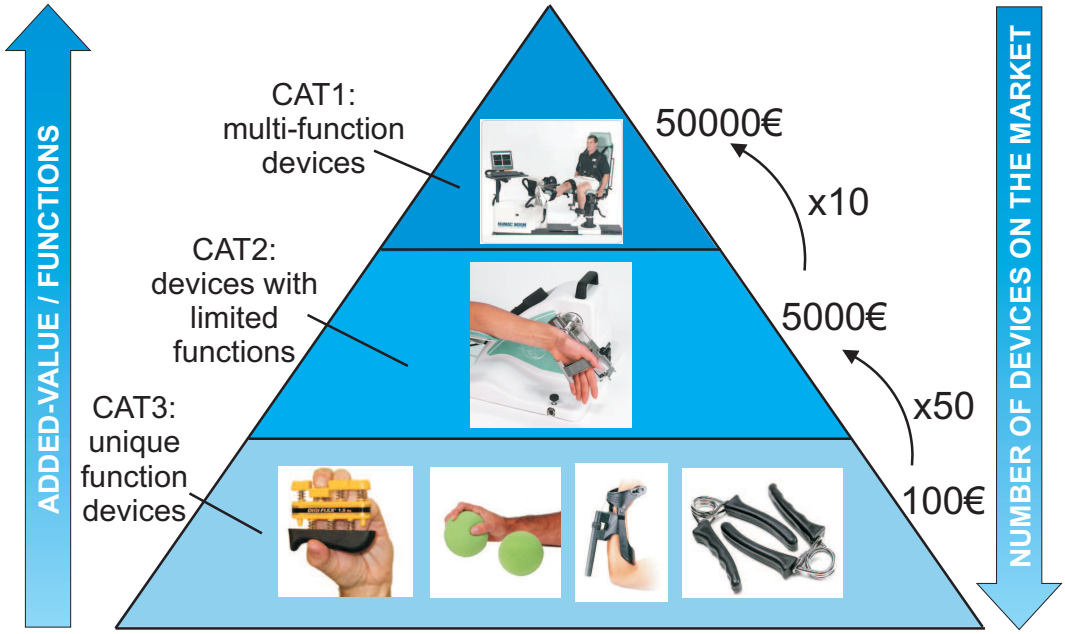

Figure 1.1: Overview of rehabilitation devices market

1.1.1 Category 1: Multi-function devices

These are computer controlled devices that can be used for muscular evaluation and exercise of almost any body joint. Data acquired during evaluation is displayed to the patient, to increase his motivation, and recorded for further analysis by the practitioner. All these devices offer a large number of exercise modes.

Multi-function devices are large, bulky and not portable. Furthermore, they exhibit low repeatability for the evaluation of small body joints (such as wrist) and a lack of precision in measurements (Chan and Maffulli, 1996) (Leclerq, 1999). Finally, changing the configuration of the device for the evaluation and exercise of one joint to another is highly time-consuming. Such devices are thus not suited for small practices where two successive patients rarely suffer from disfunction of the same joint of the body.

Major players in this category include CSMI with the Humac Norm (former CYBEX), BIODEX, BTE Technologies with the Primus and CONTREX (Figure 1.2). All these manufacturers are based in the US, except for CONTREX which is a Swiss company. These devices are priced between 45000 and 90000 euros, depending on the accessories, making them affordable only for clinics and hospitals.

Figure 1.2: Commercial multi-function devices

The market of multifunction devices is more or less saturated. In 1998, the total number of multi-function devices in service in the USA was about 3500 (Frost and Sullivan, 1998). In Europe, the distribution of devices is not equal between countries due to cultural differences, economic disparities and different reimbursement policies. Figure 1.3 gives an overview of the number of multi-function devices in operation in each European country. The total number of devices is similar to the one on the US market.

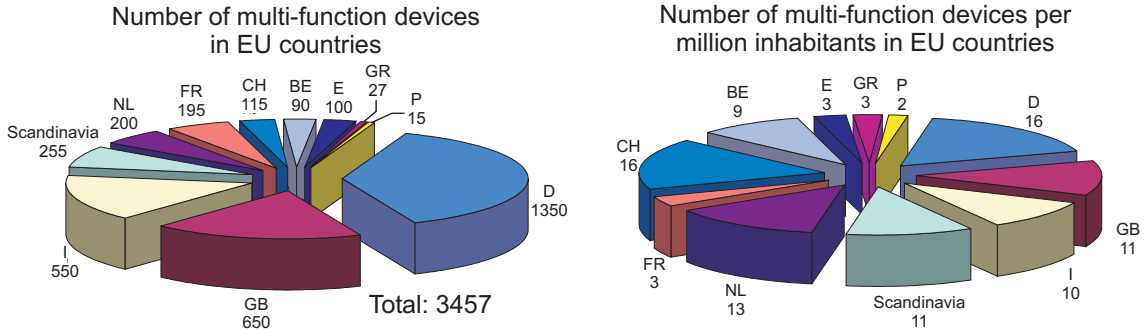

Figure 1.3: Repartition of isokinetic devices on the European market in 2001 adapted from data available in (ANAES, 2001)

1.1.2 Category 2: Devices with limited functionalities

These are microprocessor-controlled devices that can be used for exercise of one or a limited number of body joints. Some of them also offer basic evaluation capabilities and patient visual feedback. These devices offer only a single exercise mode. They are priced between 3500 and 5000 euros. Their compactness and moderate cost makes them affordable for independent practitioners. Some of these devices are even rented to patients for home use (100 euro/week). Major players are KINETEC, OTTOBOCK, ORMED and BIOMETRICS (Figure 1.4).

Figure 1.4: Portable rehabilitation devices

1.1.3 Category 3: Unique function devices

These are portable, low-cost (prices mainly below 100 euros), unactuated devices that can be used either for evaluation or exercise of a specific joint of the body. They do not offer any recording capabilities and no or very basic visual feedback (in evaluation devices, only). Their compactness and very low cost makes them affordable not only to independent practitioners

but also to patients themselves, enabling convenient home exercise. These devices can be of many types, mainly based on the use of springs and resistive elements.

1.2 Motivations and market positioning

From the market analysis described above, we can conclude that there is no portable multi-function muscular evaluation device available on the market that may be affordable to a large number of independent practitioners. Furthermore, some exercise modes are currently only available on the the costly multi-function devices, designed to accommodate all body joints, leading to a lack of accuracy and repeatability in measurements conducted on small joints. Moreover, the bulkiness and complexity of existing devices prohibits their use by the patients without the assistance of a practitioner.

There is thus a need for a device that would offer similar functionalities (and exercise modes) as those implemented on multifunction devices but in a much more compact design, portable, affordable for independent practitioners (price of about 5000 euros), well suited for small joints evaluation and that could be used by the patient in an autonomous way, possibly at home (telemedecine applications).

The aim of this thesis was thus to develop such device. Magneto-rheological (MR) fluid brake actuation was selected thanks to its high level of compactness, high controllability and safety of operation as compared to alternative technologies. The prototype described in this work was designed for the joints of the forearm but could be easily extended to other joints such as hand, ankle... However, it should be noticed that using a controllable brake (semi-active actuator) introduces a limitation as compared to existing multi-function devices which are based on active actuators (CYBEX, BIODEX..). Indeed, a limited number of exercise modes can not be implemented with such type of actuator, since the torque can only be opposed to motion. Figure 1.5 compares the various characteristics of the prototype described in this thesis with the various categories of commercially available devices. It can be observed that it combines the advantages of all categories except for the versatility of exercise modes limited by the use of a brake as actuator.

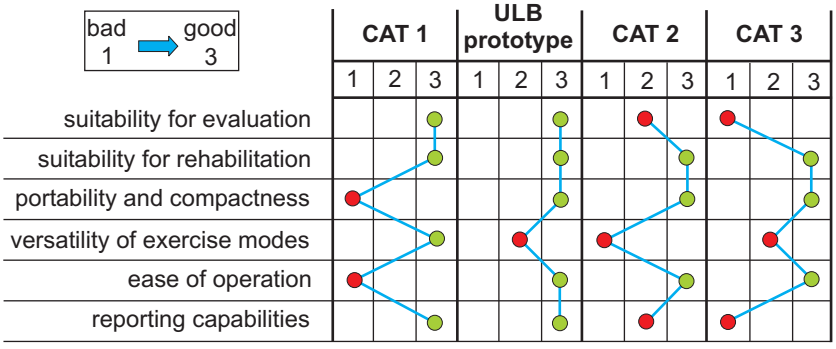

Figure 1.5: Comparison of the characteristics of the prototype with commercially available devices

1.3 Outline

The first part of this thesis is devoted to the design and development of the MR-brake to be used as actuator within the rehabilitation device. It consists of four chapters:

- Chapter 2 introduces the technology of magneto-rheological fluids, their use in mechatronic devices and, in particular, MR brake and clutches. MR-dampers are also briefly discussed, with the corresponding analytical models.
- Chapter 3 recalls the fundamental laws of electromagnetism and describes their application to magnetic circuit design, including MR-fluids gaps.
- Chapter 4 provides a critical review of MR-brake architectures based on their analytical models and gives guidelines for their selection according to various figures of merit.
- Chapter 5 describes the early MR-brake prototypes developed in the frame of this work. Their performances are also analyzed and compared thanks to a custom test bench.

The second part of this work deals with the development of the muscular rehabilitation device itself. It also consists of four chapters:

- Chapter 6 recalls the fundamentals of muscle biomechanics and describes the various methods of muscular testing and exercise.
- Chapter 7 describes the various components of the rehabilitation device developed in this work.
- Chapter 8 is devoted to the control strategies implemented in the device, for its various exercise modes. Simulated and experimental results are compared.
- Chapter 9 analyzes the repeatability of measurements obtained with the prototype and compares them with those obtained with a commercial multi-function device (CYBEX).

1.4 References

ANAES. Les appareils d'isocinétisme en évaluation et rééducation musculaire: Intérêt et utilisation. 2001.

K-M. Chan and N. Maffulli. *Principles and Practice of Isokinetics in Sports Medecine and Rehabilitation*. Williams and Wilkins, Hong-Kong, 1996.

Frost and Sullivan. US rehabilitation equipment markets: Market study, 1998.

E. Leclerq. Etude isocinétique de l'articulation du poignet et dynamométrie manuelle. Master's thesis, Université Libre de Bruxelles, 1999.

Chapter 2

MR-fluids: properties and applications

2.1 Controllable fluids

Controllable fluids exhibit a change in their rheological behavior (mainly their apparent viscosity) upon the application of an external magnetic or electric field. Such fluids are respectively called *magnetorheological* (MR) or *electrorheological* (ER) fluids. These fluids are indeed non-colloidal (i.e. non-homogeneous) suspensions of polarizable micron-sized particles that form chain like structures upon the application of the external field (Figure 2.1). The particle chains are parallel to the field direction and restrict the fluid flow, requiring a minimum field-dependent shear stress (called yield stress) for the flow to be initiated. It is also important to avoid confusion between magnetorheological fluids and colloidal *ferrofluids* composed of nano-sized particles. Ferrofluids are also attracted by a magnetic field but do not exhibit any rheological change (and in particular, no yield stress). They are mainly used within oil seals characterized by very low friction.

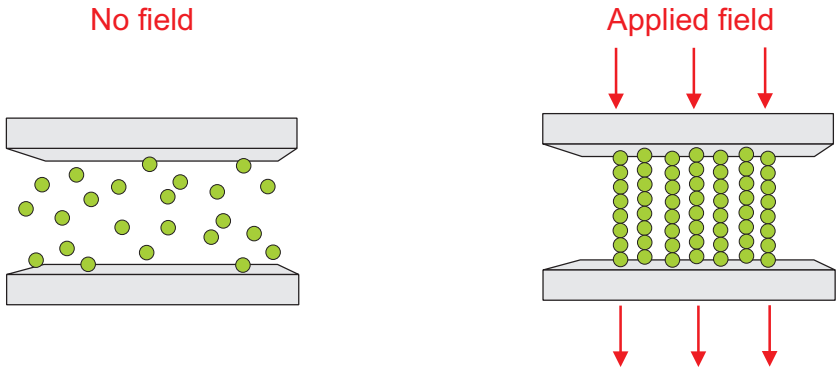

Figure 2.1: Chain-like structure formation in controllable fluids

Since their discovery (Winslow, 1949), considerable research work has been conducted on ER-fluid and devices, much of this work being motivated by potential automotive applications. Despite these major efforts, no commercial device emerged, mainly due to the numerous ER-fluid limitations. Indeed, ER-fluids developed until now exhibit too low yield stress for most applications (2-5kPa, limited by the electric breakdown strength of the fluid). Up to now,

their major field of application is vibration control where devices based on such fluids provide damping forces that are within industrial requirements. They have been used in prototypes of engine mounts, vehicle shock absorbers, shock struts for landing gears... A nice review their applications is available in (Sproston et al., 2002). ER-fluids require high voltage power supplies (several kV) combined with expensive wires and connectors. Furthermore, the temperature dependence of their electrical polarization mechanisms and their high sensitivity to impurities makes their use outside the laboratory costly and difficult (Black and Carlson, 2006).

MR-fluids were also discovered in the late 1940s by J.Rabinow (Rabinow, 1948). However, the initial interest of the scientific community in MR-fluids decreased rapidly at the benefit of ER-fluids, which were thought to be more suited for compact, real-time applications. It is only in the early 1990s that the interest in MR-fluids grew again as they were finally recognized as a good alternative to ER-fluids that suffered from the above mentioned drawbacks. Indeed, only at that time, it was realized that the ten to twenty times greater yield stress of MR-fluids (50-100kPa) would lead to devices with much smaller active fluid volumes (for the same performance), requiring much smaller, faster and less cumbersome electromagnets than initially thought, enabling real-time applications (Black and Carlson, 2006). Moreover, despite similar power requirements than ER-fluid devices (2-50 Watts), MR-fluid devices comprise electromagnets powered by low voltage power supplies. Furthermore, MR-fluids exhibit a broader operating temperature range ($-40°$C to $+150°$C, limited by the properties of the carrier fluid) and are unsensitive to impurities. The researches conducted on MR-fluids since the beginning of the 1990s led to some major developments and commercial successes, especially in the car industry. More details will be given in section 2.6. Table 2.1 summarizes the main characteristics of ER and MR-fluids.

	MR-fluids	**ER-fluids**
Max. yield stress	50-100kPa	2-5kPa
Max. field	∼250kA/m (limited by saturation)	∼4kV/mm (limited by breakdown)
Viscosity	0.1-1.0 Pa.s	0.1-1.0 Pa.s
Operable temperature range	-40 to +150°C (limited by carrier fluid)	-25 to +125°C (limited by polarization mechanisms)
Stability	unaffected by most impurities	cannot tolerate impurities
Response time	<millisecond	<millisecond
Density	3-4g/cm^3	1-2g/cm^3
Power supply (typical)	2-25V at 1-2A (2-50Watts)	2-5kV at 1-10mA (2-50Watts)

Table 2.1: Main characteristics of ER and MR-fluids [adapted from (Carlson, 2007)]

2.2 MR-fluid and MR-dampers models

2.2.1 Bingham model

The behavior of MR-fluids is commonly represented as a Bingham plastic having a variable yield strength (τ_y), depending on the magnetic field (H). For controllable fluids, such a representation was introduced in (Phillips, 1969). In this model, the post-yield flow is governed by the equation:

$$\tau = sgn(\dot{\gamma})\tau_y(H) + \eta\dot{\gamma} \qquad \tau > \tau_y(H) \tag{2.1}$$

where τ is the total shear stress, $\dot{\gamma}$ is the shear rate and η is the viscosity (independent of the magnetic field) (Figure 2.2). In the pre-yield regime ($\tau \leqslant \tau_y$) (at strains of the order 10^{-3}), the MR-fluid is usually considered to behave viscoelastically. Various models have been proposed; a nice review is made in (Gandhi and Bullough, 2005). In the frequency domain, most of them can be summarized with the following expression (Jolly et al., 1998):

$$\tau = G(H)\gamma \qquad \tau \leqslant \tau_y(H) \tag{2.2}$$

where G is the complex, field dependent shear modulus having its real and imaginary parts (G' and G'') increasing with the magnetic field (H). G' and G'' are representative of the components of the force response that are respectively in-phase and 90° out-of-phase with the harmonic displacement excitation.

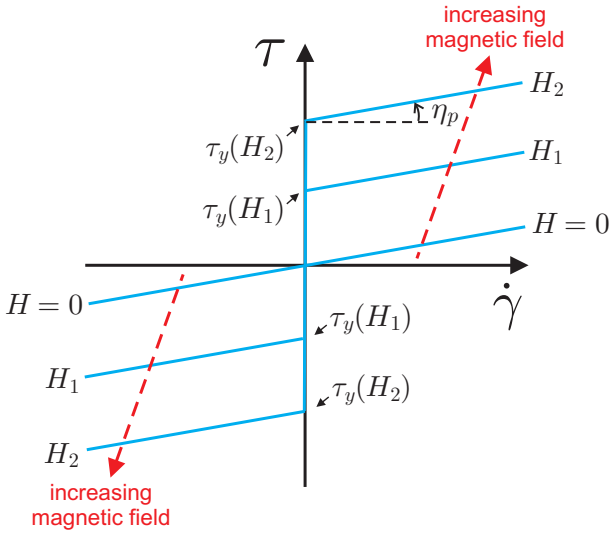

Figure 2.2: Bingham plastic model: shear stress vs shear rate

Based on Bingham's stress-strain behavior of MR-fluids, (Stanway et al., 1987) proposed an idealized mechanical model describing the behavior of a MR-damper. This model consists of a Coulomb friction element placed in parallel with a viscous damper (Figure 2.3a). The force generated by the device is given by:

$$F = f_c sgn\,(\dot{x}) + c_0\dot{x} + f_0 \tag{2.3}$$

where $\dot{x}$ is the piston velocity, c_0 is the damping coefficient and f_c is the frictional force, which is related to the fluid yield stress. An offset force f_0 can be included to account for the presence of an accumulator. It should be noticed that this model does not take into account the hysteresis of the force-velocity relationship.

2.2.2 Gamota and Filisko model

(Gamota and Filisko, 1991) proposed an extension of the Bingham model. The model consists of the Bingham model in series with a standard model of a linear solid material (Figure 2.3b). The dynamic equations for this model are:

$$\left.\begin{array}{rcl} F &=& k_1(x_2-x_1)+c_1(\dot{x}_2-\dot{x}_1)+f_0 \\ &=& c_0\dot{x}_1+f_c sgn\left(\dot{x}_1\right)+f_0 \\ &=& k_2(x_3-x_2)+f_0 \end{array}\right\}, |F|>f_c \tag{2.4}$$

$$\left.\begin{array}{rcl} F &=& k_1(x_2-x_1)+c_1\dot{x}_2+f_0 \\ &=& k_2(x_3-x_2)+f_0 \end{array}\right\}, |F|\leqslant f_c \tag{2.5}$$

where c_0 is the damping coefficient associated with the Bingham model and k_1, k_2 and c_1 are associated with the solid material. Compared to the Bingham model, this model introduces hysteresis and may better reconstruct the behavior of the damper. However, Eq.(2.4) and (2.5) are difficult to solve numerically, requiring a very small step time in numerical integration.

2.2.3 Bouc-Wen model

Another model that has been used extensively for modelling hysteretic systems, and is numerically tractable, is the Bouc-Wen model (Wen, 1976)(Figure 2.3c). However, this model still exhibits disparities with the experimental curves in regions where the acceleration and the velocity have opposite signs. The force in this system is given by:

$$F = c_0\dot{x}+k_0\left(x-x_0\right)+\alpha z \tag{2.6}$$

where the evolutionary variable z is governed by:

$$\dot{z} = -\gamma\left|\dot{x}\right| z\left|z\right|^{n-1}-\beta\dot{x}\left|z\right|^n+A\dot{x} \tag{2.7}$$

The parameters β, γ and A in the Bouc-Wen model are used to control the linearity in the unloading region and the smoothness of the transition from the pre-yield to the post-yield region. The accumulator stiffness is represented by k_0 and x_0 is associated to initial pressure in the accumulator, giving the static force $f_0 = k_0x_0$.

2.2.4 Spencer et al. model

(Spencer et al., 1997) proposed a slightly modified version of the Bouc-Wen model (Figure 2.3d) to introduce roll-off in the regions where the force and the velocity have opposite signs in order to better predict the damper behavior. The MR damper force becomes:

$$F = c_1\dot{y} + k_1(x - x_0) \tag{2.8}$$

where

$$\dot{z} = -\gamma\,|\dot{x} - \dot{y}|\,z\,|z|^{n-1} - \beta\,(\dot{x} - \dot{y})\,|z|^n + A\,(\dot{x} - \dot{y}) \tag{2.9}$$

$$\dot{y} = \frac{1}{c_0 + c_1}\left[\alpha z + c_0\dot{x} + k_0\,(x - y)\right] \tag{2.10}$$

The accumulator stiffness is represented by k_1 and the viscous damping observed at larger velocities is represented by c_0. The dashpot c_1 is included in the model to produce the roll-off at low velocities and k_0 to control the stiffness at large velocities.

2.3 MR-fluids composition

MR-fluid formulation consists of three main components: magnetizable particles (with a volume fraction typically between 20% and 45%), a carrier fluid and an association of various additives. The proper selection and combination of these components is of prime importance since it will define all the macroscopic characteristics of the fluid such as its off-state viscosity, its maximum yield stress, its resistance to settling, its operating temperature range... This fact explains the abundance of literature on this topic and the wide variety of reported MR-fluid formulations. In this section, we will summarize the main trends observed for MR-fluid composition.

2.3.1 Magnetizable particles

Maximum inter-particle attraction (and thus maximum yield-stress) increases with the square of the saturation magnetization J_s of the particles (Carlson and Jolly, 2000) (Ginder et al., 1996). The most widely used material for MR-fluid particles is carbonyl iron, thanks to its high saturation magnetization (Carlson, 2009). Carbonyl iron powder is obtained by the thermal decomposition of iron pentacarbonyl ($Fe(CO)_5$), leading to highly spherical particles in the 1-10μm range. The spherical shape is of particular interest since it makes the particles less abrasive, more robust and durable. These particles are further characterized by an onion skin structure and an iron content up to 97.8% (Figure 2.4). Iron powders obtained from less expensive processing techniques (such as water atomization) have also been considered and used in MR-fluid formulations. However, it should be noticed that these particles exhibit much larger sizes (10-100μm) and are more irregular in shape, affecting their abrasiveness and durability. Furthermore, highly irregular particles lead to higher fluid viscosity compared to spherical particles at the same volume fraction (Black and Carlson, 2006).

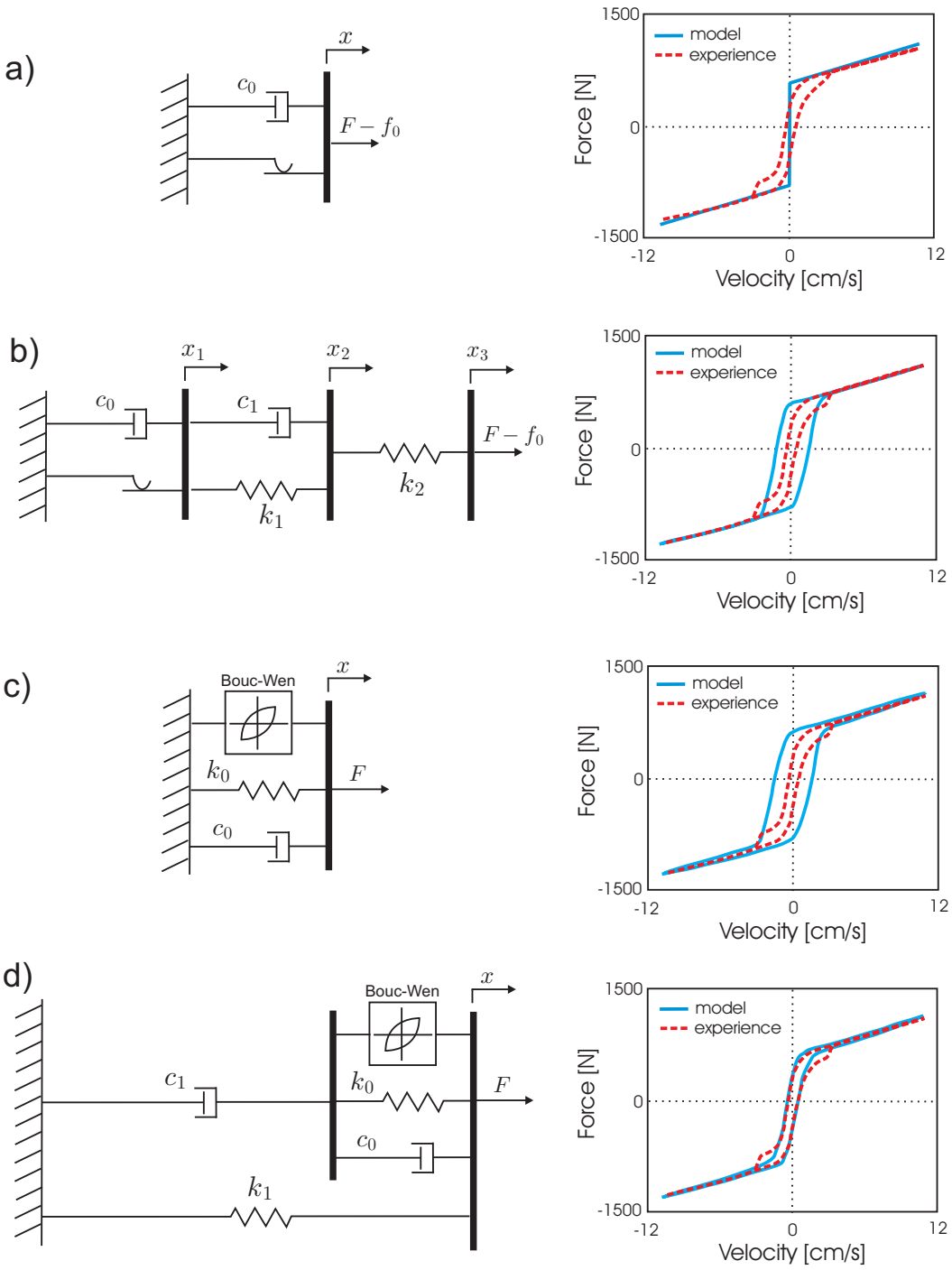

Figure 2.3: MR-fluid and MR-dampers models: a) Bingham model - b) Gamota and Filisko model - c) Bouc-Wen model - d) Spencer et al. model - Force/velocity curves are adapted from (Spencer et al., 1997)

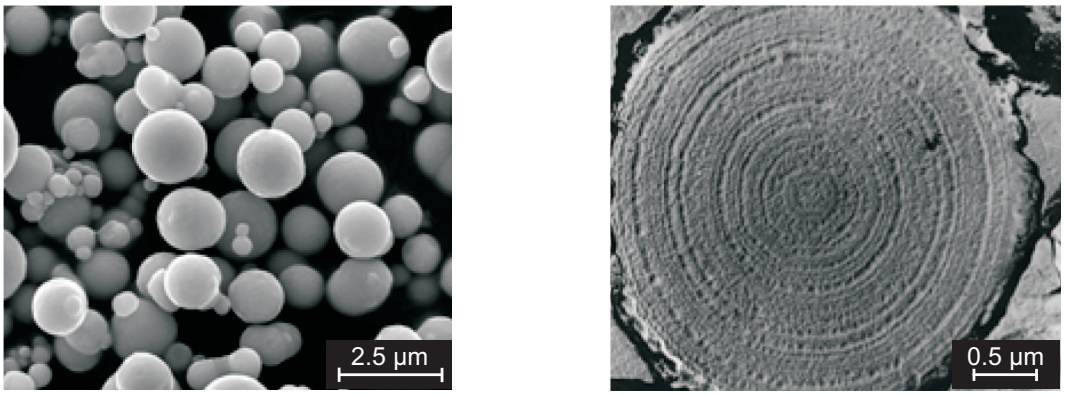

Figure 2.4: Scanning electron microscope images of carbonyl iron powder: a) spherical particles - b) onion skin structure [adapted from (BASF, 2006)]

2.3.2 Carrier fluid

Carrier fluids are selected based on their intrinsic viscosity, their temperature stability and their compatibility with other materials of the device. The most common carrier fluids are hydrocarbon oils, which can either be mineral oils or synthetic oils (or a combination of both), thanks to their good lubrication, durability and the availability of a large range of additives. Silicon oils can be used instead in order to achieve a broader operating temperature range or due to compatibility issues with other materials of the device (e.g. rubber seals). (Jolly et al., 1998) gives guidelines regarding the temperature range of some MR-fluid formulations as well as their compatibility with typical seals materials.

2.3.3 Additives

Many types of additives, often proprietary, are used in MR-fluid formulations. They have many purposes such as: inhibit particle settling and agglomeration, reduce friction, prevent particle oxidation and wear. The major impact of these properties on the MR-fluid stability and durability, which are crucial in industrial applications, explains the fact that, in recent years, much of the MR-fluid research effort was focused on the development of new additive packages.

Particle settling may appear in MR-fluids due to the large difference between particles and carrier fluid densities. This phenomenon may be accompanied by particle agglomeration, which means that particles are sticking together in the absence of magnetic field (due, for example, to a small level of remnant magnetization in the particles). While a small level of particle settling is not really an issue in devices where the fluid is naturally and efficiently remixed during operation (such as dampers and shock absorbers in automotive applications (Carlson, 2003)), in other applications such as seismic dampers, agglomeration has to be avoided since, in that case, particle redispersion is much more difficult to achieve, leading to an alteration of the MR-fluid properties.

2.4 Properties of MR-fluids

2.4.1 Off-state viscosity

The field-independent viscosity (η) is the most critical off-state property of MR-fluids since it has a direct impact on the velocity-dependent minimum output force or torque of a given device in the absence of magnetic field. Furthermore, this viscosity is also responsible for the temperature dependance of the device output force or torque.

The MR-fluid viscosity is mostly influenced by two factors: the intrinsic viscosity of the carrier fluid and the particle volume fraction. The higher the particle volume fraction, the higher the MR-fluid viscosity. At room temperature, most MR-fluid viscosities range from 50 to 200mPas (Carlson, 2009).

2.4.2 Yield stress

The field-dependent maximum yield stress (τ_y) is the most critical on-state property of MR-fluids since it has a direct impact on the maximum output force or torque of a given device.

As already discussed in section 2.3.1, the material of the particles has an impact on the maximum yield stress since its value increases with the square of the saturation magnetization of the particles (Carlson and Jolly, 2000).

A second factor influencing the maximum yield stress is the particle volume fraction. Rabinow, in 1948, already demonstrated that increasing the particle volume fraction led to an increase of the output torque of his MR-fluid clutch. Since then, a number of researchers have studied this effect (Genç, 2002) (Kordonski et al., 1997) and have shown that the maximum yield stress increases non-linearly with growing particle volume fraction (Chin et al., 2001) (Foister, 1997)(Figure 2.5a). Unfortunately, as already mentioned in section 2.4.1, the off-state plastic viscosity also increases with particle volume fraction, at an even faster rate than the yield stress (Figure 2.5b), leading to a decrease of the potential dynamic range (ratio between maximum and off-state force or torque) of a device using such fluids.

An alternative way to increase the maximum yield stress is to increase the particle size distribution inside the MR-fluid. The advantage of this technique is that it allows the viscosity to be reduced while maintaining the same particle volume fraction (Goncalves et al., 2006). A particular case of this technique is to use bimodal particle distributions, where two different size groups of particles are combined (Golden et al., 2005) (Weiss et al., 1999) (Foister, 1997). As shown in Figure 2.6, a substantial increase in yield stress can be achieved by a small increase in the proportion of small particles (25% in weight). This effect can be explained by an increased particle packing when chains are formed.

Figure 2.7 shows graphs of the yield stress (τ_y) versus magnetic field (H) for some typical MR-fluids from LORD corporation and ISC Fraunhofer Institut Silicatforschung (data obtained from product datasheets).

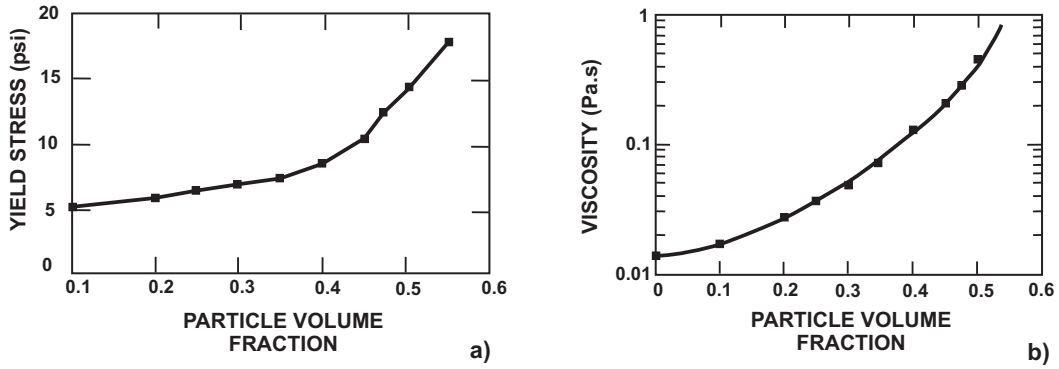

Figure 2.5: a) Maximum yield stress versus particle volume fraction (under magnetic flux density of 1Tesla) - b) Viscosity versus particle volume fraction [adapted from (Foister, 1997)]

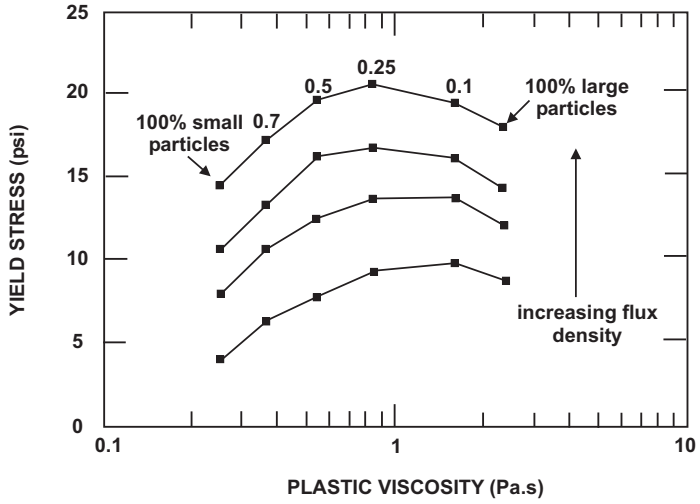

Figure 2.6: Maximum yield stress versus plastic viscosity for various bimodal formulations (unchanged total particle weight fraction of 55%) [adapted from (Foister, 1997)]

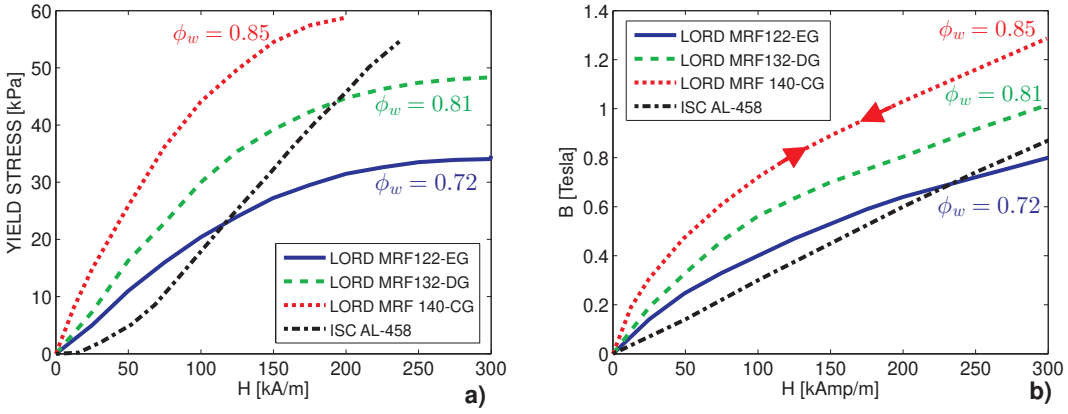

Figure 2.7: a) Maximum yield stress versus magnetic field - b) B-H characteristic, for various fluid formulations (ϕ_w is the particle weight fraction)

Very different behaviors can be observed due to different fluid formulations (in particular various particle weight fractions, ϕ_w). Furthermore, differences between the shape of the curves for LORD and ISC fluids may also be explained by different experimental protocols used to measure the yield stress. For the fluids provided by LORD corporation, it can be seen that the yield stress begins to saturate for magnetic fields above 250kA/m. Unfortunately, from the data available to us, no conclusion could be drawn about the magnetic field intensity at which the AL-458 yield stress saturates.

2.4.3 B-H relationship

From the data available in product datasheets, the B-H curve for MR-fluids within their useful range is mainly non-linear for the fluids provided by LORD, but linear for the ISC fluid. Such difference may be explained by different MR-fluid formulations or differences in the experimental protocol. Figure 2.7b) shows a graph of the induction field (B) versus magnetic field (H) for the MR-fluids considered in this study.

Furthermore, it is important to note that little or no hysteresis can be observed in the MR-fluid B-H curves. This behavior is a consequence of the magnetically soft properties of the iron used for the particles as well as the mobility of these particles (Jolly et al., 1998).

2.4.4 Durability and In-Use-Thickening

First durability tests conducted on MR-fluid devices at the end of the 1990s have shown that, if an ordinary MR-fluid is subjected to high stress and high shear rate over a long period of time, the fluid will thicken (Carlson, 2001). This phenomenon is called In-Use-Thickening (IUT). A MR-fluid initially exhibiting low off-state viscosity will progressively thicken until it eventually turns into a thick paste exhibiting a much higher off-state viscosity and making it unusable in most applications.

One of the causes of IUT is the fact that, when exposed to long periods of stress, the friable surface layer of the iron particles peals away and breaks into small pieces that separate from the primary particle. This is particularly true for carbonyl iron particles exhibiting an onion skin structure (Figure 2.4). Solutions to this phenomenon include the use of particles exhibiting a higher hardness and/or the use of anti-wear and anti-friction additives (at levels of 0.5 to 3% by volume) (Goncalves et al., 2006).

2.5 Operating modes of MR-fluids

MR-fluids are operated in four different modes (Figure 2.8): valve mode, direct shear mode, squeeze mode and pinch mode. Valve and direct shear modes have been used in a wide variety of devices, while squeeze mode is much less well known and pinch mode has only been recently proposed (Goncalves and Carlson, 2008).

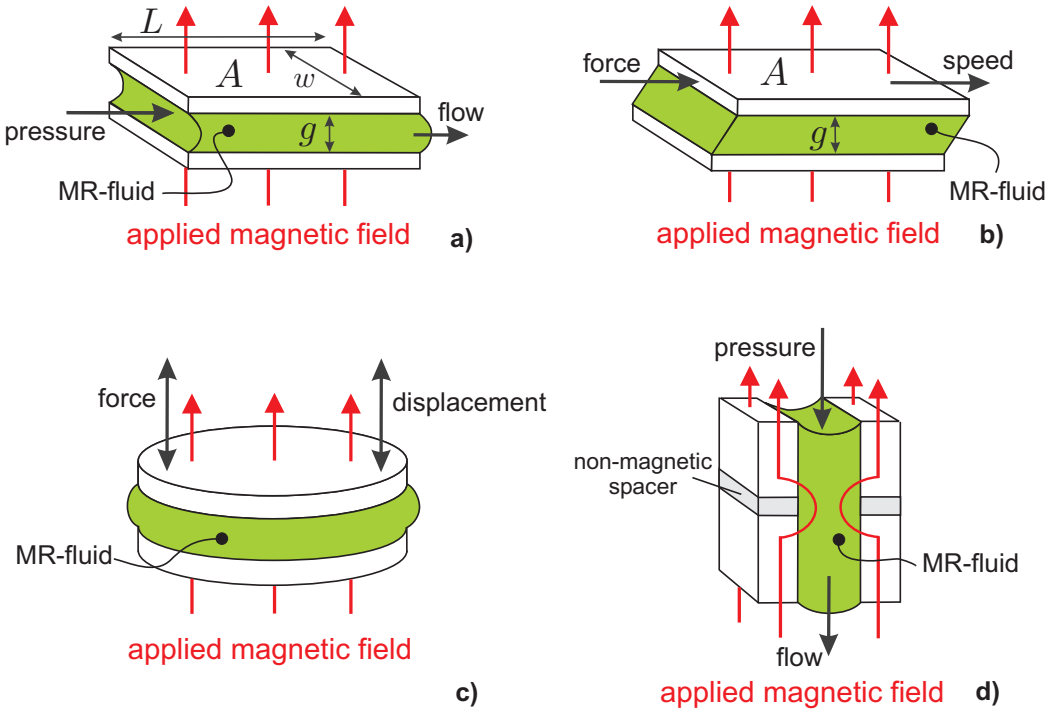

Figure 2.8: Operating modes of MR-fluids: a) valve mode - b) direct shear mode - c) squeeze mode - d) pinch mode

In the **valve mode** (Figure 2.8a), the MR-fluid flows through a channel while an external magnetic field is applied perpendicular to the flow direction. The resistance to the fluid flow can be adjusted by varying the intensity of the applied magnetic field, creating in that way a controllable valve mechanism that does not require any movable mechanical part (Black and Carlson, 2006). Devices based on the valve mode essentially include dampers and shock absorbers used in a broad range of applications.

In the **direct shear mode** (Figure 2.8b), the MR-fluid is contained between two parallel surfaces (poles) while an external magnetic field is applied perpendicular to the poles. A force is applied to one of the poles, making it move laterally relative to the other, directly shearing the fluid layer. The force required to cause the fluid to shear depends on the intensity of the applied magnetic field and on the resulting shear stress developed in the MR-fluid. Devices based on the shear mode essentially include brakes and clutches used in a broad range of applications. This mode is used in the device described in this thesis.

In the **squeeze mode** (Figure 2.8c) (Gstöttenbauer, 2008), the MR-fluid is contained between two parallel surfaces (poles) while an external magnetic field is applied perpendicular to the poles. A force is applied perpendicular to one of the poles, making it move towards the other, compressing the fluid layer. For a given force, the displacement of the moving pole is controlled by the intensity of the applied magnetic field. Displacement amplitudes are very small (in the order of some millimeters) but resistive forces are very high. Despite a much smaller amount of applications, this operating mode has however been explored in

small amplitude vibration and impact dampers (Carlson, 1996) (Jolly and Carlson, 1996).

In the **pinch mode** (Figure 2.8d), as for the valve mode, the MR-fluid flows through a channel. But, here, the external magnetic field is applied more or less parallel to the flow direction by arranging the poles axially along the flow path and separating them by a non-magnetic spacer. On the contrary to all previous operating modes, such configuration leads to a highly non-uniform magnetic field inside the MR-fluid. The main idea is rather than solidifying the fluid throughout the valve (as in the valve mode), the MR-fluid is solidified by the the magnetic field only near the walls, changing in that way the effective orifice diameter through which the fluid flows (Goncalves and Carlson, 2008).

2.6 Applications in mechatronic devices

2.6.1 Dampers and shock absorbers

MR-fluid dampers and shock absorbers developments have mainly been driven by the requirements of the automotive industry and have largely benefited from previous R&D work conducted on ER-fluid devices in the 1980s.

Early commercial products appeared in 1998 with MR-fluid dampers to be used in semi-active seat suspensions for trucks and with adjustable MR-fluid based primary suspension for racing cars (Carlson and Sproston, 2000). However, the first real commercial breakthrough was made in 2002 with the introduction, by Delphi, of the MagneRide, the first commercial suspension system having real-time controllable MR-fluid shock absorbers that automatically adapt to changing road conditions with a faster response time, fewer moving parts and lower power requirements than previous hydraulic systems (Sproston et al., 2002)(Figure 2.9). This system, initially available on top-of-the-range (Cadillac STS, Buick Lucerne) and sports cars (Chevrolet Corvette, Ferrari 599, Audi TT) is progressively being implemented on mid-range vehicles (available on Audi A3 from 2008).

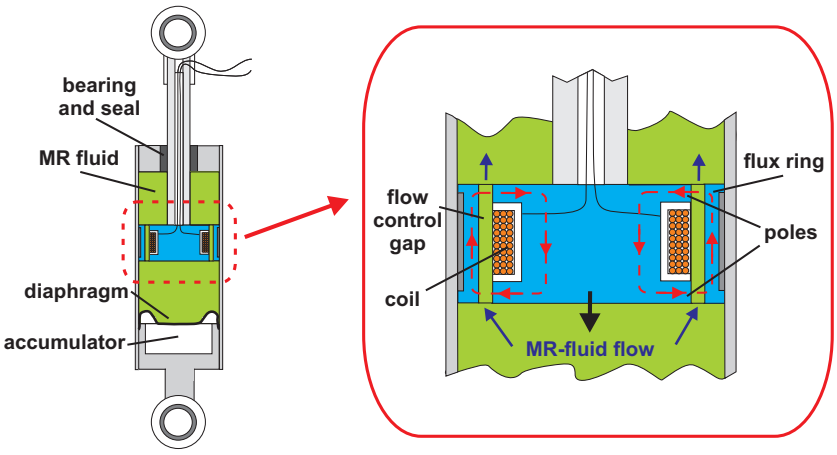

Figure 2.9: Schematic cross-section view of a magneto-rheological shock absorber [adapted from (Carlson, 2007)]

Another application under development for the automotive industry is the MR-fluid engine vibration isolation. Using MR-fluids inside such engine mounts allows to modify their stiffness in real-time and achieve the best possible isolation for each RPM of the engine (Figure 2.10) (Carlson, 2007) (Barber and Carlson, 2008).

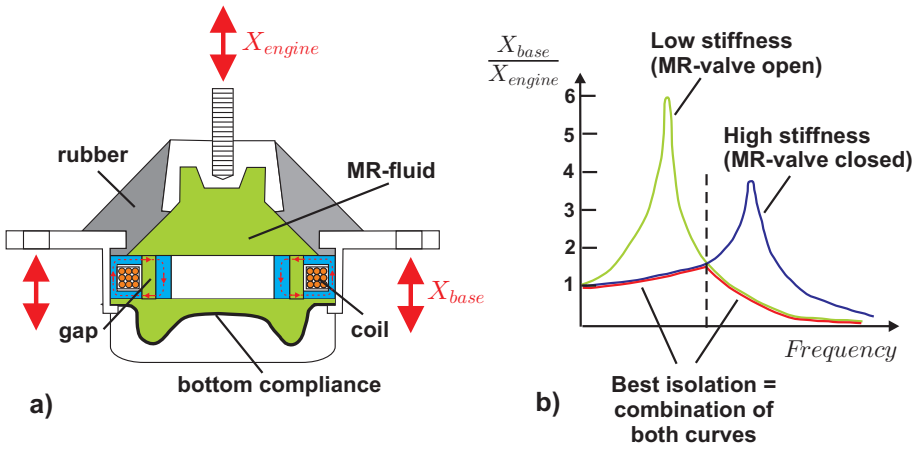

Figure 2.10: a) MR-fluid engine mount - b) vibration isolation performances [adapted from (Carlson, 2007)]

The automotive industry is not the only one to benefit from developments in the field of MR-fluid devices. Large MR-fluid dampers (capacity up to 300kN)(Figure 2.11a) have also been developed to be implemented for semi-active vibration control in civil engineering structures. They have been used in bridges and buildings to limit the effects of seismic and wind excitation (Sproston et al., 2002) (Carlson, 2007) (Yang et al., 2002). It is important to note that, for seismic applications, sedimentation is a real issue since the damper may not be used for a very long period of time.

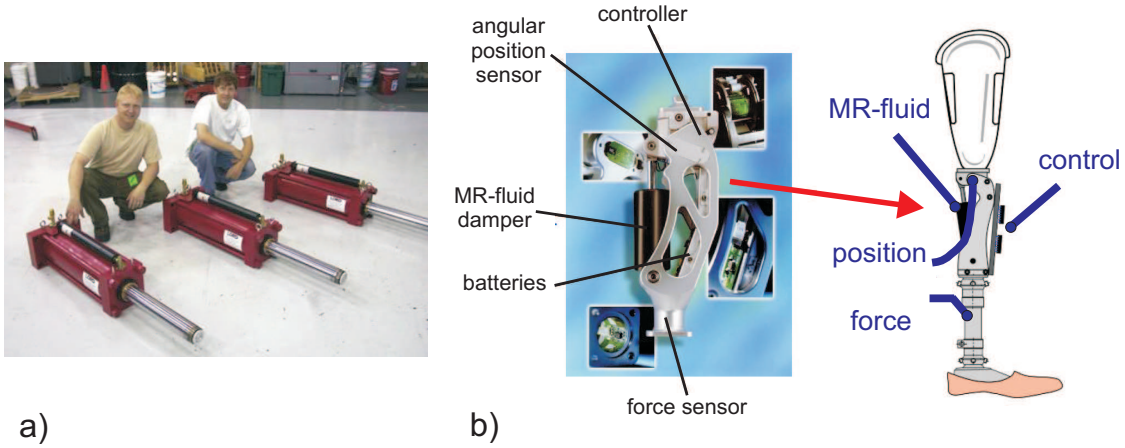

Figure 2.11: a) MR-fluid high capacity dampers for vibration control in civil engineering structures [adapted from (Carlson, 2007)] - b) Biedermann-Motech above-knee prosthesis based on MR-fluid damper [adapted from (Carlson and Sproston, 2000)]

MR-fluid technology, thanks to its inherent compactness has also been implemented in portable rehabilitation applications. In 2000, Biedermann Motech introduced an above-knee prosthesis based on a real-time controlled MR-fluid damper, increasing gait balance, stability (even when walking on stairs or ramps) and energy efficiency (Biedermann, 2002) (Biedermann et al., 2004)(Figure 2.11b).

2.6.2 Brakes and clutches

Despite the fact that, today, the major part of commercial MR-fluid devices are MR-dampers used in the automotive industry, the first commercial application of a MR-fluid device was, in 1995, into the exercise market as variable resistance brake for use in aerobic stair-climbers and cycling machines developed by Nautilus (Webb, 1998) (Carlson and Sproston, 2000)(Figure 2.12a). Indeed, such MR-brake was quieter, less expensive and more compact than previous eddy-current brakes. Furthermore, MR-brakes are running at much lower voltages reducing the cost of the power supply (Baker, 1995). Unfortunately, due to the intense use to which some exercise equipment can be subjected, problems of fluid deterioration (IUT, see section 2.4.4) caused reliability issues. More recent fluid formulation may solve this problem.

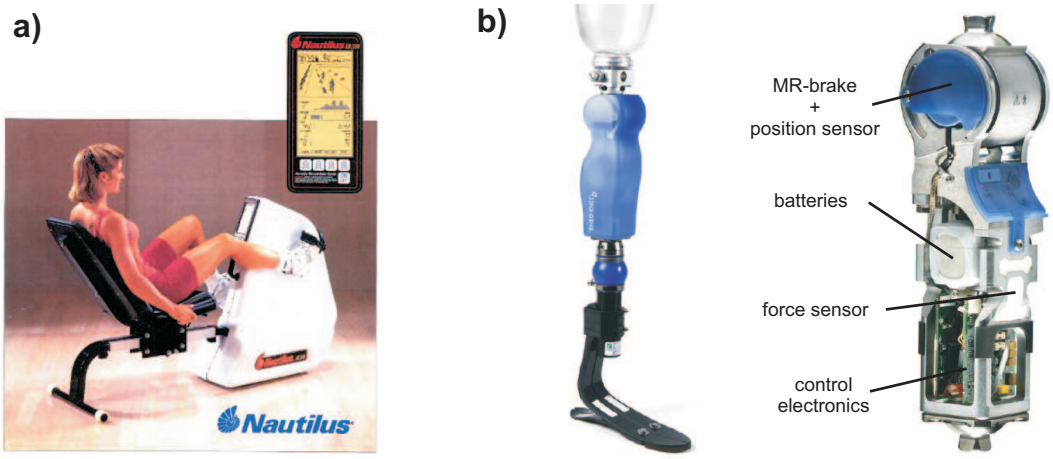

Figure 2.12: a) Nautilus aerobic cycling machine - b)Rheoknee / knee prosthesis based on a rotary MR-brake commercialized by OSSUR [adapted from (OSSUR)]

Real-time controlled "smart" prosthesis can also integrate rotary MR-brakes instead of linear MR-dampers. This is the case of the knee prosthesis developed by the MIT (Deffenbaugh et al., 2001) and commercialized by OSSUR (Figure 2.12b). It seems indeed more logical to make use of a rotational device to implement the knee joint.

As can be seen on Figure 2.12b), thanks to the high level of compactness of the MR-brake used (40Nm - diameter: 6cm), all electronics, sensors and batteries can fit within the lower part of the prosthesis. Other applications in the same field and based on the same technology include "smart" orthoses for various human joints as described in the patent by (Carlson, 1997). Some developments in this area have already been conducted by (Furusho et al., 2007)

leading to a first prototype of ankle-orthosis.

Force-feedback (haptic) interfaces also benefit from the high compactness and high torques of MR-brakes and clutches. Furthermore, in such applications, brakes offer a major advantage over motors since they can only apply resistive forces, ensuring user safety. This property is also a drawback since they can not simulate all types of force (like a spring in its extension phase, for instance). An example of industrial application is the use of a rotary brake implemented as actuator within a steer-by-wire system for electric forklift trucks, eliminating the mechanical connection between the steering wheel and the ground wheels (Carlson and Sproston, 2000). Two degree-of-freedom pantograph type haptic displays have also been developed by (Reed, 2003) and (Yamaguchi et al., 2003), respectively using MR brakes and MR-clutches. The compactness and absence of backlash of MR-brakes have also been exploited in the development of haptic knobs to be used as multipurpose user interface in automotive vehicles (Ackermann and Elferich, 2000).

Other automotive applications include the use of MR-clutches. Since 2003, General Motors studies the feasibility of using them as radiator fan drive clutches, instead of conventional silicon oil clutches, in trucks and SUVs, with the objective of reducing the fuel consumption by 2.5% thanks to a lower off-state viscosity and smoother torque transitions (Carlson and Johnson, 2004) (Smith et al., 2007). MAGNA Powertrain, in cooperation with BASF, also developed and tested a 700Nm MR-fluid rotational clutch used as a coupling unit between front and rear axle on a 4-wheel drive vehicle (Kieburg, 2008). The results showed superior driving performance compared to what can be achieved with the current technology.

Finally, in 2002, preliminary tests in weightlessness have also been conducted by the NASA to validate the the feasibility of using MR-brakes as part of deployment mechanisms for space structures (antennas...) (Sproston et al., 2002).

As can be seen from these few examples, MR-fluid devices, thanks to their numerous advantages (compactness, high forces or torques, low power consumption, smoothness and safety of operation), can be used in a wide variety of fields ranging from automotive to rehabilitation. Many of these characteristics will also be exploited in the rehabilitation device described in this thesis.

2.7 References

B. Ackermann and R. Elferich. Application of magnetorheological fluids in programmable haptic knobs. In *Proceedings of Actuator 2000*, Bremen, Gremany, 2000.

A. Baker. Brake cuts exercise-equipment cost. *Design news*, 1995.

D.E. Barber and J.D. Carlson. Performance characteristics of prototype MR engine mounts containing LORD glycol MR fluids. In *Proceedings of ERMR'08*, Dresden, Germany, 2008.

BASF. Product datasheet: Carbonyl iron powders. 2006.

L. Biedermann. Leg prosthesis with an artificial knee joint provided with adjustment device. US patent 6,423,098, 2002.

L. Biedermann, W. Matthis, and C. Schulz. Leg prosthesis with an artificial knee joint and method for controlling a leg prosthesis. US patent 6,755,870, 2004.

T. Black and J.D. Carlson. *Synthetic, Mineral Oils and Bio-Based Lubricants*, chapter 35: Magnetizable Fluids, pages 565–583. Taylor and Francis, 2006.

J.D. Carlson. What makes a good MR-fluid? In *Proceedings of the 8th ERMR Conference*, pages 63–69, Nice, France, 2001.

J.D. Carlson. What makes a good MR fluid. *Journal of Intelligent Material Systems and Structures*, 13:431–435, 2003.

J.D. Carlson. Semi-active vibration supression. In *CISM Course: Semi-Active Vibration Suppression - the Best from Active and Passive Technologies*, Udine, October 2007.

J.D. Carlson. *Smart Materials*, chapter 17: Magnetorheological Fluids, pages 17.1–17.8. CRC Press, 2009.

J.D. Carlson. Multi-degree of freedom magnetorheological devices and system for using same. US patent 5,492,312, 1996.

J.D. Carlson. Portable magnetically controllable fluid rehabilitation devices. World patent WO 97/33658, 1997.

J.D. Carlson and A.R. Johnson. Electro-rheological and magnetorheological fluids: A state-of-the-art report. In *Proceedings of Actuator'04*, Bremen, Germany, 2004.

J.D. Carlson and M.R. Jolly. MR fluid, foam and elastomer devices. *Mechatronics*, 10: 555–569, 2000.

J.D. Carlson and J.L. Sproston. Controllable fluids in 2000 - status of ER and MR fluid technology. In *Proceedings of Actuator'00*, Bremen, Germany, 2000.

B.D. Chin, J.H. Park, M.H. Kwon, and O.O. Park. Rheological properties and dispersion stability of magnetorheological (MR) suspensions. *Rheologica Acta*, 40:211–219, 2001.

B.W. Deffenbaugh, H.M. Herr G.A. Pratt, and M.B. Wittig. Electronically controlled prosthetic knee. US patent application 2001/0029400, 2001.

R.T. Foister. Magnetorheological fluids. US patent 5,667,715, 1997.

J. Furusho, T. Kikuchi, M. Tokuda, T. Kakehashi, K. Ikeda, S. Morimoto, Y. Hashimoto, H. Tomiyama, A. Nakagawa, and Y. Akazawa. Development of a shear type compact MR brake for the intelligent ankle-foot orthosis and its control. In *Proceedings of the 2007 IEE 10th International Conference on Rehabilitation and Robotics*, pages 89–94, Noordwijk, The Netherlands, 2007.

D.R. Gamota and F.E. Filisko. Dynamic mechanical studies of electrorheological materials: Moderate frequencies. *Journal of Rheology*, 35:399–425, 1991.

F. Gandhi and W.A. Bullough. On the phenomenological modeling of electrorheological and magnetorheological fluid preyield behavior. *Journal of Intelligent Material Systems and Structures*, 16:237–248, 2005.

S. Genç. *Synthesis and Properties of Magnetorheological (MR) Fluids*. PhD thesis, University of Pittsburg, 2002.

J.M. Ginder, L.C. Davis, and L.D. Elie. Rheology of magnetorheological fluids: Models and measurements. *International Journal of Modern Physics B*, 10:3293–3303, 1996.

M.A. Golden, J.C. Ulicny, K.S. Snavely, and A.L. Smith. Magnetorheological fluids. US patent 6,932,917, 2005.

F.D. Goncalves and J.D. Carlson. An alternate operation mode for MR-fluids - magnetic gradient pinch. In *Proceedings of the 11th ERMR Conference*, Dresden, Germany, 2008.

F.D. Goncalves, J-H. Koo, and M. Ahmadian. A review of the state of the art in magnetorheological fluid technologies - part i: MR fluid and MR fluid models. *The Shock and Vibration digest*, 38:203–219, 2006.

N. Gstöttenbauer. *Magneto-Rheological Fluids in Squeeze Mode*. PhD thesis, Johannes Kepler University of Linz, 2008.

M.R. Jolly and J.D. Carlson. A controllable squeeze film damper using magnetorheological fluid. In *Proceedings of Actuator 96*, pages 333–336, Bremen, Germany, 1996.

M.R. Jolly, J.W. Bender, and J.D. Carlson. Properties and applications of commercial magnetorheological fluids. In *Proceedings of SPIE 5th International Symposium on Smart Structures and Materials*, San Diego, California, 1998.

C. Kieburg. MR all-wheel-drive prototype car driving tests and durability requierements for the MR fluids used. In *Proceedings of ERMR'08*, Dresden, Germany, 2008.

W.I. Kordonski, S.R. Gorodkin, and Z.A. Novikova. The influence of ferroparticle concentration and size on MR-fluid properties. In *Proceedings of the 6th ERMR Conference*, pages 532–542, Yonezawa, Japan, 1997.

OSSUR. Rheoknee product datasheet.

R.W. Phillips. *Engineering Applications of Fluids with a Variable Yield Stress*. PhD thesis, University of California, Berkeley, 1969.

J. Rabinow. The magnetic fluid clutch. *American Institute of Electrical Engineers Transactions*, 67:1308–1315, 1948.

M. R. Reed. Development of an improved dissipative passive haptic display. Master's thesis, Georgia Institute of Technology, 2003.

A.L. Smith, J.C. Ulicny, and L.C. Kennedy. Magnetorheological fluid fan drive for trucks. *Journal of Intelligent Material Systems and Structures*, 18:1131–1136, 2007.

B.F. Spencer, S.J. Dyke, M.K. Sain, and J.D. Carlson. Phenomenological model of a magnetorheological damper. *ASCE Journal of Engineering Mechanics*, 123(3):230–238, 1997.

J.L. Sproston, L.C. Yanyo, J.D. Carlson, and A.K. El Wahed. Controllable fluids in 2002 - status of ER and MR fluid technology. In *Proceedings of Actuator '02*, pages 333–338, Bremen, Germany, 2002.

R. Stanway, J.L. Sproston, and N.G. Stevens. Non-linear modelling of an electro-rheological vibration damper. *Journal of Electrostatics*, 20:167–184, 1987.

G.M. Webb. Exercise apparatus and associated method including rheological fluid brake. US patent 5,810,696, 1998.

K.D. Weiss, J.D. Carlson, and D.A. Nixon. Method and magnetorheological fluid formulations for increasing the output of a magnetorheological fluid device. US patent 5,900,184, 1999.

Y.K. Wen. Method of random vibration of hysteretic systems. *Journal of Engineering Mechanics Division 102*, pages 249–263, 1976.

W.M. Winslow. Induced fibration of suspensions. *Journal of Applied Physics*, 20:1137–1140, 1949.

Y. Yamaguchi, J. Furusho, K. Koyanagi, and S. Kimura. Development of a 2-d force display system using MR actuators. In *Proceedings of ICAT 2003*, Tokyo, Japan, 2003.

G. Yang, B.F. Spencer, J.D. Carlson, and M.K. Sain. Large-scale MR fluid dampers: Modeling and dynamic performance considerations. *Engineering Structures*, 24(3):309–323, 2002.

Chapter 3

Magnetic circuit design

3.1 Fundamentals of electromagnetism

3.1.1 Ampere's law

Ampere's law describes the relation between the electric current in a conductor (I, expressed in Amperes [A]) and the resulting magnetic field (H, expressed in Amperes/meter [A/m]). It states that the line integral of the tangential component of the magnetic field strength around a closed path is equal to the total current enclosed by the path whatever the number of electrical conductors (Edminister, 1993)(Figure 3.1). Furthermore, it is important to note that H is independent of the properties of the medium (e.g. air, steel, MR-fluid...).

For a single conductor, we have:

$$\oint_C \vec{H} \cdot \vec{dl} = I \tag{3.1}$$

For N conductors, we have:

$$\oint_C \vec{H} \cdot \vec{dl} = NI \tag{3.2}$$

where NI is called the magnetomotive force ($\mathscr{F}$), expressed in Ampere-turns.

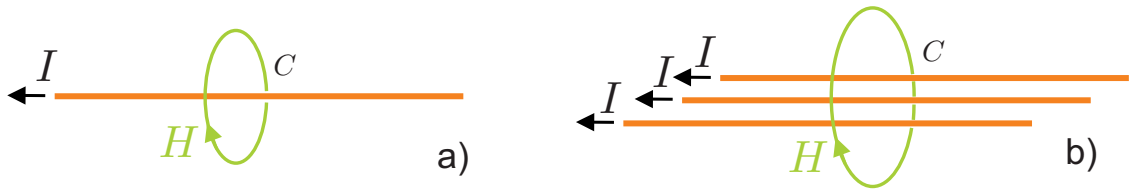

Figure 3.1: Magnetic field generated by: a) a single conductor - b) N conductors

3.1.2 B-H relationship

B is the magnetic flux density (also called magnetic induction), usually expressed in Tesla [T]. On the contrary to H, B depends on the properties of the medium. The relation between

B and H is given by:

$$B = \mu H = \mu_0 \mu_r H \tag{3.3}$$

where μ_0 is the absolute permeability of the vacuum (constant = $4\pi.10^{-7}$ Henry/m) and where μ_r is the relative permeability of the medium (not constant, function of H)

For non-ferromagnetic materials, $\mu_r \approx 1$. For ferromagnetic materials, $\mu_r >> 1$ (typical values are: iron=5000; silicon iron=12000; MR-fluid=5) and it is important to remember that the B-H relationship is non-linear, with a saturation of B for values of H above a certain level (the level of H for which B saturates and the saturation value of B being intrinsic material properties). It is however interesting to note that, for modelling purposes, the hypothesis of a linear behavior between B and H (before that saturation occurs) is usually made.

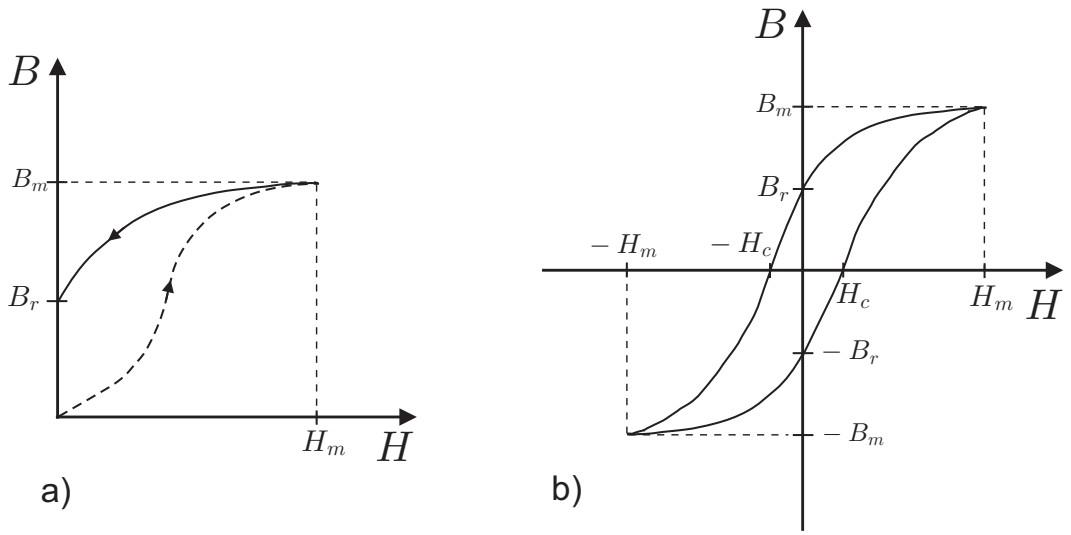

Figure 3.2: B-H curve for a ferromagnetic material: a) magnetization characteristic - b) hysteresis loop (B_r is the remanent flux density; H_c is the coercitive magnetic field)

Figure 3.2 shows the shape of the B-H curve for a ferromagnetic material. When a magnetic field (H) is applied for the first time to such material, the magnetic induction (B) within the material increases slowly at first, then more rapidly, then very slowly again and finally reaches a plateau called saturation (B_m) as can be seen on the dashed curve on Figure 3.2a). Such curve is called the magnetization characteristic and is an intrinsic property of the material.

When H is reduced, B decreases more slowly (plain curve on Figure 3.2a) and when H is reduced to zero, there is still some magnetic flux density in the material, called the remanent flux density (B_r). At this point the material behaves like a permanent magnet. Materials with high B_r values are well suited for permanent magnet applications. They are referred as hard magnetic materials. On the contrary, materials used in the magnetic core of electromagnets should exhibit B_r values as low as possible. These materials are called soft magnetic materials.

If the magnetic field direction is reversed, B becomes zero for a certain value of H called the

coercitive magnetic field (H_c). By increasing and decreasing the magnetic field (H) in both directions, we obtain a loop called hysteresis loop (Figure 3.2b).

Soft magnetic materials can be further classified according to their saturation and relative permeability values. Figure 3.3 compares the five major soft magnetic alloys according to these properties and their cost. For magnetic core applications, materials exhibiting high saturation and high permeability will be preferred since they will respectively lead to more compact devices and lower power requirements.

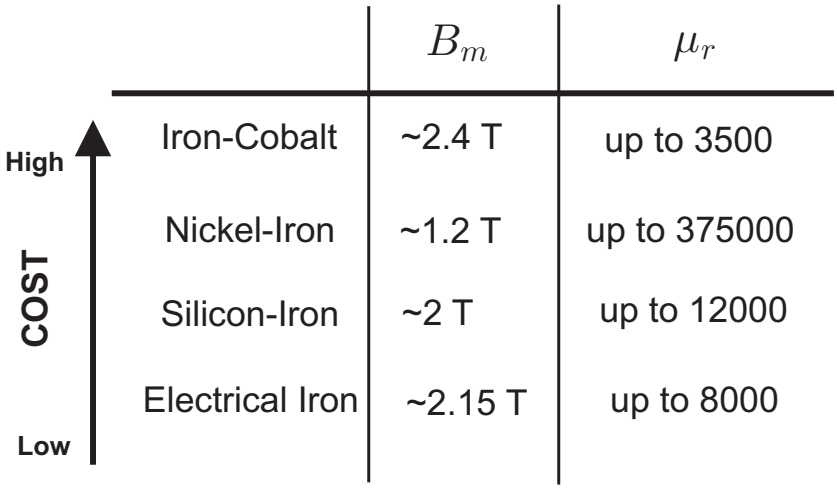

Figure 3.3: Comparison of the properties of ferromagnetic materials - B_m are values of the magnetic flux density at saturation - μ_r are relative permeability values

3.1.3 Magnetic flux and Gauss's law

The magnetic flux (Φ) passing through an open surface (S) is the integral of the induction (B) over this surface. Φ is expressed in Weber [Wb] and is thus given by:

$$\Phi = \int_S \vec{B} \cdot d\vec{S} \tag{3.4}$$

The magnetic flux lines are always continuous. This means that the flux penetrating a closed surface is equal to the flux leaving this surface. For a closed surface (S), we thus have:

$$\oint_S \vec{B} \cdot d\vec{S} = 0 \tag{3.5}$$

3.1.4 Magnetic circuits and electrical analogy

As mentioned before, Ferromagnetic materials have relative permeabilities (μ_r) much larger than other materials. Consequently, in such materials, the flux density $B = \mu H = \mu_0 \mu_r H$ is, for a given H, much larger than what would result in vacuum (or air).

Consider the soft iron core having a constant cross-section (A) represented at Figure 3.4a) with a coil (N turns and current I) winded around a small portion of it. Despite the fact that the coil is not distributed over the whole iron core, the NI of the coil causes a magnetic flux Φ which follows the core (the flux prefers the core than the surrounding space). In first approximation, it may be assumed that all the flux remains within the core and that it is uniformly distributed over the cross section of the core. Such configuration is called a magnetic circuit due to its analogy with electric circuits where the current flows exclusively through the conductor.

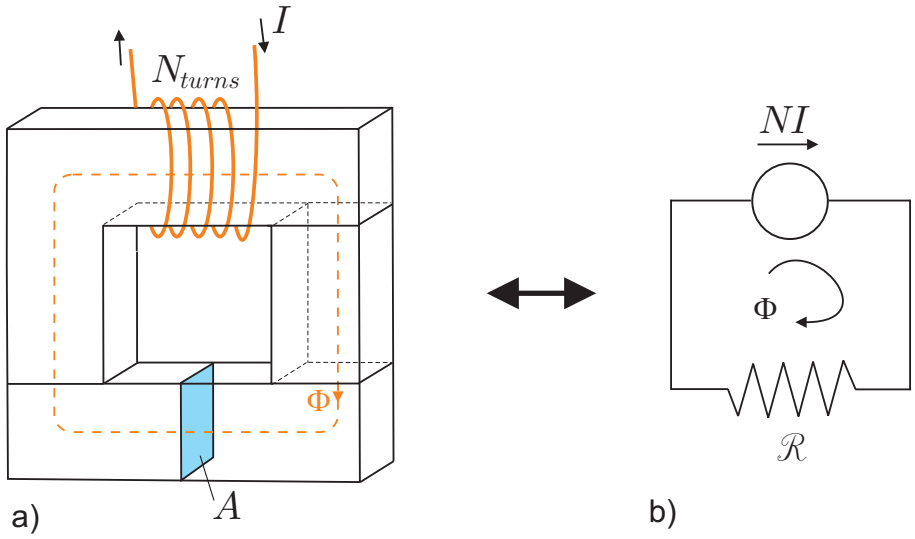

Figure 3.4: Magnetic flux inside a soft steel core

If we apply Ampere's law to this circuit, along the path in the center of the magnetic core, we obtain:

$$\mathscr{F} = NI = \oint \vec{H}.\vec{dl} \tag{3.6}$$

From Gauss law, in a given section A of the magnetic circuit, we get:

$$\Phi = \int_A \vec{B} \cdot \vec{dS} \tag{3.7}$$

If A is constant over the whole magnetic circuit and since Φ remains constant, B is also assumed constant. Eq. 3.7 becomes:

$$\Phi = BA \tag{3.8}$$

From the B-H relationship, H is also constant over the whole circuit and Eq. 3.6 becomes:

$$NI = Hl = \frac{B}{\mu} l \tag{3.9}$$

where l is the length of the magnetic path. By combining Eq. 3.8 and 3.9, one gets:

$$\Phi = \frac{NI}{l/\mu A} = \frac{\mathscr{F}}{l/\mu A} \tag{3.10}$$

If we consider the magnetic flux (Φ) and the magnetomotive force ($\mathscr{F}$) in this magnetic circuit analogous to the current (I) and the applied electromotive force (V) in an electric circuit, ($l/\mu A$) is analogous to the resistance of the electric circuit; it is defined as the *reluctance* of the magnetic circuit :

$$\mathscr{R} = l/\mu A \tag{3.11}$$

Eq. 3.10 can thus be rewritten as:

$$\mathscr{F} = \mathscr{R}\Phi \tag{3.12}$$

which is referred as the Ohm's law for magnetic circuits. The magnetic circuit of Figure 3.4a) can thus be represented by its electric equivalent (Figure 3.4b).

The analogy with electric circuits is so strong that the laws that were initially obtained for electric circuits are also valid for magnetic circuits. The equivalent of Kirchhoff's current law for magnetic circuits is derived from Gauss's law and applies to the magnetic flux (Φ) instead of the electric current (I):

$$\sum_{k=1}^{n} \Phi_k = 0 \tag{3.13}$$

where n is the total number of magnetic flux flowing towards or away from the node (Figure 3.5a). Kirchhoff's voltage law can also be transposed for magnetic circuits. Indeed, by applying the Ampere's law to a closed magnetic circuit, we get:

$$\sum_{k=1}^{n} \mathscr{F}_k = \sum_{k=1}^{m} (\mathscr{R}\Phi)_k \tag{3.14}$$

where n is the number of applied magnetomotive forces and m is the number of NI drops. This last equation thus means that the sum of the magnetomotive forces applied to a closed magnetic circuit is equal to the sum of the NI drops within this circuit (Figure 3.5b).

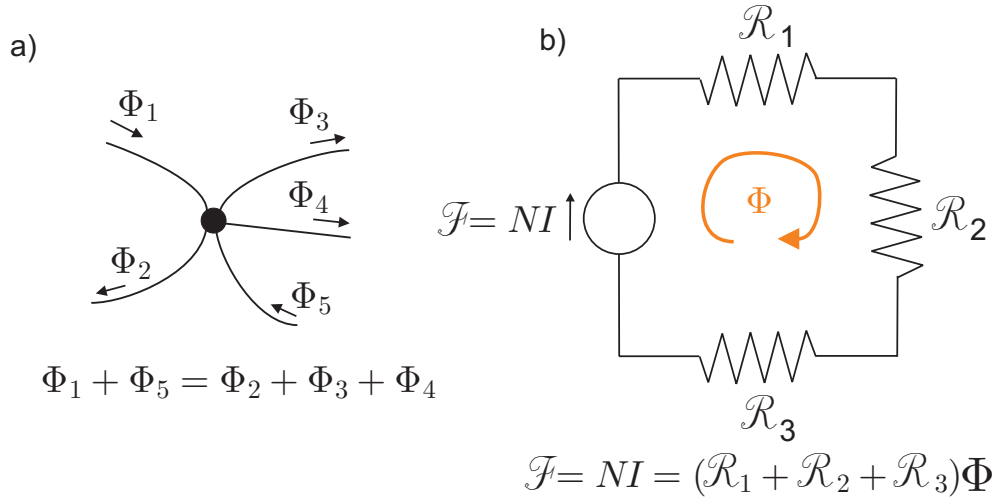

Figure 3.5: Magnetic analogy of: a) Kirchhoff's current law - b) Kirchhoff's voltage law

3.1.5 Permanent magnets

B-H curves of permanent magnets are characterized by high remanent flux density (B_r) and coercitive magnetic field (H_c). The *B-H* curve in the second quadrant is called the *demagnetization curve*, it determines the suitability of the magnet for a given application.

Depending on the magnet material and external temperature conditions, the ideal shape of the *B-H* curve can either be as shown in Figure 3.6a) or in Figure 3.6b). It is interesting to note that, except at the singularities, the slope of both *B-H* curves is equal to μ_0. The value of H at the singularities is called the *intrinsic coercivity* of the material (H_{ci}).

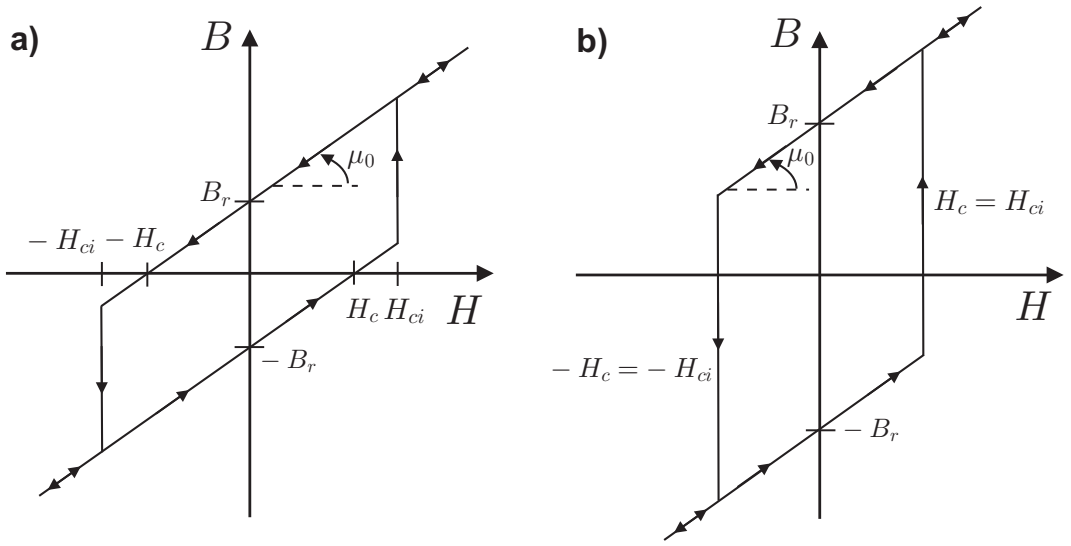

Figure 3.6: Shape of *B-H* curves for permanent magnets [adapted from (Campbell, 1994)] (B_r is the remanent flux density; H_c is the coercitive magnetic field)

For permanent magnets exhibiting a *B-H* curve like in Figure 3.6a), the portion of the curve in the second quadrant is entirely linear, the knee occurring at $-H_{ci}$ being located in the third quadrant. As it will be explained later on, this configuration is preferable to that of Figure 3.6b).

Figure 3.7 shows the demagnetization curves of two types of permanent magnets at various temperatures. The demagnetization curve of the Ceramic 8 magnet is non-linear except when the temperature is well above room temperature. In this case, the knee in the *B-H* curve moves to the third quadrant. On the contrary, the demagnetization curve of the rare-earth (Nd,Dy)-Fe-B magnet is linear except at high temperatures. Furthermore, it can be observed that all curves, for both materials, exhibit the same slope in their linear part ($\approx \mu_0$). It can also be seen that the characteristics of the permanent magnet (B_r,H_c) are highly dependent on the magnet material.

In order to illustrate the selection of a permanent magnet for a specific application, consider the simple magnetic circuit of Figure 3.8a) composed of a magnet and an air gap.

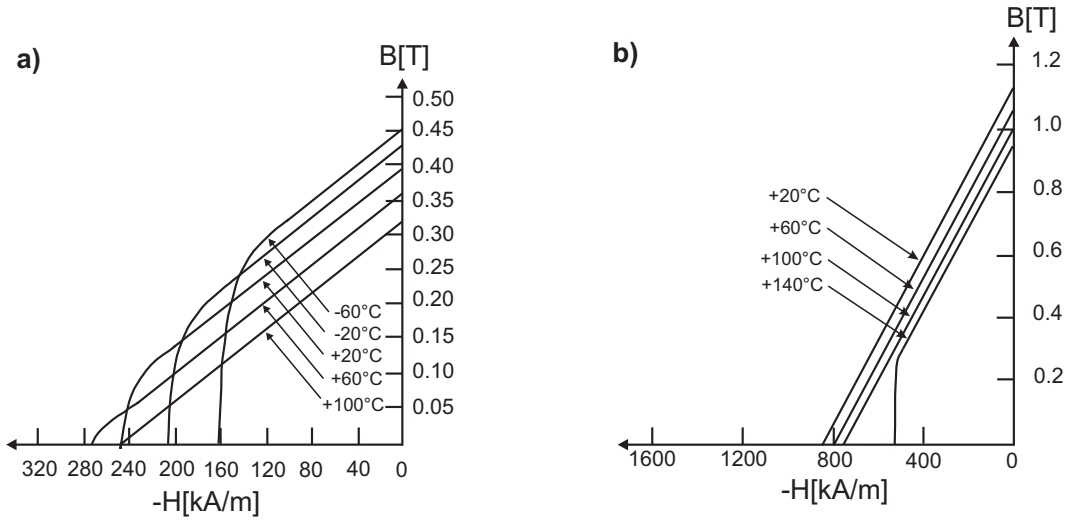

Figure 3.7: Demagnetization curves for: a) Ceramic grade 8 magnet - b) (Nd,Dy)-Fe-B magnet at various temperatures ([adapted from (Campbell, 1994)]

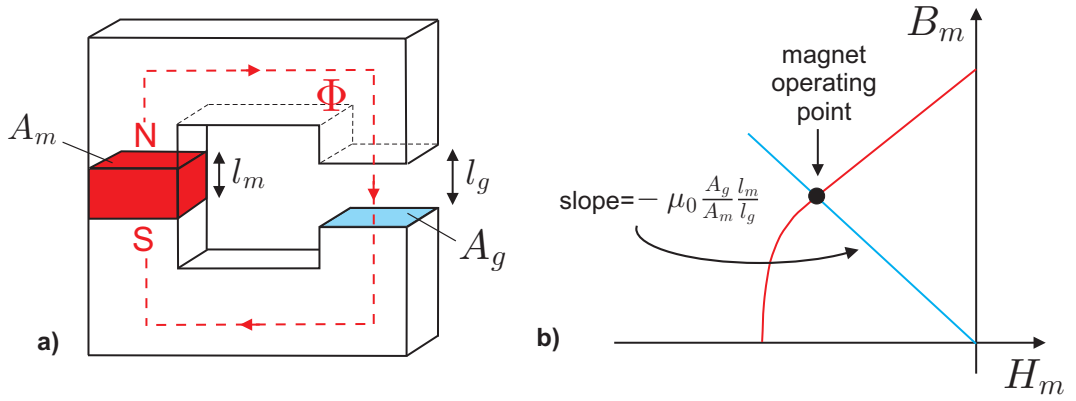

Figure 3.8: a) Circuit with permanent magnet and air gap - b) Corresponding magnet operating point

Thanks to the continuity of the magnetic flux inside the magnetic circuit and by neglecting the leakage flux, we obtain:

$$B_m A_m = B_g A_g \tag{3.15}$$

where B_m and B_g are flux densities and A_m and A_g the cross-sections, respectively in the magnet and in the air gap.

By applying Ampere's law along the path in the center of the magnetic circuit and by neglecting the contribution of the soft iron pole pieces (exhibiting a much higher permeability), we get:

$$H_m l_m + H_g l_g = 0 \tag{3.16}$$

where H_m and H_g are magnetic fields in the magnet and air gap respectively and where l_m and l_g are magnet and air gap lengths. Furthermore, in the air gap, we have:

$$B_g = \mu_0 H_g \tag{3.17}$$

By combining Eq. 3.15 to 3.17, we get:

$$B_m = -\mu_0 \frac{A_g}{A_m} \frac{l_m}{l_g} H_m \tag{3.18}$$

which corresponds to a linear relationship between the magnet parameters B_m and H_m, called the load line of the circuit.

In order to determine the magnet's operating condition, an additional relation between B_m and H_m is required. It is provided by the demagnetization curve of the magnet. The intersection of the load line and the demagnetization curve will thus give the magnet operating point, as shown at Figure 3.8b). It is important to note that the slope of the load line is only dependent of the relative dimensions of magnet and air gap.

Let's now consider a magnetic circuit similar to the previous one but with the addition of a coil (N turns, carrying a current I) generating a magnetic flux in the opposite direction of the one produced by the permanent magnet (Figure 3.9a).

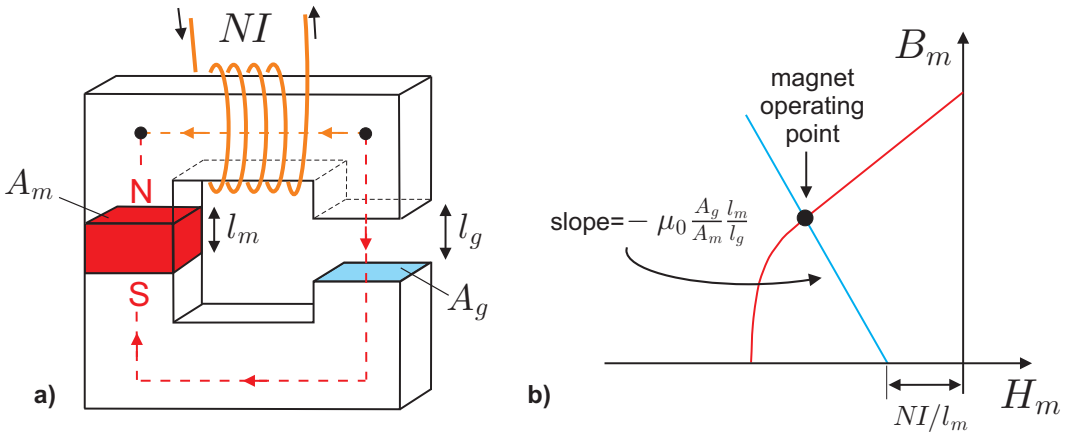

Figure 3.9: a) Circuit with permanent magnet, air gap and coil - b) Corresponding magnet operating point

Eq. 3.16 becomes:

$$H_m l_m + H_g l_g = NI \tag{3.19}$$

Combining Eq. 3.19 with Eq. 3.15 and 3.17 leads to a modified load line, which includes coil excitation:

$$B_m = -\mu_0 \frac{A_g}{A_m} \frac{l_m}{l_g} \left(H_m - \frac{NI}{l_m} \right) \tag{3.20}$$

The shape of this new load line remains unchanged but its position is now determined by the coil excitation, its intersection with the H_m axis being displaced by NI/l_m as shown in Figure 3.9b).

It is important to note that the position of the operating point on the demagnetization curve is of prime importance. Indeed, if it falls below the knee of the curve, an irreversible demagnetization takes place due to a lost of alignement of the magnetic domains within the material. Only full remagnetization of the material (by applying an external magnetic field equal to H_{ci}) can restore the initial magnet properties.

Two processes can be at the origin of magnet demagnetization. The first one is due to changes in the shape of the demagnetization curve with temperature. Indeed, even if the operating point is above the knee of the curve at a given temperature, it may fall below the knee of the curve if temperature changes leading to an irreversible reduction of the magnetization.

The impact of temperature on the shape of the demagnetization curve is highly dependent on the magnet material (Figure 3.7). It should thus be properly selected according to its foreseen temperature operating range. The magnet dimensions (l_m and A_m) also play a role since they influence the load line slope, which has to be increased as much as possible to be more robust to temperature changes. Furthermore, it should be noticed that each magnet material is characterized by a Curie temperature (T_c) at which thermal agitation is such that magnetic domains lose their alignment and randomize leading to a full demagnetization of the magnet, whatever the load line slope.

The second process leading to magnet demagnetization results from the movement of the operating point along the demagnetization curve due to either changes in gap geometry or in the applied coil excitation during what is called dynamic operation.

Indeed changes in gap geometry will affect the slope of the load line. Increasing gap length (l_g) or decreasing gap cross-section (A_g) will reduce the load line slope and the magnet operating point may fall below the knee of the demagnetization curve. Increasing the coil excitation (NI) will cause the load line to move to the left, also increasing the chances that the operating point falls below the knee of the curve.

From Figure 3.10, it can be observed that if the operating point falls below the knee of the curve (point b), returning to the initial conditions (geometry or applied excitation) will not make the operating point return to (a) but to (c) along a "minor" demagnetization curve. Point (c) is characterized by lower B_m and H_m values due to partial magnet demagnetization. Subsequent application and removal of the same load line disturbance will cause the magnet to operate reversibly along the minor curve, between (b) and (c).

It can thus be observed that, here again, increasing the magnet length will be useful since it may compensate for the load line slope decrease due to to changes in gap geometry and also decrease the magnitude of the lateral translation of the load line due to a change in the coil excitation.

The selection and design of a magnet is thus a process involving many parameters. If com-

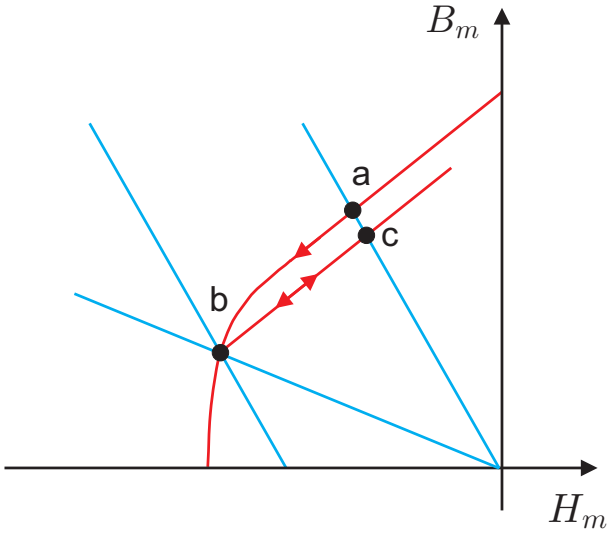

Figure 3.10: Impact of changes of gap geometry or coil excitation on magnet operating point [adapted from (Campbell, 1994)]

pactness is a concern, magnet materials exhibiting high B_r values, such as rare earth magnets, should be selected. However, knowing the magnet operating temperature range, it should be checked that the operating point of the magnet does not fall below the knee of the demagnetization curve in both static and dynamic operation, which means that all changes in gap geometry and applied external coil excitation should be known. This requirement will define the magnet length. The magnet cross-section will be defined by the magnetic flux required in the gap.

It is also useful to characterize a magnet by its electric equivalent. For that purpose, we make the assumption that the demagnetization curve of the magnet is completely linear (which is the case for rare earth magnets at room temperature). We thus have:

$$B_m = \mu_0 H_m + B_r \tag{3.21}$$

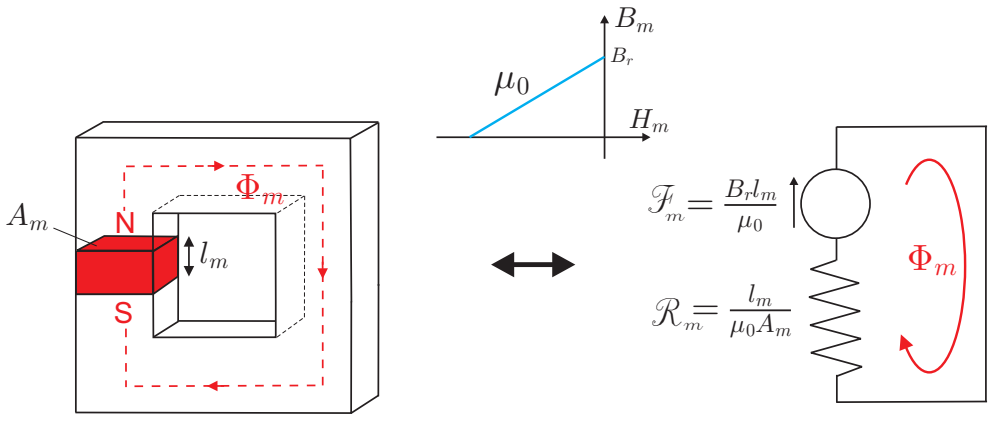

Figure 3.11: Electric equivalent of a permanent magnet

Let's consider the simple magnetic circuit of Figure 3.11a). Ampere's law applied to this circuit gives (contribution the iron core neglected):

$$H_m l_m = 0 \tag{3.22}$$

Combining Eq. 3.21 and 3.22 gives:

$$\frac{B_r l_m}{\mu_0} = \frac{B_m l_m}{\mu_0} \tag{3.23}$$

that can be rewritten as:

$$\frac{B_r l_m}{\mu_0} = \frac{l_m}{\mu_0 A_m}\Phi_m \tag{3.24}$$

or:

$$\mathscr{F}_m = \mathscr{R}_m \Phi_m \tag{3.25}$$

A permanent magnet is thus equivalent to its reluctance ($\mathscr{R}_m = l_m/\mu_0 A_m$) in series with a magnetomotive force ($\mathscr{F}_m = B_r l_m/\mu_0$) proportional to its length (l_m) and remanent flux density (B_r) (Figure 3.11b).

3.2 Magnetic circuits with MR-fluids

3.2.1 Magnetic core with MR-fluid filled gap

This configuration corresponds to the situation where an electromagnet is used to control the apparent viscosity of the MR-fluid (Figure 3.12a). When no current is applied to the coil, the MR-fluid apparent viscosity is minimum.

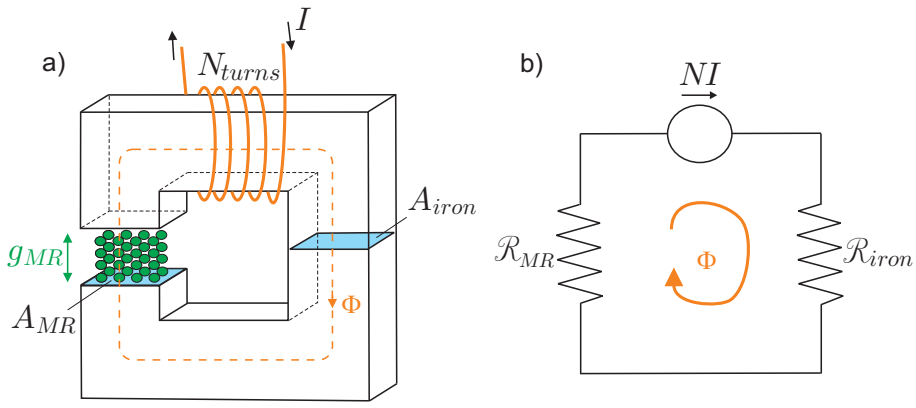

Figure 3.12: Magnetic core with MR-fluid filled gap : a) magnetic circuit - b) electric equivalence [adapted from (Carlson, 2007)]

The equivalent electric circuit is shown at Figure 3.12 b). The equivalent Kirchhoff's voltage law gives:

$$NI = (\mathscr{R}_{MR} + \mathscr{R}_{iron})\Phi \tag{3.26}$$

leading to:

$$\Phi = \frac{NI}{\mathscr{R}_{MR} + \mathscr{R}_{iron}} = \frac{NI}{(g_{MR}/\mu_{MR}A_{MR}) + (l_{iron}/\mu_{iron}A_{iron})} \tag{3.27}$$

which is equivalent to:

$$H_{MR} = \frac{\Phi}{\mu_{MR}A_{MR}} = \frac{NI}{g_{MR} + l_{iron}\,(\mu_{MR}/\mu_{iron})\,(A_{MR}/A_{iron})} \tag{3.28}$$

It is however important to note that $\mu_{iron} \approx 1000\mu_{MR}$. Consequently, provided that l_{iron} is not too large and that the MR-fluid and soft-steel core sections are in the same range, Eq. 3.27 can be simplified to:

$$\Phi = \frac{NI}{\mathscr{R}_{MR}} \tag{3.29}$$

which is equivalent to:

$$H_{MR} = \frac{NI}{g_{MR}} \tag{3.30}$$

3.2.2 Magnetic core with MR-fluid filled gap and permanent magnet

This configuration corresponds to the situation where an electromagnet is used in combination with a permanent magnet to control the viscosity of the MR-fluid (Figure 3.13a). The permanent magnet is used to shift the off-state (no current in the coil) viscosity of the MR-fluid to a selected value and the electromagnet is used to control the viscosity variations around this value. A frequent situation is that where the magnetic circuit is designed in such a way that the MR-fluid viscosity is maximum when no current flows through the coil. This is particularly useful when the device based on such magnetic circuit has to be blocked the major part of its operation time (such as in release mechanisms, for instance).

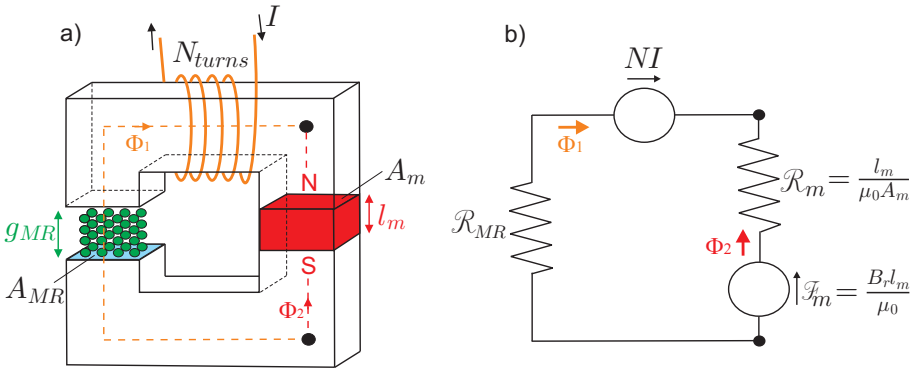

Figure 3.13: Magnetic core with MR-fluid filled gap and permanent magnet : a) magnetic circuit - b) electric equivalence [adapted from (Carlson, 2007)]

The equivalent electric circuit is shown at Figure 3.13b). The equivalent Kirchhoff's voltage law gives:

$$NI - \mathscr{R}_{MR}\Phi_1 = \mathscr{F}_m - \mathscr{R}_m\Phi_2 \tag{3.31}$$

The equivalent Kirchhoff's current law gives:

$$\Phi_1 + \Phi_2 = 0 \tag{3.32}$$

By combining Eq. 3.31 and 3.32, we obtain:

$$\Phi_1 = \frac{NI - \mathscr{F}_m}{\mathscr{R}_{MR} + \mathscr{R}_m} \tag{3.33}$$

By replacing $\mathscr{F}_m$, $\mathscr{R}_{MR}$ and $\mathscr{R}_m$ by their full expression, it can be shown that Eq. 3.33 is equivalent to:

$$H_{MR} = \frac{(\mu_0\mu_r/l_m)\,NI - B_r}{\mu_0\left[\mu_r(g_{MR}/l_m) + \mu_{MR}(A_{MR}/A_m)\right]} \tag{3.34}$$

In order to cancel the flux inside the MR-fluid, NI has to be equal to $\mathscr{F}_m$, which is highly influenced by the magnet length (the magnet more or less behaves like an air gap inside the magnetic circuit, $\mu_r \cong 1$). It should however be noticed that such a magnetic circuit will not be used in practice since it might lead to demagnetization of the permanent magnet, as described in section 3.1.5. A solution to this problem is to include a secondary path inside the magnetic circuit (Figure 3.14a).

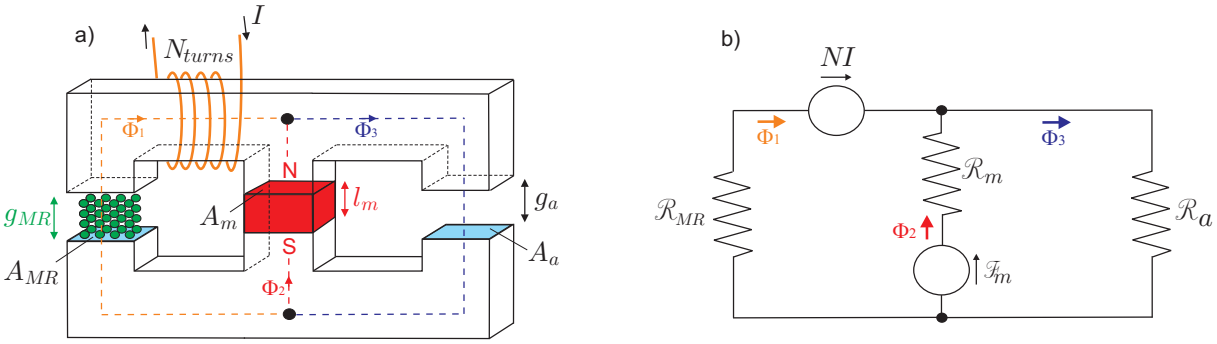

Figure 3.14: Magnetic core with MR-fluid filled gap and permanent magnet with secondary path : a) magnetic circuit - b) electric equivalence

The electromagnet will thus not be used to completely cancel the flux produced by the permanent magnet but will only redirect it to the secondary path. This secondary path comprises a higher reluctance air gap in order to concentrate the major part of the flux generated by the permanent magnet in the primary path (comprising the MR-fluid gap) when no current is flowing through the coil. Figure 3.15 compares the situation with no current in the coil and maximum current flowing through the coil.

The equivalent electric circuit is shown in Figure 3.14b). Kirchhoff's laws give:

$$\mathscr{R}_a\Phi_3 = \mathscr{F}_m - \mathscr{R}_m\Phi_2 = NI - \mathscr{R}_{MR}\Phi_1 \tag{3.35}$$

$$\Phi_3 = \Phi_1 + \Phi_2 \tag{3.36}$$

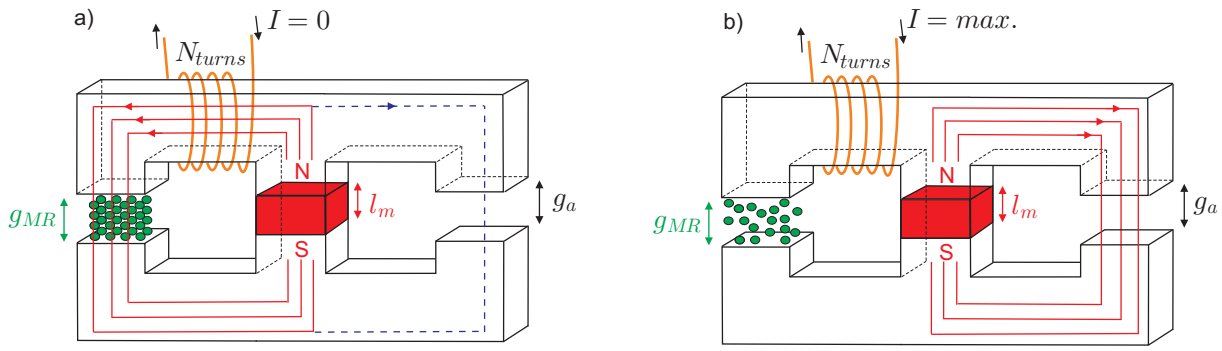

Figure 3.15: Flow of the magnetic flux inside the magnetic circuit when the current inside the coil is: a) null - b) maximum

By combining Eq. 3.35 and 3.36, we obtain:

$$\Phi_1 = \frac{NI - \left(\frac{\mathscr{R}_a}{\mathscr{R}_m + \mathscr{R}_a}\right)\mathscr{F}_m}{\left(\frac{\mathscr{R}_a}{\mathscr{R}_m + \mathscr{R}_a}\right)\mathscr{R}_m + \mathscr{R}_{MR}} \tag{3.37}$$

which is equivalent to:

$$H_{MR} = \frac{NI\left(\frac{A_a \mu_0 \mu_a}{A_m g_a} + \frac{\mu_0 \mu_r}{l_m}\right) - B_r}{\frac{A_a}{A_m}\frac{g_{MR}}{g_a}\mu_0\mu_a + \frac{g_{MR}}{l_m}\mu_0\mu_r + \left(\frac{A_{MR}}{A_m}\right)\mu_0\mu_{MR}} \tag{3.38}$$

It is interesting to note that, if $g_a \to \infty$, we come back to Eq. 3.34 obtained for a magnetic circuit without secondary path.

In order to cancel the magnetic flux inside the MR-fluid gap, we need:

$$NI = \frac{\mathscr{F}_m}{\left(1 + \frac{\mathscr{R}_m}{\mathscr{R}_a}\right)} \tag{3.39}$$

which is equivalent to:

$$NI = \frac{B_r l_m}{\mu_0 \mu_r \left[\left(\frac{A_a}{A_m}\right)\left(\frac{l_m}{g_a}\right)\left(\frac{\mu_a}{\mu_r}\right) + 1\right]} \tag{3.40}$$

This value may seem smaller than what was obtained in the previous case; however, to obtain the same magnetic field inside the MR-fluid gap, the magnet has to be more powerful since it has to compensate for the loss of magnetic flux in the secondary circuit. For a given A_m value, it will lead to an increase of l_m as compared to the previous case, leading to an unchanged NI value.

3.2.3 Fringing in air and fluid gaps

Up to now, we have considered the section of air and fluid gaps located inside the magnetic circuit as being equal to the section of the soft steel core located at the interface with the

gap. However, this is not completely correct since fringing of magnetic flux appears at the interface between the gap and the soft iron core (Figure 3.16a). Consequently, the magnetic field inside the gap is lower than expected.

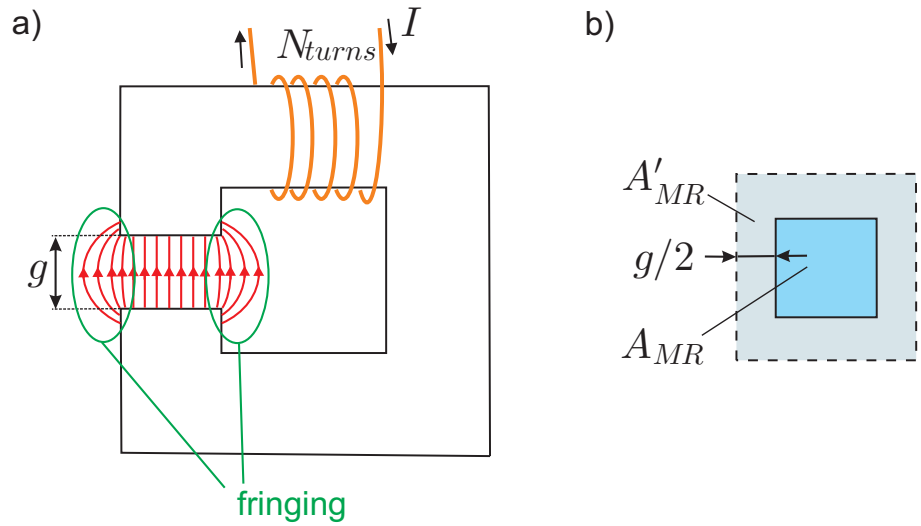

Figure 3.16: a) Fringing of magnetic flux lines at the interface with a MR-fluid gap - b) Core cross-section and effective gap section

In order to take the effect of fringing into account during the design process, one should consider an effective gap section (A'_{MR} or A'_a) larger than the cross-section of the soft steel core located at the interface with the gap (A_{MR} or A_a). For magnetic circuits having a square cross-section, a good approximate of the effect of fringing can be obtained by adding the gap length to each side of the square (Figure 3.16b).

3.3 References

P. Campbell. *Permanent Magnet Materials and their Application.* Cambridge university press, 1994.

J.D. Carlson. Semi-active vibration supression. In *CISM Course: Semi-Active Vibration Suppression - the Best from Active and Passive Technologies*, Udine, October 2007.

J. A. Edminister. *Schaum's Outline of Theory and Problems of Electromagnetics (2nd Edition).* McGraw-Hill, 1993.

Chapter 4

MR-brake architectures

Five major brake designs have been identified: drum brake, disk brake, inverted drum brake, T-shaped rotor brake and multiple disks brake (Figure 4.1). To our knowledge, a quantitative comparison of these architectures is not available in the literature. This is the purpose of this chapter.

4.1 Figures of Merit

The various designs can be compared with the following figures of merit:

- Dynamic Range (maximum torque/off-state torque)(seal friction not considered)
- Torque/Volume (T/V) ratio
- Rotor radius (for a given torque)
- Electric power consumption

The dynamic range and the torque to volume ratio must be maximized; the rotor radius may not exceed some critical value for some applications (e.g. knee prosthesis) and the electric power must be kept to a minimum.

For every architecture, the order of magnitude of these quantities may be evaluated with a simple analytical model, assuming a uniform distribution of the magnetic flux density B within any cross-section, no fringing, and that the value of B_{iron} and B_{MR} are just below saturation. The basic equations are:

(a) The conservation of the magnetic flux within every cross-section (BA=constant)

(b) Ampere's law: $NI = \oint \vec{H} d\vec{l}$

(c) The braking torque induced by the magnetic field can be calculated with Bingham's model assuming that the shear stress, $\tau_y(H)$, is constant over the active MR area (A):

$$T_\tau = \int_A r\tau_y dA \tag{4.1}$$

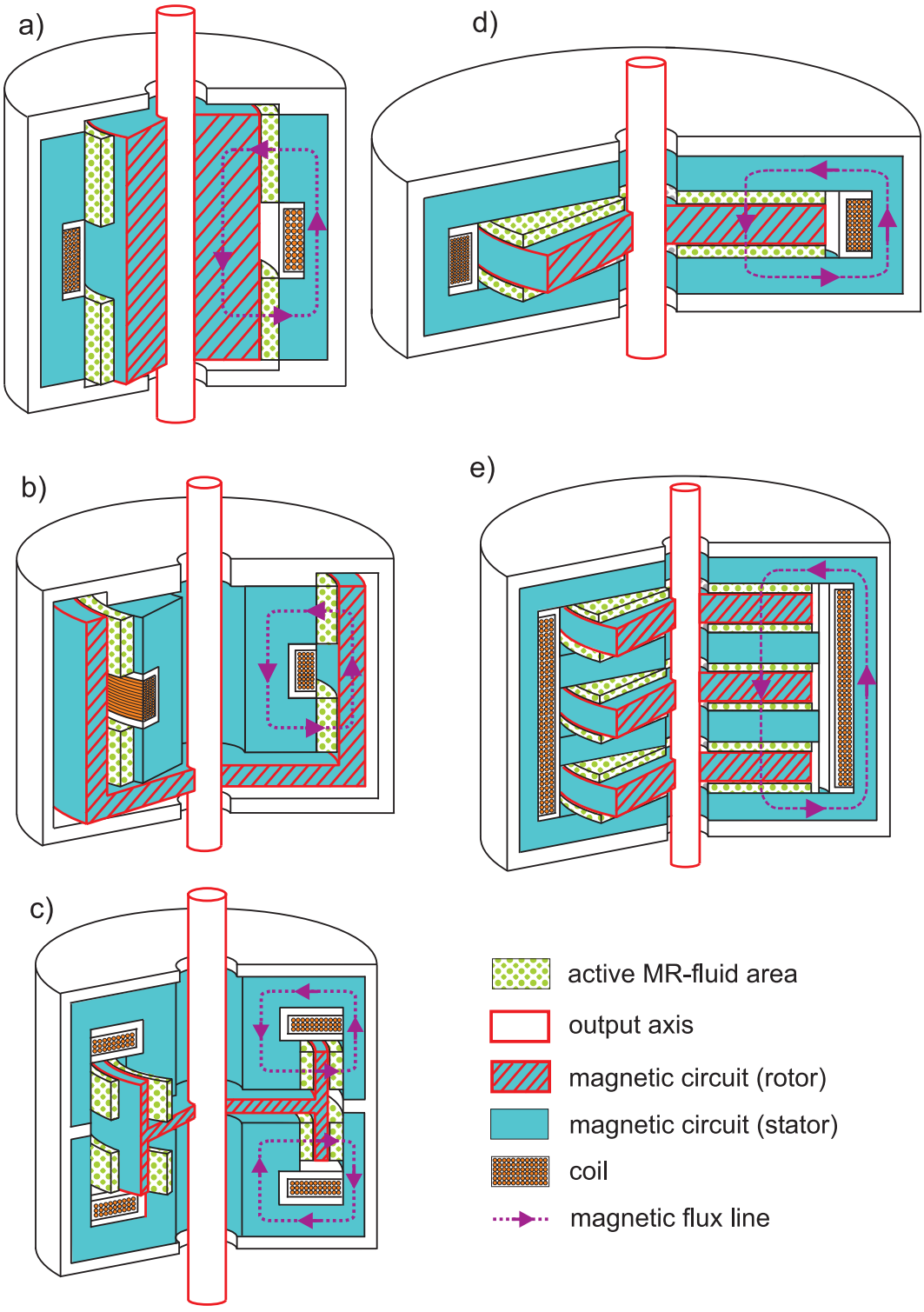

Figure 4.1: Major MR-brake designs: a) drum - b) inverted drum - c) T-shaped rotor - d) disk - e) multiple disks

4.2 Drum brake and inverted drum brake

Drum brakes are, with the disk brakes, the easiest designs to manufacture. The rotor has a cylindrical shape and the magnetic field is applied in the radial direction. However, despite their high geometric simplicity, such brakes are, in this form, not so common in the literature. (Huang et al., 2002) gives some of the analytical expressions that guide their design and LORD corporation uses them as an example in a tutorial about the design of devices making use of MR-fluids (LORD, 1998).

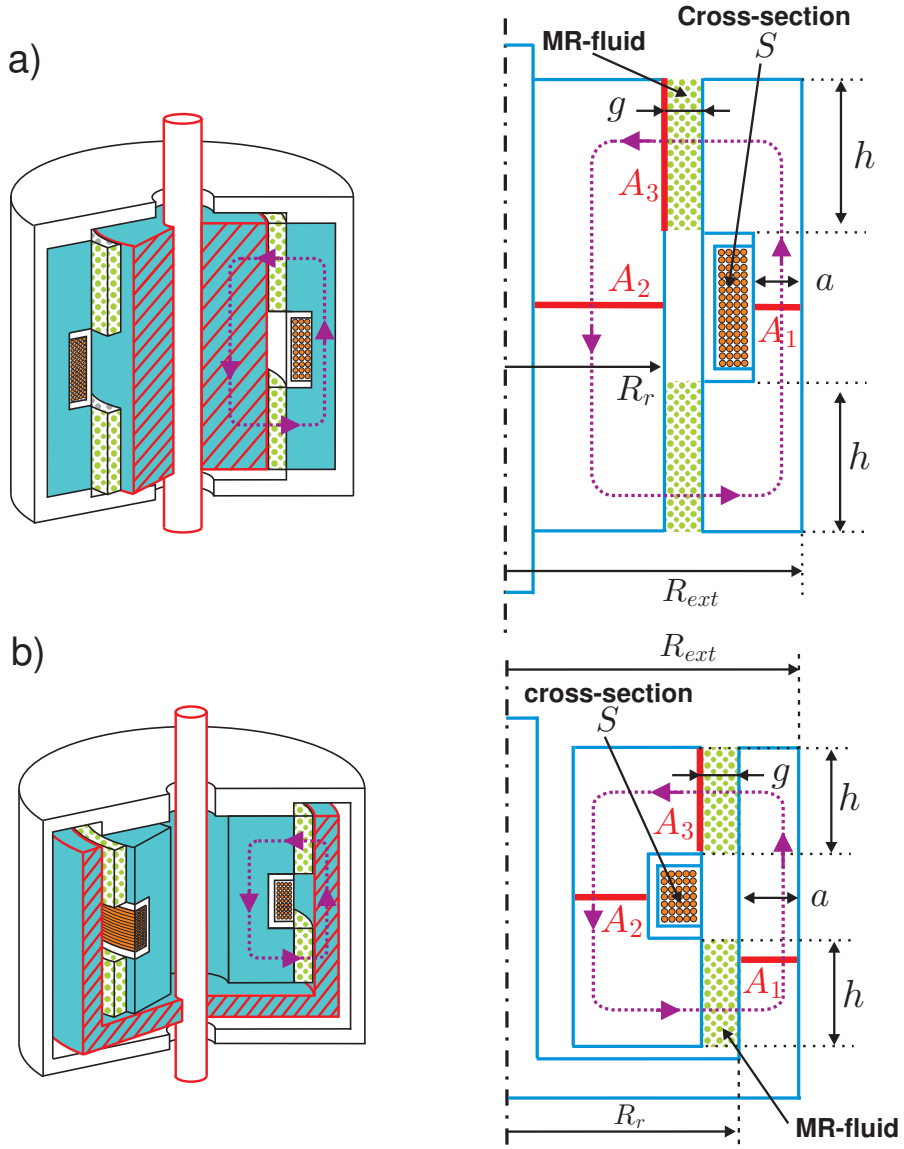

Figure 4.2: a) Drum brake - b) Inverted drum brake

The drum design is characterized by a large inertia, which motivated the inverted drum geometry. This inertia may also be reduced by reshaping its inner part in regions of lower magnetic flux (Jolly et al., 2005).

The inverted drum design is used in a wide variety of applications such as a 40Nm clutch prototype for a truck fan drive developed by General Motors (Smith et al., 2007) or in a brake with integrated flywheel to be used in muscular exercise equipments (Carlson, 2001). The relative compactness of this design in terms of external diameter was also exploited in a prototype of programmable haptic knob (Ackermann and Elferich, 2000).

Drum brakes and inverted drum brakes can be described by the same analytical model.

From Figure 4.2, the maximum field-induced torque is given by:

$$T_\tau = 2R_r \cdot (2\pi R_r h) \cdot \tau_y = 4\pi h \tau_y R_r^2 \tag{4.2}$$

where τ_y is the maximum shear stress of the MR-fluid. Similarly, the off-state viscous torque is calculated by using the viscous shear model, $\tau = \eta\dot{\gamma} = \eta R_r \dot{\theta}/g$; this leads to

$$T_\eta = 4\pi h \eta \frac{\dot{\theta}}{g} R_r^3 \tag{4.3}$$

where η is the fluid viscosity in the absence of magnetic field. Combining (4.2) and (4.3), the dynamic range is given by:

$$\frac{T_\tau}{T_\eta} = \frac{\tau_y}{\eta} \cdot \frac{1}{R_r} \cdot \frac{g}{\dot{\theta}} \tag{4.4}$$

A rotation velocity of $\dot{\theta} \approx 1$ rad/sec may be considered as typical for rehabilitation devices. This equation does not include the friction torque from the seal used to close the MR-fluid cavity.

The thickness of the iron, h may be related to the radius R_r by expressing the conservation of the magnetic flux within the two sections marked A_2 and A_3. Assuming uniform flux densities, one gets

$$B_{iron}.A_2 = B_{MR}.A_3 \tag{4.5}$$

or

$$B_{iron}.\pi R_r^2 \approx B_{MR}.2\pi R_r h \tag{4.6}$$

This equation gives the relationship between the thickness of the stator h and the radius of the brake:

$$h \approx \frac{B_{iron}}{B_{MR}} \cdot \frac{R_r}{2} = \frac{1}{\alpha}\frac{R_r}{2} \tag{4.7}$$

$\alpha = B_{MR}/B_{iron}$ express the ratio between the magnetic the flux densities right before saturation; it depends on the quality of the magnetic material and the particle volume fraction in the fluid (for the materials used in this study, $\alpha = B_{MR}/B_{iron} \approx 1/2$ leading to $h \approx R_r$).

Combining Eq. (4.2) and (4.7) gives the relationship between the maximum braking torque and the radius of the brake

$$R_r = \left(\frac{\alpha}{2\pi} \cdot \frac{T_\tau}{\tau_y} \right)^{1/3} \tag{4.8}$$

For $\alpha = 1/2$, one gets

$$R_r = \left(\frac{1}{4\pi} \cdot \frac{T_\tau}{\tau_y} \right)^{1/3} \tag{4.9}$$

By expressing the conservation of magnetic flux in sections A_1 and A_2, one gets

$$B_{iron}.A_1 = B_{iron}.A_2 \tag{4.10}$$

or

$$2\pi R_r a \approx \pi R_r^2 \tag{4.11}$$

that is

$$a \approx \frac{R_r}{2} \tag{4.12}$$

Drum and inverted drum brakes have the shape of a cylinder of approximate radius $R_{ext} = R_r + a$ and height $2h$. The volume is

$$V \approx \pi R_{ext}^2.2h = \frac{9}{4}\frac{1}{\alpha}\pi R_r^3 \tag{4.13}$$

For $\alpha = 1/2$, this leads to

$$V \approx \frac{9}{2}\pi R_r^3 \tag{4.14}$$

Since the magnetic material (iron) makes up most of the device, the mass of the brake is obtained easily by multiplying by the iron density. Combining (4.2) and (4.14), the torque to volume ratio is

$$\frac{T_\tau}{V} \approx \frac{8}{9}\tau_y \tag{4.15}$$

The magnetomotive force, NI, results from Ampere's law, $NI = \oint Hdl$. However, since the magnetic constant of the iron is much bigger (1000 times) than that of the MR fluid ($\mu_{iron} >> \mu_{MR}$), leading to $H_{MR} >> H_{iron}$, the integral is dominated by the contribution of the fluid gap:

$$NI \approx H_{MR}.2g \tag{4.16}$$

Thus, the magnetomotive force requirement is obtained by setting H_{MR} equal to the magnetic field right before saturation. It is a linear function of the fluid gap g.

If S is the cross-section available for the coil and d is the diameter of the wire, the number of turns is given by

$$N = \frac{4S}{\pi d^2} \tag{4.17}$$

and the resistance r of the of the wire (of length $l \approx 2\pi R_r N$)

$$r = \frac{\rho l}{\pi d^2/4} = \frac{8\rho R_r N}{d^2} \tag{4.18}$$

where ρ is the resistivity of the coil wire material. Thus, the maximum instantaneous electrical power dissipated by the brake is

$$W_e = rI^2 = \frac{8\rho R_r N}{d^2} I^2 = \frac{8\rho R_r}{d^2 N}(NI)^2 \tag{4.19}$$

and, substituting NI from (4.16) and d^2N from (4.17), one finds

$$W_e = \frac{2\pi\rho R_r}{S} \cdot (H_{MR} \cdot 2g)^2 = CR_r \cdot (H_{MR} \cdot 2g)^2 \tag{4.20}$$

where $C = 2\pi\rho/S$. The electrical power dissipated grows with the square of the total gap $2g$ in the magnetic circuit, and linearly with the radius R_r. Combining with (4.9), the electrical power is related to the maximum torque according to

$$W_e \approx \frac{2\pi\rho}{S} \cdot \left(\frac{1}{4\pi} \cdot \frac{T_\tau}{\tau_y}\right)^{1/3} (H_{MR} \cdot 2g)^2 \tag{4.21}$$

4.3 T-shaped rotor brake

The T-shaped rotor brake is more compact than the drum designs but more complex to manufacture (due to the thin strip at the extremity of the rotor).

Despite its high compactness, this design is not so common in the literature. (York et al., 1997) gives a first example used as a torque load simulator system exhibiting a very high torque (135Nm) with a relatively compact design (rotor diameter: 150mm). The double MR-fluid gap configuration was also discussed by (Bölter and Janocha, 1997) describing generic design rules for MR-fluid actuators, with emphasis on the robustness of this design to particle centrifugation. Other authors (Dwivedi et al., 2002) (Lucchesi, 2004) also introduced some design adaptations such as the use of two strips instead of one at the rotor extremity in order to further increase compactness (at the expense of a higher manufacturing complexity).

From Figure 4.3, the maximum field-induced torque is given by:

$$T_\tau = 8\pi h \tau_y R_r^2 \tag{4.22}$$

Similarly, the off-state viscous torque is calculated by using the viscous shear model, $\tau = \eta\dot{\gamma} = \eta R_r \dot{\theta}/g$; this leads to

$$T_\eta = 8\pi h \eta \frac{\dot{\theta}}{g} R_r^3 \tag{4.23}$$

where η is the fluid viscosity in the absence of magnetic field. Combining Eq. (4.22) and (4.23), the dynamic range is given by:

$$\frac{T_\tau}{T_\eta} = \frac{\tau_y}{\eta} \cdot \frac{1}{R_r} \cdot \frac{g}{\dot{\theta}} \tag{4.24}$$

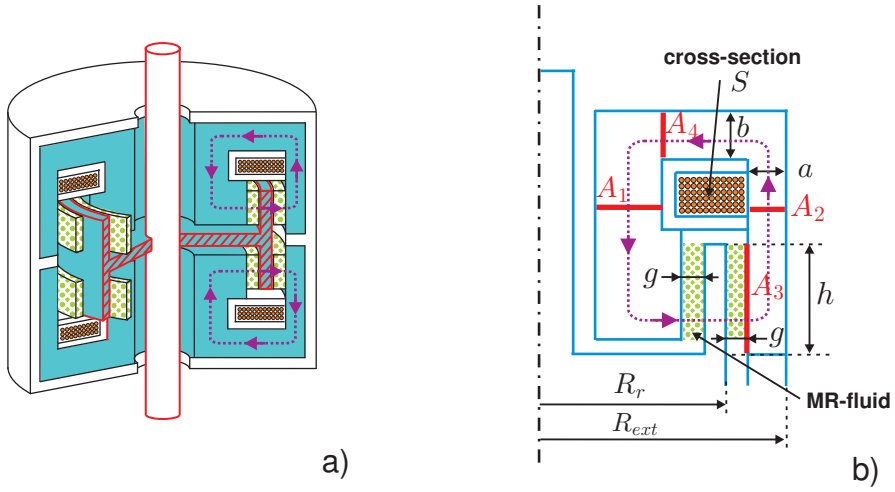

Figure 4.3: T-shaped rotor brake: a) schematic view - b) design parameters

as for drum brakes; the thickness of the iron h may be related to the radius R_r by expressing the conservation of the magnetic flux within the two sections marked A_1 and A_3. Assuming uniform flux densities, one gets

$$B_{iron}.A_1 = B_{MR}.A_3 \tag{4.25}$$

or

$$B_{iron}.\pi R_r^2 \approx B_{MR}.2\pi R_r h \tag{4.26}$$

This equation gives the relationship between the height of the strip at the rotor extremity h and the radius of the brake:

$$h \approx \frac{B_{iron}}{B_{MR}} \cdot \frac{R_r}{2} = \frac{1}{\alpha}\frac{R_r}{2} \tag{4.27}$$

Combining Eq. (4.22) and (4.27) gives the relationship between the maximum braking torque and the radius of the brake

$$R_r \approx \left(\frac{\alpha}{4\pi} \cdot \frac{T_\tau}{\tau_y}\right)^{1/3} \tag{4.28}$$

For $\alpha = 1/2$, one gets

$$R_r \approx \left(\frac{1}{8\pi} \cdot \frac{T_\tau}{\tau_y}\right)^{1/3} \tag{4.29}$$

From this equation, it can be seen that for the same output torque T_τ, the rotor radius of the T-shaped design is about two times smaller than for the drum design.

By expressing the conservation of magnetic flux between A_2 and A_3, one gets

$$B_{iron}.A_2 = B_{MR}.A_3 \tag{4.30}$$

or

$$B_{iron} \cdot 2\pi R_r a \approx B_{MR} \cdot 2\pi R_r h \tag{4.31}$$

that is (with $\alpha = 1/2$)

$$a \approx \alpha h \approx \frac{R_r}{2} \tag{4.32}$$

And, by expressing the conservation of magnetic flux between A_2 and A_4, one gets

$$B_{iron}.A_2 = B_{iron}.A_4 \tag{4.33}$$

or

$$2\pi R_r a \approx 2\pi R_r b \tag{4.34}$$

that is

$$a \approx b \tag{4.35}$$

The brake has the shape of a cylinder of approximate radius $R_r + a$ and height $2(h + b)$. The volume is

$$V \approx \pi R_{ext}^2.2(h+b) = \frac{9}{4}\pi \left(\frac{1}{\alpha} + 1\right) R_r^3 \tag{4.36}$$

For $\alpha = 1/2$, this leads to

$$V \approx \frac{27}{4}\pi R_r^3 \tag{4.37}$$

Combining Eq.(4.22) and (4.37), the torque to volume ratio is

$$\frac{T_\tau}{V} \approx \frac{32}{27}\tau_y \approx \frac{11}{9}\tau_y \tag{4.38}$$

From similar developments than those made for the drum designs, the maximum instantaneous electrical power dissipated by the brake, with coils in parallel or in series, is:

$$W_e = 2rI^2 = \frac{8\pi\rho R_r}{S} \cdot (H_{MR} \cdot 2g)^2 = 4CR_r \cdot (H_{MR} \cdot 2g)^2 \tag{4.39}$$

where $C = 2\pi\rho/S$ and S is the total cross-section available for the coils. The power consumption is thus four times higher than for the drum designs. Combining with (4.29), the electrical power is related to the maximum torque according to

$$W_e \approx \frac{8\pi\rho}{S} \cdot \left(\frac{1}{8\pi} \cdot \frac{T_\tau}{\tau_y}\right)^{1/3} (H_{MR} \cdot 2g)^2 \tag{4.40}$$

4.4 Disk brake

The disk brake is the most common design found in the literature and also the first one that has been described in the seminal work of (Rabinow, 1951). This type of brake is very easy to manufacture and gives reasonably good results in terms of weight and compactness.

The rotor has a disk shape and the magnetic field is applied in the axial direction, perpendicular to the disk surface (Figure 4.4). Some variations to this design can be found in the

literature such as the use of two coils instead of one in order to increase the magnetic pole area (Wong and Liao, 2005) or the relocation of the coils on top of the disk in order to reduce its external diameter (Jolly et al., 2005). Other designs concentrate the magnetic field at the extremity of the disk in order to increase the lever arm of the active MR-fluid area (Li and Du, 2003) (Takesue et al., 2003). Some authors also discuss the shape optimization of the magnetic core in order to further increase its torque/weight ratio (Nam et al., 2007). A nice comparison of various disk brake designs can be found in (Wang et al., 2004) and in (Carlson et al., 1998).

It is also interesting to note that this design is the only one that is commercially available as a standard product manufactured by LORD corporation (MRF132LD, MRB2107-03) and used in many studies such as (Lampe and Grundmann, 2000), (An and Kwon, 2002), (An and Kwon, 2003) and (Sapinski and Bydon, 2003).

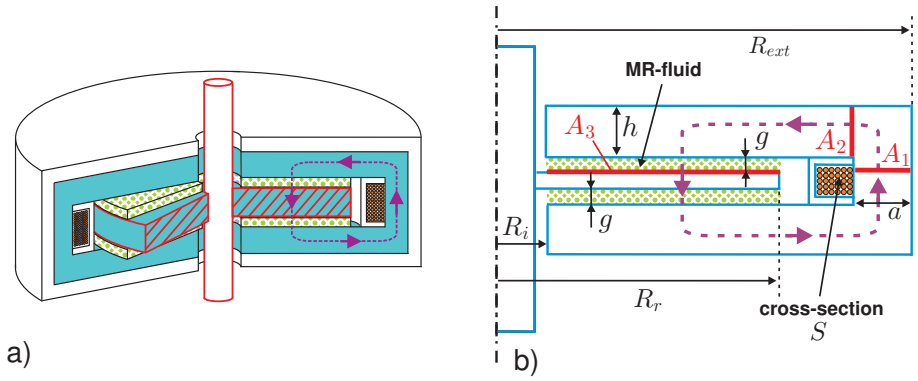

Figure 4.4: Drum brake: a) schematic view - b) design parameters

According to Figure 4.4, the maximum field-induced torque is given by:

$$T_\tau = 2\int_0^{2\pi} d\theta \int_{R_i}^{R_r} r^2 \tau_y dr = \frac{4}{3}\pi\tau_y \left(R_r^3 - R_i^3\right) \approx \frac{4}{3}\pi\tau_y R_r^3 \tag{4.41}$$

where τ_y is the maximum shear stress, assumed uniformly distributed over the active gap. Similarly, the off-state viscous torque is given by:

$$T_\eta \approx \pi\eta\frac{\dot{\theta}}{g}R_r^4 \tag{4.42}$$

where η is the fluid viscosity in the absence of magnetic field. Combining (4.41) and (4.42), the dynamic range is given by:

$$\frac{T_\tau}{T_\eta} = \frac{4}{3}\,\frac{\tau_y}{\eta}\cdot\frac{1}{R_r}\cdot\frac{g}{\dot{\theta}} \tag{4.43}$$

Equation (4.41) also provides the relationship between the maximum braking torque and the radius of the brake.

$$R_r = \left(\frac{3}{4\pi}\frac{T_\tau}{\tau_y}\right)^{1/3} \tag{4.44}$$

The thickness of the iron, h may be related to the radius R_r by expressing the conservation of the magnetic flux within the two sections marked A_2 and A_3. Assuming uniform flux densities, one gets

$$B_{iron}.A_2 = B_{MR}.A_3 \tag{4.45}$$

or

$$B_{iron}.2\pi R_r h = B_{MR}.\pi R_r^2 \tag{4.46}$$

This equation gives the relationship between the thickness of the stator h and the radius of the brake:

$$h = \frac{B_{MR}}{B_{iron}} \cdot \frac{R_r}{2} = \alpha \frac{R_r}{2} \tag{4.47}$$

Similarly, expressing the conservation of magnetic flux in sections A_1 and A_2, one gets

$$B_{iron}.A_1 = B_{iron}.A_2 \tag{4.48}$$

or

$$2\pi R_r a \approx 2\pi R_r h \tag{4.49}$$

that is

$$a \approx h \tag{4.50}$$

The brake has the shape of a cylinder of approximate radius $R_{ext} = R_r + h$ and height $2h$. The volume is

$$V \approx \pi R_{ext}^2.2h = \pi R_r^3 \left(1 + \frac{\alpha}{2}\right)^2 \alpha \tag{4.51}$$

For $\alpha = 1/2$, this leads to

$$V \approx \frac{3}{4}\pi R_r^3 \tag{4.52}$$

Combining (4.41) and (4.52), the torque to volume ratio is

$$\frac{T_\tau}{V} \approx \frac{16}{9}\tau_y \tag{4.53}$$

From similar developments than those made for the drum designs, the electrical power dissipated in the disk brake is given by the same expression:

$$W_e = \frac{2\pi\rho R_r}{S} \cdot (H_{MR} \cdot 2g)^2 = CR_r \cdot (H_{MR} \cdot 2g)^2 \tag{4.54}$$

where $C = 2\pi\rho/S$. As for the drum designs, combining with (4.44), the electrical power is related to the maximum torque according to

$$W_e \approx \frac{2\pi\rho}{S} \cdot \left(\frac{3}{4\pi} \cdot \frac{T_\tau}{\tau_y}\right)^{1/3} (H_{MR} \cdot 2g)^2 \tag{4.55}$$

4.5 Multiple disks brake

In order to increase the compactness of the disk design, several rotors disks can be used instead of one, with a disk attached to the stator located in between each rotor disk. Such design, already proposed in (Rabinow, 1951) is very popular and used in a wide number of applications requiring very high torque in a limited space and weight. This configuration is used for a prosthetic knee (delivering an output torque of about 50Nm) manufactured by OSSUR Inc. (Deffenbaugh et al., 2001) (Gudmundsson et al., 2007), or as part of an ankle-foot orthosis (Furusho et al., 2007). Other applications requiring high torques are in the automotive field with clutches for automatic transmission (Gopalswamy and Jones, 1998) or for limited slip differential applications (Kavlicoglu et al., 2006).

The equations describing this particular design being very similar to those of the single disk brake, only the final expressions will be described in this section.

If N_d is the number of disks linked to the rotor (and $2gN_d$ the total MR-fluid gap), the torque induced by the magnetic field and the viscous torque are given by:

$$T_\tau \approx \frac{4}{3}\pi\tau_y R_d^3 N_d \tag{4.56}$$

$$T_\eta \approx \pi\eta\frac{\dot{\theta}}{g}R_r^4 N_d \tag{4.57}$$

As compared with the single disk design, if the dimensions are unchanged, the output torque is multiplied by the number of disks attached to the rotor without affecting the dynamic range.

Indeed, combining Eq.(4.56) and (4.57), one gets the dynamic range:

$$\frac{T_\tau}{T_\eta} = \frac{4}{3}\,\frac{\tau_y}{\eta}\cdot\frac{1}{R_r}\cdot\frac{g}{\dot{\theta}} \tag{4.58}$$

Equation (4.56) provides the relationship between the maximum braking torque and the radius of the brake

$$R_r = \left(\frac{3}{4\pi}\cdot\frac{1}{N_d}\cdot\frac{T_\tau}{\tau_y}\right)^{1/3} \tag{4.59}$$

showing that the rotor radius decreases with the number of disks.

As for the single disk design, the brake has the shape of a cylinder of approximate radius $R_{ext} = R_r + h$. Its height is equal to $2h + h_{coil}$, where h_{coil} is the coil height. The volume is

$$V \approx \pi R_{ext}^2.(2h + h_{coil}) = \pi R_r^2\left(1+\frac{\alpha}{2}\right)^2(\alpha R_r + h_{coil}) \tag{4.60}$$

For $\alpha = 1/2$, this leads to

$$V \approx \frac{3}{2}\pi R_r^2\left(\frac{R_r}{2} + h_{coil}\right) \tag{4.61}$$

Combining (4.56) and (4.61), the torque to volume ratio is

$$\frac{T_\tau}{V} \approx \frac{8}{9} \cdot \frac{R_r}{(R_r/2) + h_{coil}} \cdot N_d \cdot \tau_y \tag{4.62}$$

If h_{coil} is neglected, as done for all previous designs, one gets

$$\frac{T_\tau}{V} \approx \frac{16}{9} \cdot N_d \cdot \tau_y \tag{4.63}$$

As before, the magnetomotive force, NI, results from Ampere's law. The integral is dominated by the contribution of the fluid gap:

$$NI \approx H_{MR}.2g.N_d \tag{4.64}$$

NI is thus N_d times larger than for the previous designs. If the current I is the same for all designs, this means that the number of turns N has to be N_d times larger, drastically increasing the coil dimensions. Neglecting h_{coil} in Eq.(4.62) is thus not correct for high N_d values and especially when the gap thickness is large. Figure 4.5 shows the evolution of the torque/volume ratio of multiple disks brakes as a function of the number of rotor disks N_d, when h_{coil} is *not* neglected. It can be seen that, above a given number of disks (depending on the gap thickness), the torque/volume ratio reaches a plateau value and does not increase any more with the number of disks. Such behavior can not be seen from Eq.(4.63) where h_{coil} is neglected.

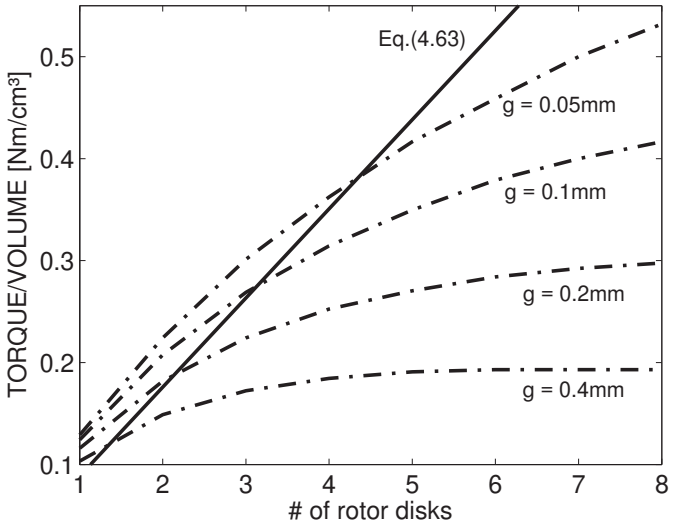

Figure 4.5: Multiple disks brake: results of Finite Element analysis

From similar developments than those made for the drum designs, the electrical power dissipated in the disk brake is given by

$$W_e = \frac{2\pi\rho R_r}{S} \cdot (H_{MR} \cdot 2g \cdot N_d)^2 = CR_r \cdot (H_{MR} \cdot 2g \cdot N_d)^2 \tag{4.65}$$

where $C = 2\pi\rho/S$. As for the drum designs, combining with (4.59), the electrical power is related to the maximum torque according to

$$W_e \approx \frac{2\pi\rho}{S} \cdot \left(\frac{3}{4\pi} \cdot \frac{1}{N_d} \cdot \frac{T_\tau}{\tau_y} \right)^{1/3} (H_{MR} \cdot 2g)^2 \tag{4.66}$$

4.6 Validation via Finite Element analysis

The simplified analytical models, described in the previous sections, have all been validated by comparison with a finite element analysis of the flux density within the magnetic circuit, conducted with FEMM, an open-source Finite Element software solving low frequency electromagnetic problems on 2D planar and axisymetric domains (for more details see: http://www.femm.info). The numerical results show that the flux density is nearly constant throughout the flux gap, and equal to the value required to achieve the maximum yield stress. An illustration of these results is shown at Figure 4.6, for the single disk brake. Results for the T-shaped rotor brake used in this work are shown in chapter 7.

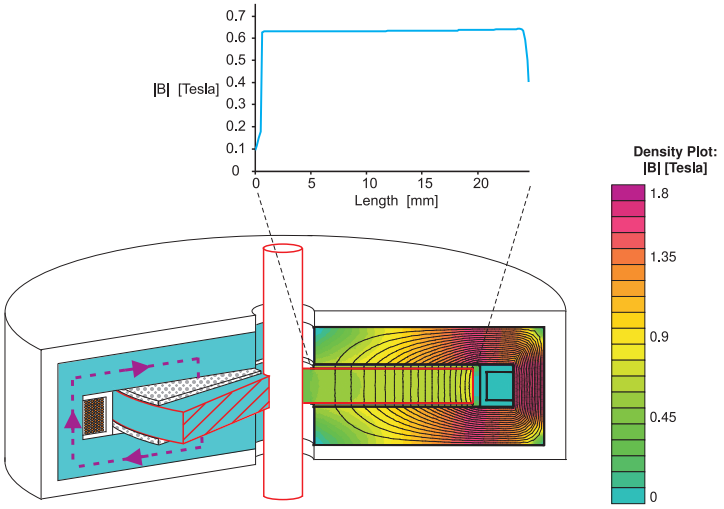

Figure 4.6: Disk brake: results of Finite Element analysis (obtained with FEMM)

4.7 Comparison of performances

The analytical formulas obtained in the previous sections are summarized in Table 4.1. Note that the dynamic range is characterized by similar expressions for all designs, but it is inversely proportional to the rotor radius that, for a given torque T_τ, highly differs for the various brake designs. The torque to volume ratio is only dependent on the MR-fluid shear stress τ_y (and the number of rotor disks N_d for the multiple disks design). Finally, it is interesting to note that for all designs, the electric power consumption grows with the square of the total gap. Decreasing the gap will limit the power consumption but will also reduce the dynamic range and increase mechanical complexity, driving manufacturing costs.

	Rotor radius (R_r)	T/V ratio	Dynamic Range	Power
Drum and inverted drum	$\left(\frac{1}{4\pi}\cdot\frac{T_\tau}{\tau_y}\right)^{1/3}$	$\frac{8}{9}\tau_y$	$\frac{\tau_y}{\eta\dot{\theta}}\cdot\frac{g}{R_r}$	$CR_r\left(H_{MR}\cdot 2g\right)^2$
Disk	$\left(\frac{3}{4\pi}\cdot\frac{T_\tau}{\tau_y}\right)^{1/3}$	$\frac{16}{9}\tau_y$	$\frac{4}{3}\cdot\frac{\tau_y}{\eta\dot{\theta}}\cdot\frac{g}{R_r}$	$CR_r\left(H_{MR}\cdot 2g\right)^2$
Multiple disks	$\left(\frac{3}{4\pi}\cdot\frac{1}{N_d}\cdot\frac{T_\tau}{\tau_y}\right)^{1/3}$	$\frac{16}{9}\tau_y N_d$	$\frac{4}{3}\cdot\frac{\tau_y}{\eta\dot{\theta}}\cdot\frac{g}{R_r}$	$CR_r\left(H_{MR}\cdot 2g\cdot N_d\right)^2$
T-shaped	$\left(\frac{1}{8\pi}\cdot\frac{T_\tau}{\tau_y}\right)^{1/3}$	$\frac{11}{9}\tau_y$	$\frac{\tau_y}{\eta\dot{\theta}}\cdot\frac{g}{R_r}$	$4CR_r\left(H_{MR}\cdot 2g\right)^2$

Table 4.1: Characteristics of the various MR-brake designs ($\alpha = 1/2$) - N_d corresponds to the number of rotor disks

From the expressions of Table 4.1, a classification of the various designs can be made. It is summarized at Table 4.2. These results have been obtained considering $N_d > 4$ in the multiple disks design. It can be concluded that the multiple disks brake performs best in terms of compactness (torque/volume ratio, rotor radius) and of dynamic range but at the expense of a much higher power consumption. The T-shaped rotor design offers a good alternative, being a little bit less compact (lower torque/volume ratio) but requiring less power and being easier to manufacture. The three other designs are globally less compact than the T-shaped rotor design, making it a good compromise for the application considered in this thesis.

	Drum	Disk	Inverted drum	T-shaped	Multiple-disks
Rotor radius	-	- -	-	+	++
Torque/volume	- -	+	- -	-	++
Dynamic range	-	- -	-	+	++
Power	++	+	++	+	- -
Mechanical simplicity	++	++	-	-	- -

Table 4.2: Comparison of the various MR-brake designs

The approximate formulae presented at Table 4.1 have been compared to results obtained with magnetic Finite Element (FE) models based on brake dimensions resulting from exact relationships. These results have been obtained for a MR-fluid gap of 0.4mm for all designs and 4 rotor disks for the multiple disks design. As can be observed on Figure 4.7a), the approximate formulae provide a good estimation of the rotor radius (R_r) except for the T-shaped rotor design where R_r is underestimated due to the approximation made at Eq. 4.26. Torque/Volume values are overestimated for small output torques, for all designs (Figure 4.7b). Indeed, small

output torque requirements lead to small brake dimensions where the coil volume cannot be neglected. At higher output torques, only the multiple disk design exhibits bad correspondence due to a very large coil that was neglected in the approximate formula. As can be observed, a smaller gap value, leading to smaller coil dimensions (for a given current), leads to a better agreement with FE results.

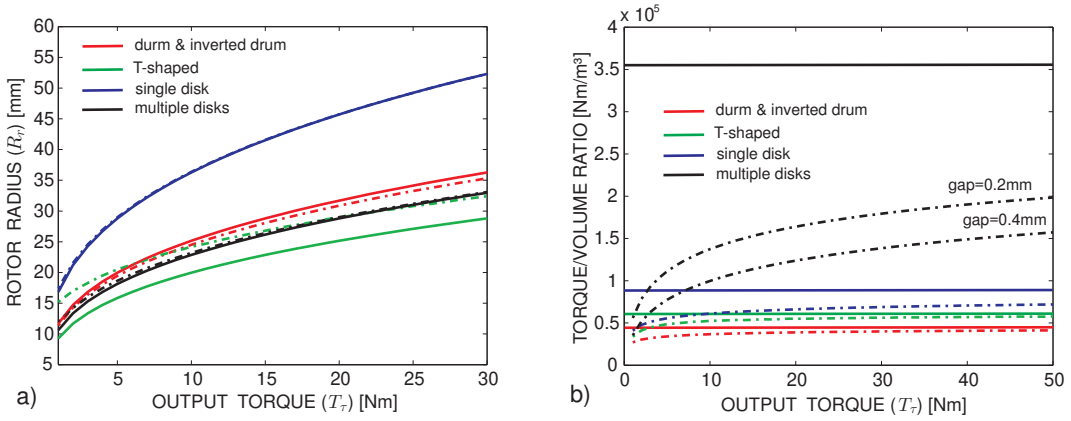

Figure 4.7: a) Rotor radius - b) Torque/Volume ratio as a function of output torque (plain lines correspond to approximate formulae and dashed lines to FE results)

Curves obtained with the approximate formulae for the Dynamic Range are in good agreement with FE results except for the T-shaped brake at low torques (Figure 4.8a). This can be explained by the underestimated rotor radius (the relative difference in rotor radius being higher at low torques). Figure 4.8b) compares the results obtained for the power consumption, considering the same coil section (S) for all designs (the current is adapted to fit the various architectures). It can be observed that the approximate formulae underestimate the power requirements for all designs (indeed the rotor radius R_r was considered instead of the coil radius to compute the electrical resistance of the coil). However, for all figures of merit, the relative performances of all designs is respected.

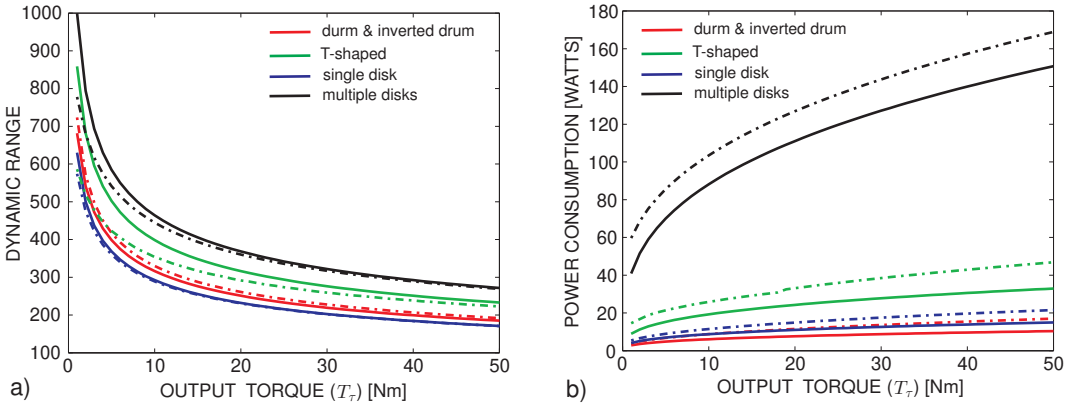

Figure 4.8: a) Dynamic Range - b) Power consumption as function of output torque (plain lines correspond to approximate formulae and dashed lines to FE results)

4.8 References

B. Ackermann and R. Elferich. Application of magnetorheological fluids in programmable haptic knobs. In *Proceedings of Actuator 2000*, Bremen, Gremany, 2000.

J. An and D-G. Kwon. Modeling of a magnetorheological actuator including magnetic hysteresis. *Journal of Intelligent Material Systems and Structures*, 14:541–550, 2003.

J. An and D-S. Kwon. Haptic experimentation on a hybrid Active/Passive force feedback device. In *Proceedings of the IEEE International Conference on Robotics and Automation*, pages 4217–4222, Washington DC, 2002.

R. Bölter and H. Janocha. Design rules for MR-fluid actuators in different working modes. In *Proccedings of SPIE Smart Structures and Materials 1997*, pages 148–159, San Diego, California, 1997.

J.D. Carlson. Magnetorheological brake with integrated flywheel. US patent 6,186,290, 2001.

J.D. Carlson, D.F. LeRoy, J.C. Holzheimer, D.R. Prindle, and R.H. Marjoram. Controllable brake. US patent 5,842,547, 1998.

B.W. Deffenbaugh, H.M. Herr G.A. Pratt, and M.B. Wittig. Electronically controlled prosthetic knee. US patent application 2001/0029400, 2001.

V. Dwivedi, G.V. Strikis, J.M. Ginder, L.D. Ellie, S.A. Harte, and K. Bhatia. Magnetic powder clutch. US patent 6,394,244, 2002.

J. Furusho, T. Kikuchi, M. Tokuda, T. Kakehashi, K. Ikeda, S. Morimoto, Y. Hashimoto, H. Tomiyama, A. Nakagawa, and Y. Akazawa. Development of a shear type compact MR brake for the intelligent ankle-foot orthosis and its control. In *Proceedings of the 2007 IEE 10th International Conference on Rehabilitation and Robotics*, pages 89–94, Noordwijk, The Netherlands, 2007.

S. Gopalswamy and G.L. Jones. Magnetorheological transmission clutch. US patent 5,823,309, 1998.

K.H. Gudmundsson, F. Jonsdottir, H. Palsson, and S.G. Karlsson. Optimization a magnetorheological rotary brake. In *Proceedings of 3rd ECCOMAS Thematic Conference on Smart Structures and Materials*, Gdansk, Poland, 2007.

J. Huang, J.Q. Zhang, Y. Yang, and Y.Q. Wei. Analysis and design of a cylindrical magnetorheological fluid brake. *Journal of Materials Processing Technology*, 129:559–562, 2002.

M.R. Jolly, R.H. Majoram, S. Koester, and K.A. St Clair. Brake with field responsive material. US patent 6,854,573, 2005.

B. Kavlicoglu, F. Gordaninejad, C. Evrensel, A. FUchs, and G. Korol. A semi-active, high torque, magnetorheological fluid limited slip differential clutch. *Journal of Vibration and Acoustics*, 128:604–610, 2006.

D. Lampe and R. Grundmann. Transitional and solid state behaviour of a magnetorheological clutch. In *Proceedings of Actuator 2000*, 2000.

W.H. Li and H. Du. Design and experimental evaluation of a magnetorheological brake. *International Journal of Advanced Manufacturing Technology*, 21:508–515, 2003.

LORD. *Engineering Note - Designing with MR-Fluids*. LORD, 1998.

N. Lucchesi. *Analisi e Progettazione Di un Nuovo Sistema Dattuazione Per Interfacce Aptiche a Più Gradi Di Libertà*. PhD thesis, Universita Degli Studi di Pisa, 2004.

Y-J. Nam, Y-J. Moon, and M-K Park. Performance improvement of a rotary MR fluid actuator based on electromagnetic design. *Journal of Intelligent Material Systems and Structures*, 00:1–11, 2007.

J. Rabinow. Magnetic fluid torque and force transmitting device. US patent 2,575,360, 1951.

B. Sapinski and S. Bydon. Application of magnetorheological fluid brake to shaft position control in induction motor. In *AMAS Workshop on Smart Materials and Structures*, pages 169–180, Jadwisin, 2003.

A.L. Smith, J.C. Ulicny, and L.C. Kennedy. Magnetorheological fluid fan drive for trucks. *Journal of Intelligent Material Systems and Structures*, 18:1131–1136, 2007.

N. Takesue, J. Furusho, and Y. Kiyota. Analytic and experimental study on fast response MR-fluid actuator. In *Proceedings of the IEEE Int. Conf. On Robotics and Automation 2003*, pages 202–207, Tapei, Taiwan, 2003.

H. Wang, X.L. Gong, Y.S. Zhu, and P.Q. Zhang. A route to design rotary magnetorheological dampers. In *Proceedings of the Ninth International Conference on Electrorheological Fluids and Magnetorheological Suspensions*, pages 680–686, Beijing, China, 2004.

K.S. Wong and W.H. Liao. Adaptive body fitness equipment using magnetorheological fluids. In *Proceedings of the IEEE International Conference on Robotics and Biomimetics*, pages 432–437, 2005.

T.M. York, C.D. Gilmore, and T.G. Libertiny. Magnetorheological fluid coupling device and torque load simulator system. US patent 5,598,908, 1997.

Chapter 5

Early prototypes and test bench

5.1 Design of the prototypes

Early MR-brake prototypes have been developed within the exploratory phase of the design of a portable haptic exoskeleton devoted to robot teleoperation. In this context various actuation technologies were analyzed and compared with respect to parameters such as dynamic range, torque/volume ratio, torque rise time... (Avraam et al., 2005) (Letier et al., 2006). MR-brakes were considered in the frame of this study due to their compactness, absence of backlash and smooth operation. They were finally not considered for the final design at the benefit of DC motors coupled with a cable reducer providing better haptic rendering (Letier et al., 2008).

5.1.1 Prototype 1 - Drum brake

A first MR-brake prototype was build in order to validate the design process (described in chapter 4) and to identify possible manufacturing difficulties and challenges. The drum brake design (see section 4.2) was selected for this first prototype thanks to its inherent simplicity and radial compactness. This brake was designed to deliver an output torque of 1Nm and the MR-fluid gap was fixed at 0.4mm, a value easily achievable with common manufacturing processes.

Since one of the objectives of this first prototype was to achieve a compact and light design, we selected, among the fluids available to us, the MR-fluid exhibiting the highest yield stress value combined with the lowest induction (Figure 2.7b): AL458 developed by Fraunhofer ISC.

The material selected for the magnetic core is soft iron. Due to their higher saturation values (Figure 3.3), iron-cobalt alloys would have led to a more compact and lighter design but these materials are more expensive and difficult to obtain in small quantities. If power consumption is critical, silicon-iron alloys are preferred for their higher permeability. Dimensions of this first prototype are given at Figure 5.1a).

A schematic cross-section of the prototype is shown at Figure 5.1b). Two ball bearings with integrated seals (SKF 626-RSH) have been used to support the rotor and avoid MR-fluid leaks. A filling pipe connected to a lateral channel is located within the brake output axis in

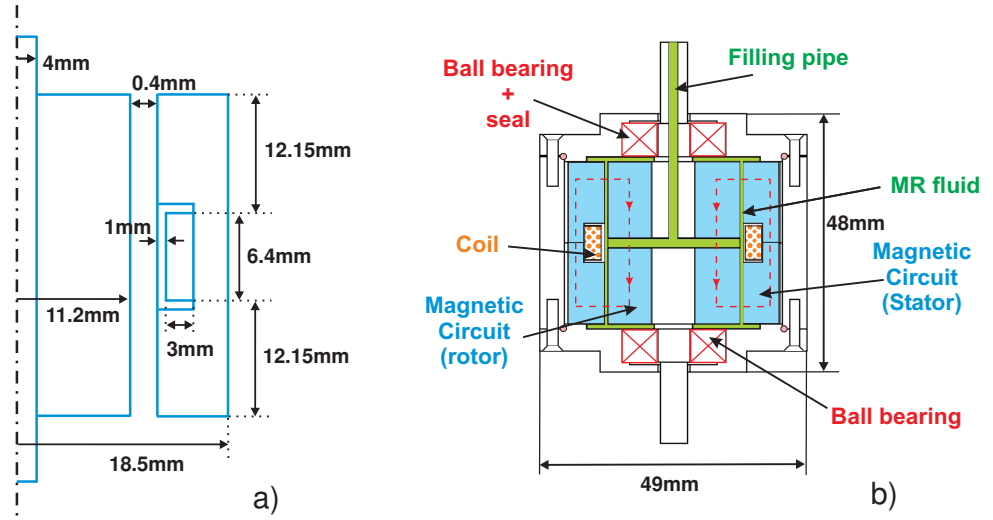

Figure 5.1: Drum brake prototype: a) magnetic core dimensions - b) schematic cross-section

order to ensure proper filling of the gap. The brake axis is made of brass in order to achieve a high enough torsional strength and avoid magnetic flux leakage. The rotor is glued to the output axis. This brake was designed to be easily disassembled. The stator is composed of two parts, surrounding the coil winded on an aluminum support. The outer aluminum casing is composed of a central cylinder and two covers equipped with rubber o-rings to seal the MR-fluid cavity. Figure 5.2 shows a picture of the different parts of the prototype.

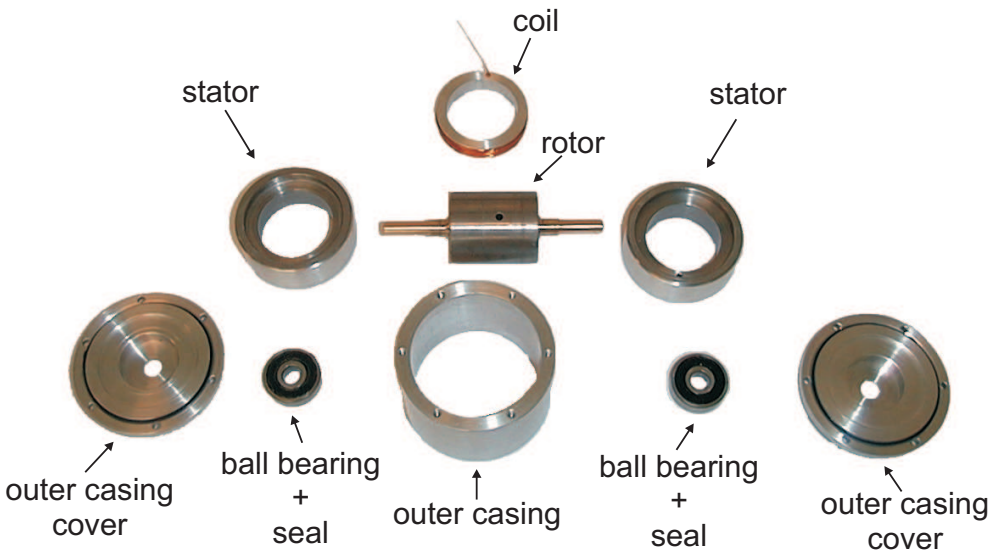

Figure 5.2: Drum brake prototype: exploded view

5.1.2 Prototype 2 - T-shaped rotor brake

The objective of the second prototype was to validate the increased compactness of the T-shaped rotor design as compared to the drum design. An even higher compactness may have been achieved with the multiple disks design but this design was not considered due to a much higher mechanical complexity. The desired output torque was set to 2Nm and the MR-fluid gap was fixed at the same value as before (0.4mm). The MR-fluid and magnetic core material selected for this prototype were the same as for the previous one. Dimensions of this prototype are given at Figure 5.3a).

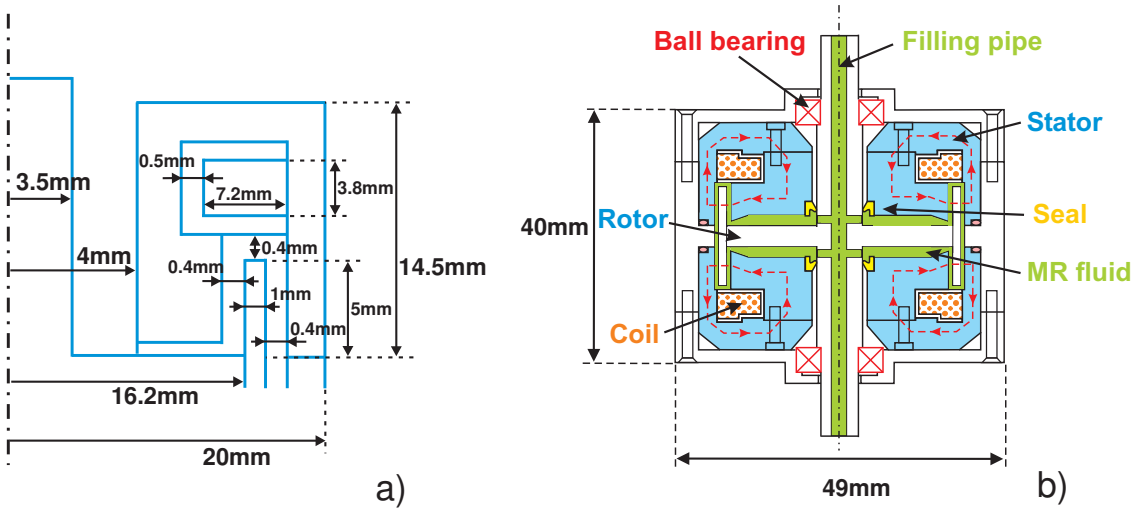

Figure 5.3: T-shaped rotor brake prototype: a) magnetic core dimensions - b) schematic cross-section

A schematic cross-section of the prototype is shown at Figure 5.3b). For this prototype, seals independent of ball bearings have been used in order to limit the volume of the MR-fluid cavity. Two filling pipes are located within the output axis. A single non-magnetic stainless steel part is used for the output axis and the hub to avoid flux leakage. The useful T-shaped section of the rotor is composed of a cylindrical soft iron part glued and screwed to the central part.

Two toroid coils have been used, winded on a plastic support to avoid eddy currents during operation, limiting the response time of the brake (see section 5.3.4). These coils are surrounded by a soft iron magnetic core exhibiting an optimized geometry to achieve a nearly uniform induction distribution, reducing the weight of the brake. Here again, the outer aluminum casing is composed of a central cylindrical part and two covers. Figure 5.4 shows a picture of the different parts of the second prototype.

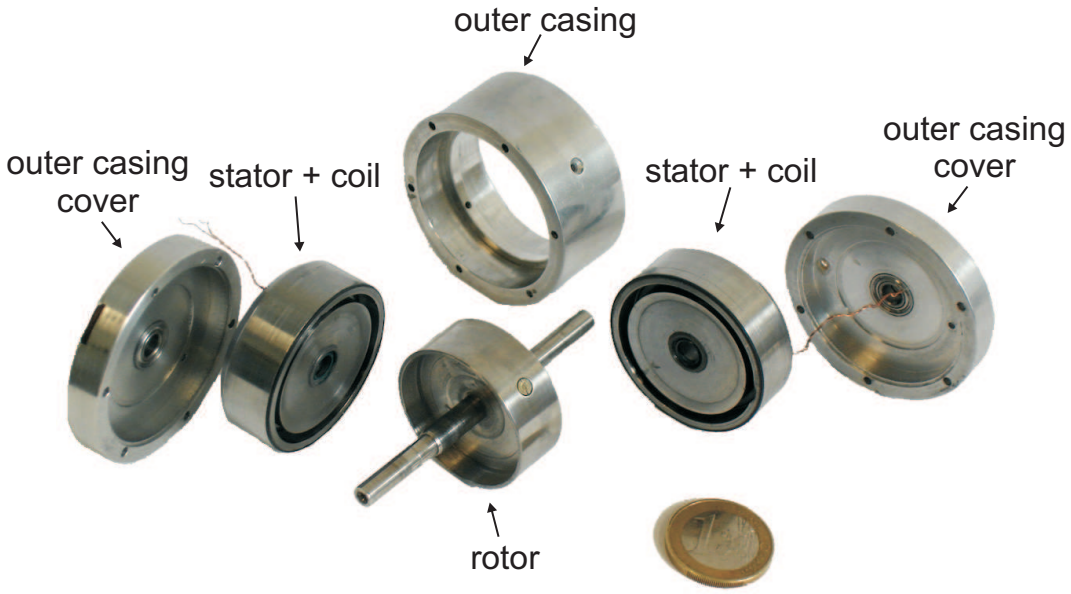

Figure 5.4: T-shaped rotor brake prototype: exploded view

5.2 Design of the test bench

In order to measure the properties of the MR-brake prototypes and test control algorithms, a test bench has been developed. It is similar to what can be found in the literature (An and Kwon, 2003) (Takesue et al., 2003) (Nam et al., 2007) (Böse et al., 2006); it consists of a DC motor coupled with a planetary reducer having its output axis connected to the MR-brake on one side and mounted on a flexible support equipped as a torque sensor (Figure 5.5).

The DC-motor, which can be either torque or speed controlled, is used as a driving source to apply various torque or speed patterns on the MR-brake. The encoder on the DC-motor side is used to control the motor motion and the one on the MR-brake side is used to control the MR-brake torque. Control of both DC-motor and MR-brake, driven through external current amplifiers, is implemented on a PC equipped with MATLAB simulink, the PC being interfaced with the setup through a dSpace control board.

A reaction torque sensor, manufactured in-house, is used to indirectly measure the torque applied by the brake by measuring the reaction torque applied on the stator of the DC-motor. This sensor converts the rotational motion of the stator of the DC-motor into flexion of its flexible ribs (Figure 5.6), measured with strain gages properly placed. To select their location, a Finite Element model of the sensor has been realized (Figure 5.7a).

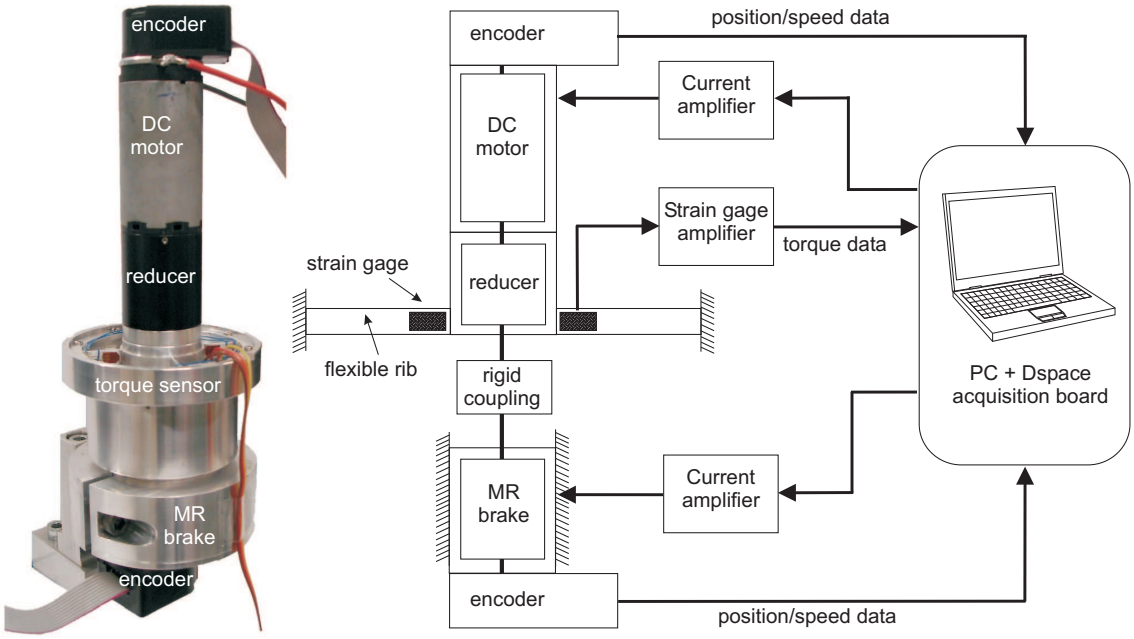

Figure 5.5: Test bench for prototype evaluation

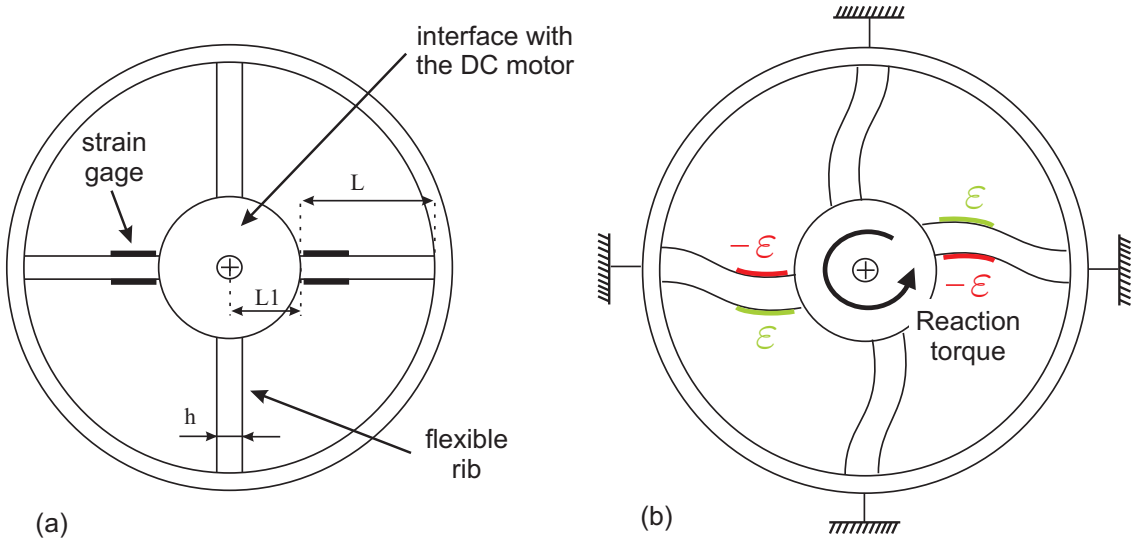

Figure 5.6: Schematic view of the torque sensor with: (a) no torque applied - (b) applied reaction torque

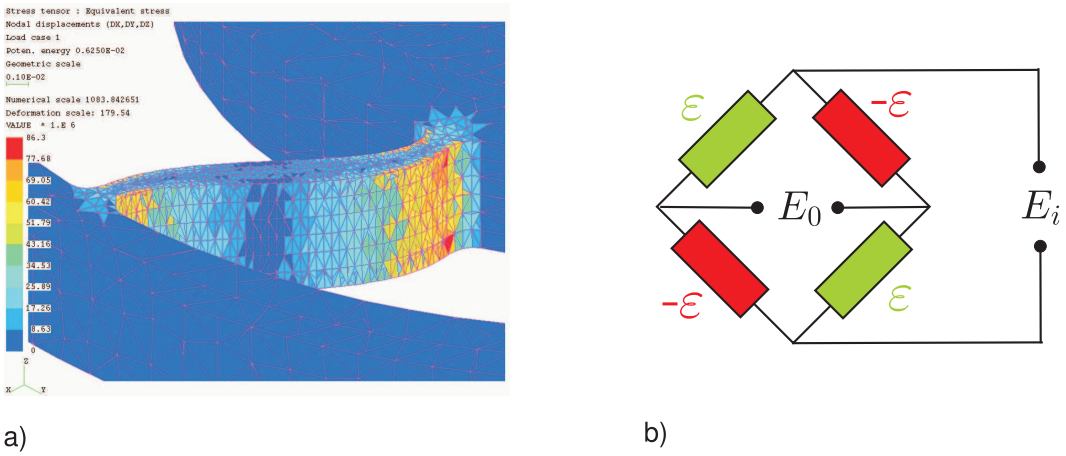

Figure 5.7: a) Rib strain obtained by FE analysis - b) Strain gages in full Wheatstone bridge arrangement

The sensor is designed to be as sensitive as possible. This means that for a given maximum torque and a given rib length, the rib thickness (h) should be selected as small as possible and in such a way that the maximum stress is significantly lower than the lamella material yield stress ($h = 1.25$mm, $L = 15$mm, $L_1 = 17$mm).

Four strain gages, with an electrical resistance of 350Ω (from HBM: 3/350LG13), are used and connected to form a full-Wheatstone bridge (Figure 5.7b). It leads to a sensitivity twice higher than what can be obtained with only two strain gages (half-bridge) while being thermally stable. The relation between the ratio of the input (E_i) and output (E_o) voltages and the measured strain is given by Eq. 5.1:

$$\frac{E_o}{E_i} = G\varepsilon \tag{5.1}$$

where G is the gage factor (intrinsic gage property, depending on gage material and temperature).

5.3 Experimental properties identification

5.3.1 Introduction

The objective of this section is to experimentally characterize the properties of the two brake prototypes described in section 5.1. Furthermore, for the second prototype, the same tests have been performed with two fluids exhibiting high yield stress (ISC AL458 and LORD MRF140), in order to outline the possible impact of fluid selection on device performances.

5.3.2 Torque/current characteristic

In order to obtain this curve, the motor is set to a constant rotational velocity (360°/s) while the brake is supplied with a control current varying continuously from 0A to a maximum value and then returning back to 0A (Figure 5.8). In order to avoid coil overheating and due to the small coil wire section (diameter=0.2mm), the current inside each coil was limited to about 0.55A.

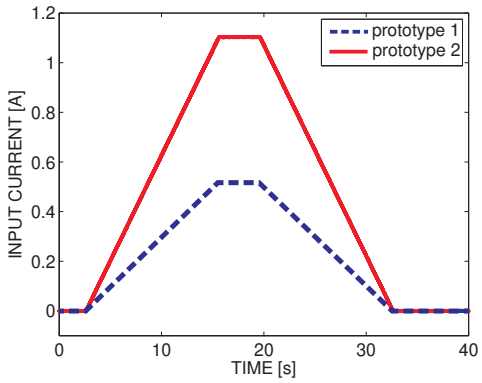

Figure 5.8: Input current applied to the MR-brake prototypes

Figure 5.9 shows the curves obtained, according to this procedure, for the two prototypes and the two selected MR-fluids. As expected (section 5.1), the maximum torque obtained with the second prototype is about twice as large as the one obtained with the first prototype. Furthermore, the maximum output torque is larger with the AL-458 than with the MRF140. This can be explained by the fact that the second prototype was initially designed to be used in combination with the AL458. When it is used with the MRF140, due to a higher fluid permeability (Figure 2.7b), section 3.1.2), saturation in the soft-steel appears for a lower current value, limiting the maximum output torque (if NI remains unchanged, H_{MR} is unchanged but B_{MR} and thus B_{iron} are increased).

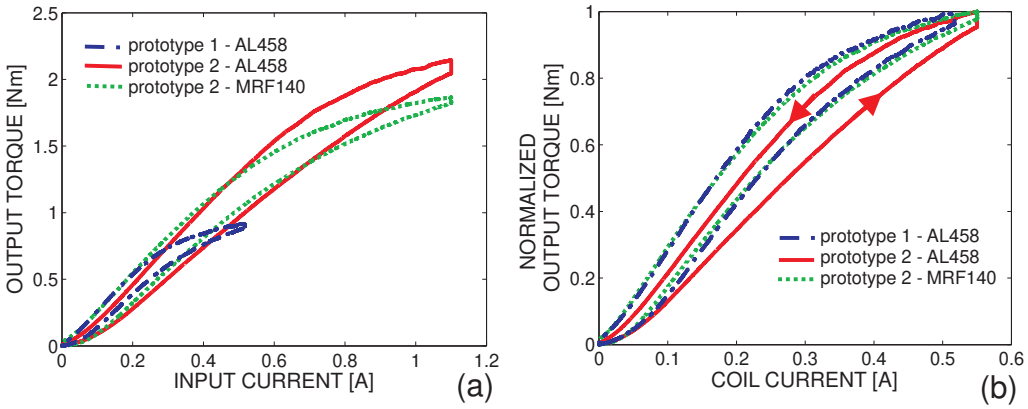

Figure 5.9: Torque/current curves for the various MR-brake prototypes: (a) nominal - (b) normalized to its maximum value

The torque/current curve is non-linear, because the relationship between the yield stress (τ_y) and the magnetic field (H) is non-linear (Figure 2.7b), section 3.1.2) and also, for high current values, because of saturation in the soft-steel core which is also responsible of the hysteresis (Sapinski and Bydon, 2003). Such an hysteretic behavior is well known in the MR-brakes literature (Takesue et al., 2003)(An and Kwon, 2003)(Nam et al., 2007) and MR-dampers (Dong et al., 2005). In order to better understand this hysteretic behavior, various triangular current patterns were applied to the second brake prototype (Figure 5.10).

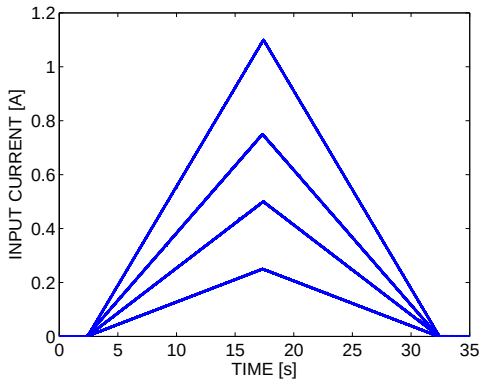

Figure 5.10: Triangular-shaped input current applied to the second MR-brake prototype

As a result, for both MR-fluids, sub-hysteresis cycles were observed, all of them being included in the largest one obtained for the maximum input current (Figure 5.11). Such behavior was already observed in (Sapinski and Bydon, 2003) and in (Liu et al., 2006). Figure 5.11 also shows the torque/current curve resulting from Finite Elements simulation (no hysteresis modelling). The disparities with the experimental curves might be explained by disparities between real and modelled material properties.

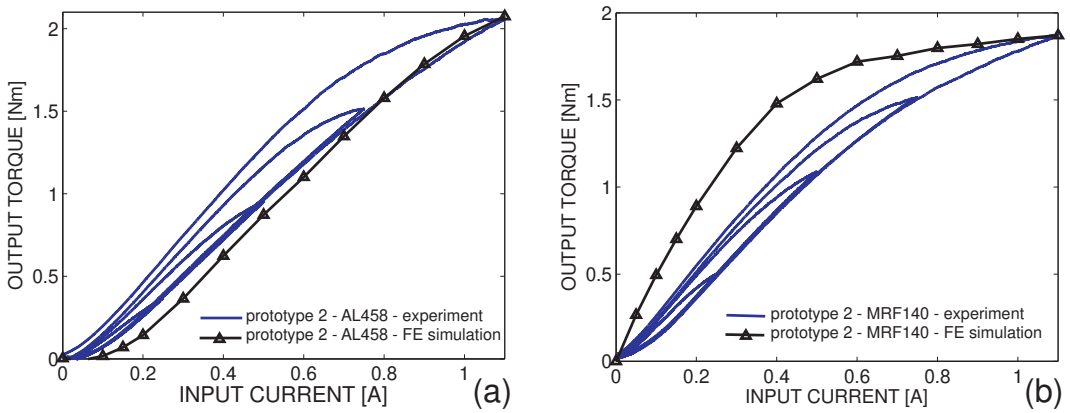

Figure 5.11: Torque/current curve for the second MR-brake prototypes filled with (a) ISC AL458 (b) LORD MRF140

5.3.3 Torque/speed characteristic

The objective of this sub-section is to investigate the possible dependency between the output torque of the brake and its rotational speed. For this purpose, a continuously increasing speed ramp was imposed on the motor of the test bench (going from 0°/s to 400°/s) while different constant current commands were applied to the second brake prototype.

Before discussing experimental results, it is interesting to see how the torque/speed behavior of the brake can be analytically predicted. The Bingham model gives:

$$\tau = \tau_y(B) + \eta\left(\dot{\gamma}\right)\dot{\gamma} \tag{5.2}$$

where $\dot{\gamma}$ is the shear rate. If we assume a linear speed profile between the stator and rotor of the brake and if we consider only the contribution of the fluid located in the active fluid area, Eq. 5.2 becomes:

$$\tau = \tau_y(B) + \eta\left(\dot{\gamma}\right)\frac{r\dot{\theta}}{g} \tag{5.3}$$

where r is either the inner- or outer- rotor radius and g is the MR-fluid gap. Furthermore, it is important to note that, due to anti-settling additives, the off-state viscosity (η) is highly dependent on the shear rate up to a certain shear rate value (Figure 5.12(a), for the AL458). This leads to a highly non-linear shear stress/shear rate relationship, at low shear rates (Figure 5.12(b) obtained with a rotational rheometer for the AL458 and MRF140). For higher shear rates, the relation is considered as linear.

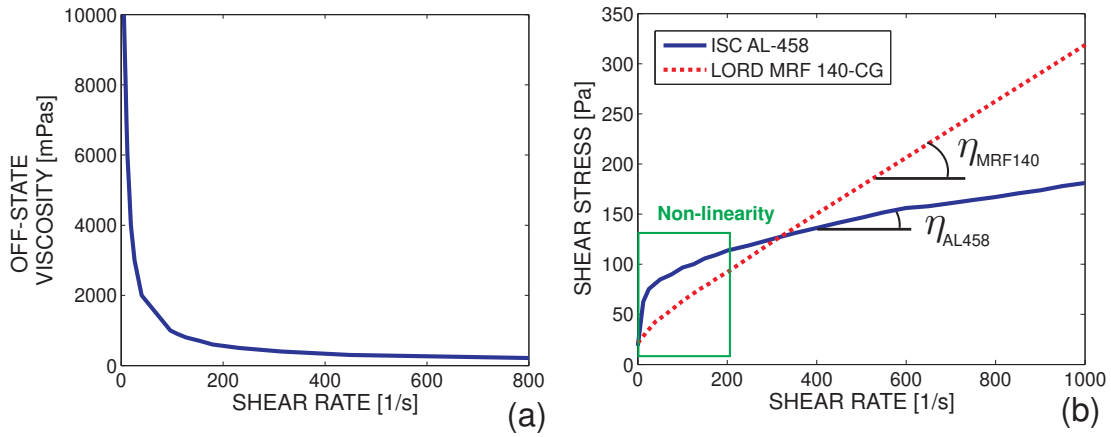

Figure 5.12: (a) Off-state viscosity (η) of the AL458 (b) Off-state shear stress ($\eta\frac{r\dot{\theta}}{g}$) as a function of shear rate ($\frac{r\dot{\theta}}{g}$) for the AL458 and MRF140 (adapted from manufacturer datasheets) (for this application, typical shear rate values are about 200/s)

Knowing the relation between the off-state shear stress and the shear rate, and referring to Eq. 5.3, we can calculate the off-state torque of the device as a function of angular speed for various values of the MR-fluid gap (Figure 5.13). Curves in Figure 5.13 have been shifted by a value corresponding to the static friction inside the brake (measured experimentally). The off-state friction is increasing when the MR-fluid gap is decreasing. However it should

be noticed that, even for very small gaps, the slope of the curve remains small, corresponding to a very small dependency between the off-state torque and the angular speed of the brake. Thus, at the rotational speeds considered here, the off-state torque is dominated by the seal friction. Figure 5.14 shows the experimental results (full lines) obtained with the second brake prototype filled with (a) AL458 and (b) MRF140. These results are compared to the analytical predictions, based on the Bingham model (dashed lines) relying on the experimental Torque/Current characteristic to predict the field-induced torque. The output torque is nearly independent of the angular speeds (except for very small angular speeds). This behavior is similar to what was observed in previous studies (Takesue et al., 2003) (Ye and Williams, 2006) (Nam et al., 2007).

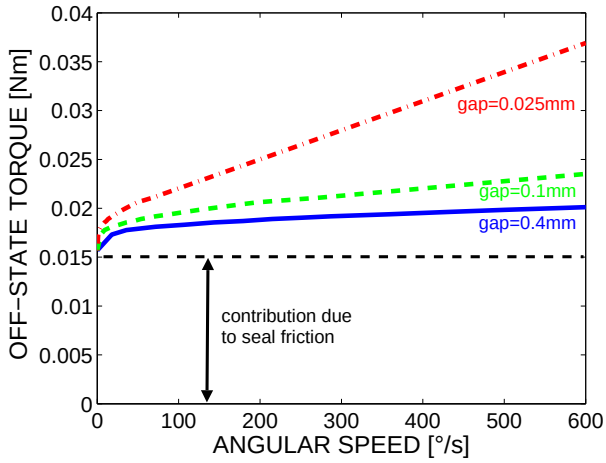

Figure 5.13: Analytical estimation of the off-state torque of the second brake prototype filled with AL458

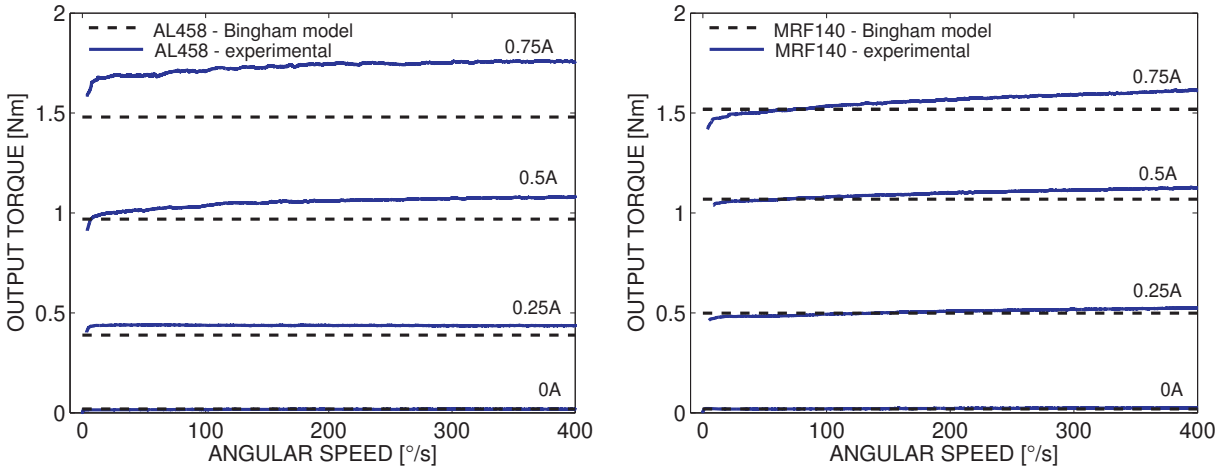

Figure 5.14: Experimental and simulated torque/speed curves for the second brake prototype filled with AL458 and MRF140 for various input currents (experimental curves and Bingham model)(speed sweep duration: 20s)

It is also interesting to note that the deviation between experimental results and analytical predictions is much higher for the AL458 than for the MRF140. For both fluids, this deviation is increasing for larger currents. Furthermore, the dependency between the output torque and angular speed seems to be higher for higher current values. Such behavior cannot be explained by the Bingham model where the MR-fluid viscosity (η) is independent of the magnetic flux intensity (B) (and thus of the current applied to the brake). There should be another phenomenon explaining this behavior.

For this purpose, an experiment was conducted where, by using the motor of the test bench, a constant angular speed was applied to the brake (200°/s). Successive tests were conducted where various constant current steps were imposed to the brake (Figure 5.15). The evolution of the output torque as a function of time for a duration of 10s was then measured, the brake being filled with both fluids (Figure 5.16).

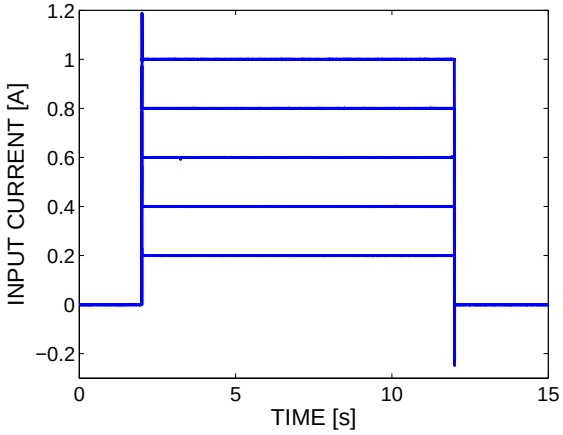

Figure 5.15: Various step input currents applied to the second MR-brake prototype

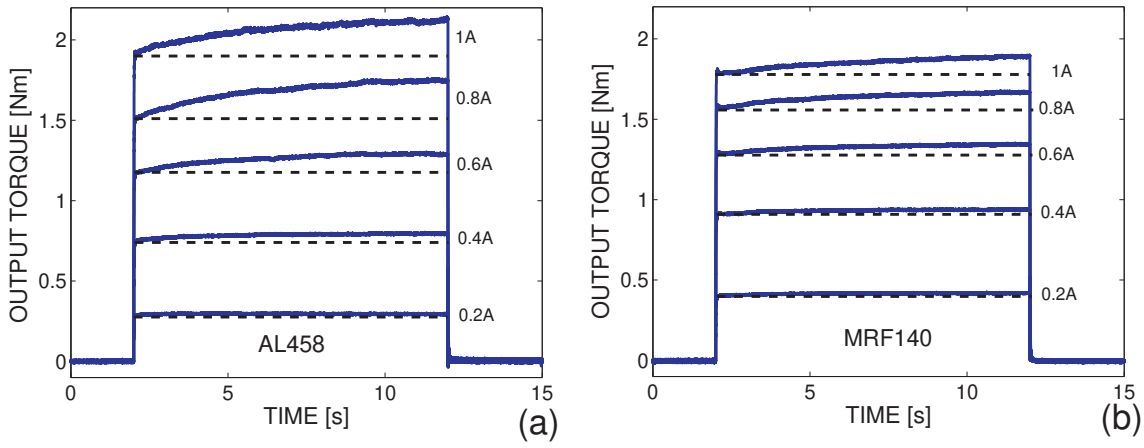

Figure 5.16: Output torque of the second MR-brake prototype, at constant speed (200°/s) and constant input currents, filled with: (a) AL458 - (b) MRF140

Despite the fact that a constant current is imposed to the brake, after a sharp rise, the output torque of the brake slowly increases with time; this phenomenon is more apparent at higher current values. (Laun et al., 2008) observed a similar effect during shear-stress measurements conducted with a commercial rheometer and suggested that it may be due to a slow particle migration inside the MR-fluid, which would appear, here, between the central part of the brake and its periphery. It is also interesting to note that this phenomenon is much more important for the AL458 than for the MRF140, probably due to different fluid compositions.

Based on these results and looking back at Figure 5.14, it can be concluded that what was initially thought as purely being the effect of angular speed on the output torque might be in fact mainly the effect of slow particle migration on the evolution of the output torque with time. It can thus be said that the output torque is nearly not influenced by the angular speed (whatever the current applied to the brake).

5.3.4 Torque response time

The torque response time of the brake is an important parameter since it will influence the dynamic behavior of the device and the control bandwidth. It is important to note that, in general, the torque response time of the device is not controlled by the MR-fluid itself, the inherent MR-fluid response time being much smaller than 1ms (Carlson, 2007). Factors influencing the response time are the magnetic circuit design, the inductance of the coil used to generate the magnetic field and the characteristics of the control electronics.

Indeed, the torque response time is measured by using the motor of the test bench to apply a constant angular speed (200°/s) on the rotor of the brake. At the same time, a current step is applied to the brake. This current step has thus to be as sharp as possible in order to avoid any influence of the current response time on the torque response time of the brake. This is really an issue since the current is flowing through a coil inside the brake in order to generate the required magnetic field. It is thus compulsory to make use of a properly tuned current amplifier to drive the MR-brake (Koo et al., 2006). If not, wrong conclusions might be drawn about the intrinsic behavior of the brake (Choi et al., 1999).

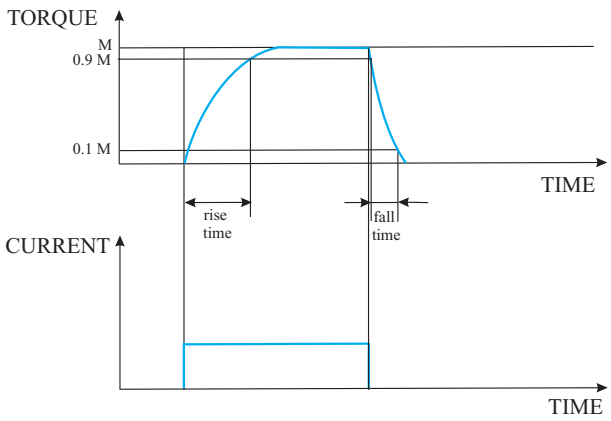

Figure 5.17: Definition of torque rise and fall time

The torque response time has mainly two components (Figure 5.17): the torque rise time, which is defined as the time required for the torque to change from 10% to 90% of its maximum steady state value, and the torque fall time, defined as the time required for the torque to change from 90% to 10% of its maximum steady state value.

Figure 5.18 compares the rise and fall time of the normalized torque on our two prototypes. One sees that the second prototype performs significantly better than the first one. This is due to a small design detail in the support of the coil: in the first prototype, the coil support is made of aluminum and is responsible of strong eddy currents when the current intensity in the coil changes rapidly. These are responsible of the slower change in the output torque. On the contrary, the coil support of the second prototype is made of plastic where eddy currents are prevented (Figure 5.19). Such an effect was already experimentally demonstrated in (Takesue et al., 2003) and validated by Finite Element analysis.

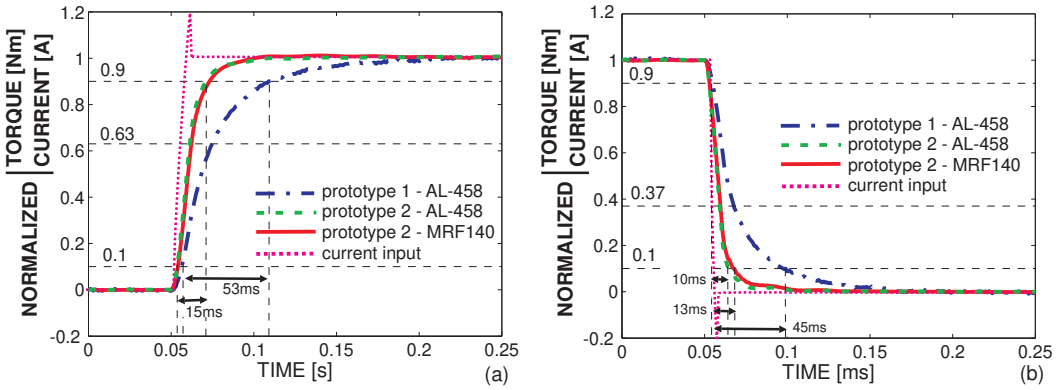

Figure 5.18: Torque rise (a) and fall (b) time for the 1st and 2nd MR-brake prototypes

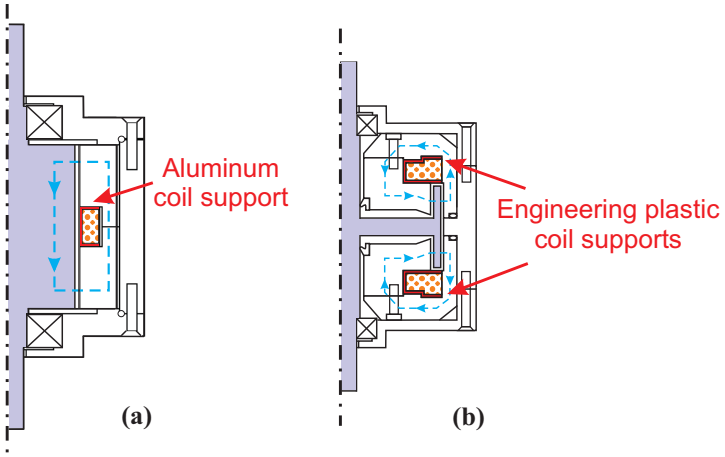

Figure 5.19: Design of 1st (a) and 2nd (b) MR-brake prototype, with emphasis on coil support

It is also important to note that the saturation limit of the current drive (in our setup: 24V) may also affect the torque rise time of the brake by limiting the slope of input current steps. More details are given in (Koo et al., 2006).

5.4 References

J. An and D-G. Kwon. Modeling of a magnetorheological actuator including magnetic hysteresis. *Journal of Intelligent Material Systems and Structures*, 14:541–550, 2003.

M. Avraam, P. Letier, I. Romanescu, M. Horodinca, and A. Preumont. Exoskeleton haptic device for extravehicular space robotic activities: A survey of actuation technology. In *Proceedings of the 15th International Symposium on Measurment and Control in Robotics*, Brussels, Belgium, 2005.

H. Böse, A. Trendler, A. Kramlich, and J. Ehrlich. A haptic knob with different magnetorheological fluids. In *Proceedings of Actuator 2006*, pages 245–248, Bremen, 2006.

J.D. Carlson. Semi-active vibration supression. In *CISM Course: Semi-Active Vibration Suppression - the Best from Active and Passive Technologies*, Udine, October 2007.

S-B Choi, S-R Hong, C-C Cheong, and Y-K Park. Comparison of field-controlled characteristics between ER and MR clutches. *Journal of Intelligent Material Systems and Structures*, 10:615–619, 1999.

S. Dong, K-Q. Lu, J.Q. Sun, and K. Rudolph. Rehabilitation device with variable resistance and intelligent control. *Medical Engineering and Physics*, 27:249–255, 2005.

J-H. Koo, F.D. Goncalves, and M. Ahmadian. A comprehensive analysis of the response time of MR dampers. *Smart Materials and Structures*, 15:351–358, 2006.

H. M. Laun, G. Schmidt, and C. Gabriel. Reliable plate-plate MRF magnetorheometry based on validated radial magnetic flux density profile simulations. *Reologica Acta*, 47(9):1049–1059, 2008.

P. Letier, M. Avraam, M. Horodinca, A. Schiele, and A. Preumont. Survey of actuation technologies for body-grounded exoskeletons. In *Proceedings of Eurohaptics*, Paris, France, 2006.

P. Letier, M. Avraam, S. Veillerette, M. Horodinca, and A. Preumont. SAM : A 7-DOF portable arm exoskeleton with local joint control. In *Proceedings of IEEE IROS 08*, Nice, France, 2008.

B. Liu, W.H. Li, P.B. Kosasih, and X.Z. Zhang. Development of an MR-brake-based haptic device. *Smart Material and Structures*, 15:1960–1966, 2006.

Y-J. Nam, Y-J. Moon, and M-K Park. Performance improvement of a rotary MR fluid actuator based on electromagnetic design. *Journal of Intelligent Material Systems and Structures*, 00:1–11, 2007.

B. Sapinski and S. Bydon. Application of magnetorheological fluid brake to shaft position control in induction motor. In *AMAS Workshop on Smart Materials and Structures*, pages 169–180, Jadwisin, 2003.

N. Takesue, J. Furusho, and Y. Kiyota. Analytic and experimental study on fast response MR-fluid actuator. In *Proceedings of the IEEE Int. Conf. On Robotics and Automation 2003*, pages 202–207, Tapei, Taiwan, 2003.

S. Ye and K. A. Williams. Torsional friction damper optimization. *Journal of Sound and Vibration*, 294:529–546, 2006.

Chapter 6

Methods of muscular evaluation and wrist biomechanics

6.1 Fundamentals of muscle biomechanics and joint function

6.1.1 Concentric and eccentric contraction

The ability of a muscle to produce force throughout the range of motion (ROM) of a joint is called *dynamic* contraction (as opposed to *isometric* contraction, where no joint motion occurs). This force production can be achieved by either muscle shortening or lengthening. If the joint motion is in a direction opposite to the gravitational force and the force produced by the muscle exceeds the external resistance applied to the joint, the muscle is shortening and the contraction is said to be *concentric*. The muscle contraction causes joint motion. If the joint motion is in the direction of the gravitational force and the external resistance applied to the joint exceeds the force produced by the muscle, the muscle is lengthening and the contraction is said to be *eccentric*. The muscle contraction resists to joint motion (Figure 6.1) (Perrin, 1993).

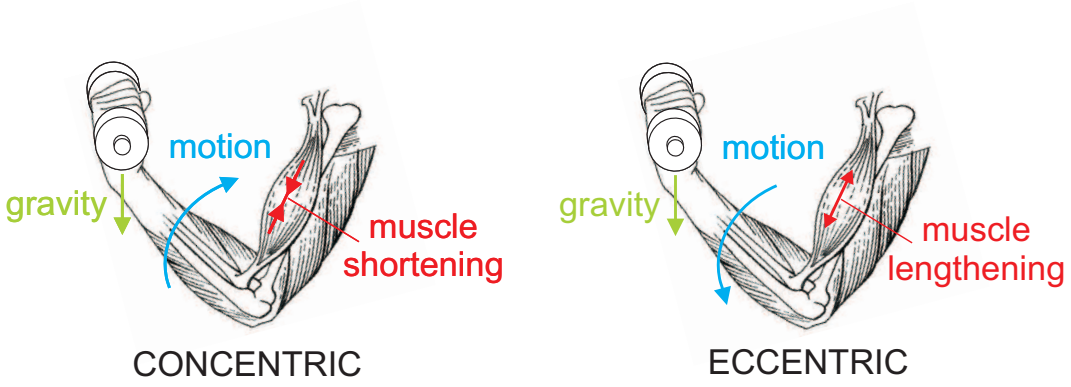

Figure 6.1: Schematic illustration of concentric and eccentric contractions of the biceps

6.1.2 Torque/position and torque/velocity relationships

The ability of a muscle to generate force, and thus joint torque, is a function of a number of factors: muscle length, speed of motion, muscle cross-section, muscle moment arm... Each muscle-joint complex is characterized by a torque versus joint angle curve, known as its strength curve (Figure 6.2a) (Kulig et al., 1984). The shape of the curve reflects the maximal joint torque generating capability throughout the range of motion. Factors such as fatigue, pain, lack of motivation and neurological disorders may affect the torque generating capability of a muscle-joint complex (Wrigley and Grant, 1995).

The well-known relationship between muscle force and contraction velocity was described by (Hill, 1938) based on experiments conducted on in-vitro specimens. A similar behavior has been observed for the in-vivo concentric torque-velocity relationship: joint torque declines as velocity increases. Eccentrically, joint torque remains more or less constant, regardless of velocity (Figure 6.2b).

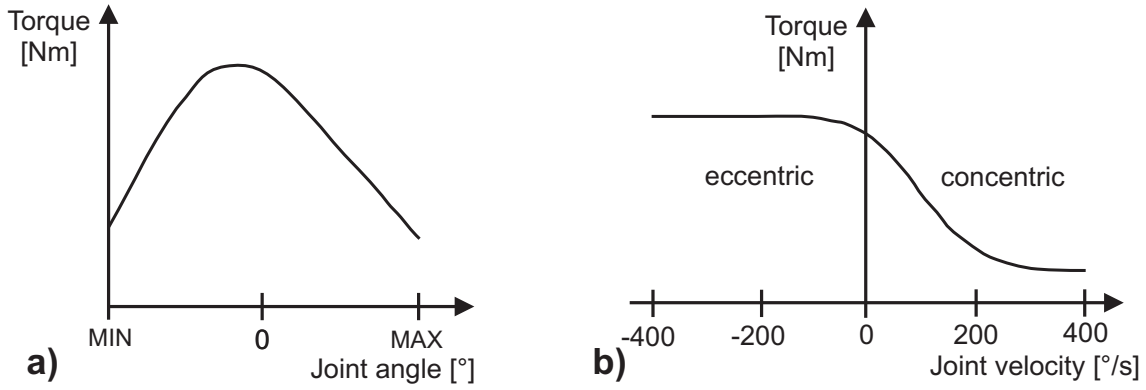

Figure 6.2: a) Typical torque/joint angle relationship - b) Typical torque/joint velocity relationship

6.2 Manual testing

Thanks to its inherent simplicity, manual testing is the most widely used method of muscular evaluation. The force developed by the muscle is characterized according to a six-level scale (Table 6.1), nearly identical to the one originally proposed by (Lovett and Martin, 1916). In order to discriminate grade 4 from grade 5, the examiner manually counteracts the motion of the patient and subjectively assesses the level of force developed (Figure 6.3). This subjectivity makes the results of testing difficult to use and compare. Furthermore, the ability of the examiner to determine when a patient's strength is "normal" is rather limited. Studies have shown that patients who had as much as 50% loss of absolute strength (as measured by quantitative methods, described in the following sections) were often rated as "normal" by manual muscle testing. Moreover, manual testing makes direct comparison of the same muscle group in the left and right extremities difficult to perform (differences in strength of less than 25% are difficult to detect).

5	- *normal* or full motion with full resistance
4	- *good* or full motion against gravity and some resistance
3	- *fair* or full motion against gravity only
2	- *poor* or full motion possible but with gravity eliminated
1	- *trace* or evidence of muscle contraction but with no motion
0	- *no muscle contraction*

Table 6.1: Reference scale for manual muscle testing [adapted from (Sapega, 1990)]

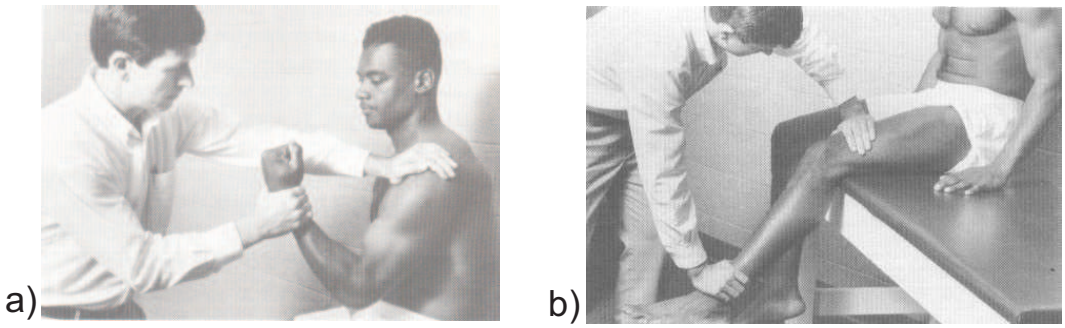

Figure 6.3: Manual testing of: a) upper - b) lower extremity [adapted from (Perrin, 1993)]

Another drawback of manual testing comes from the fact that adequate stabilization of the patient's body and extremities, to avoid muscle substitution, is difficult to achieve. Furthermore, the strength of the examiner upper extremities is often insufficient to counteract the strength of the patient lower extremity.

6.3 Isometric testing

Isometric muscle testing measures the muscle's maximum static peak force or corresponding joint torque. Muscle force development is thus not accompanied by any change in length and joint motion, the external resistance being equal to the torque developed by the muscle-joint complex (Croisier and Crielaard, 1999a) (Osternig, 2000). However, measures can be conducted at various angular positions to create a strength curve similar to the one generated by dynamic testing (Figure 6.7). Measurements, usually conducted with relatively inexpensive cable tensiometers have shown good to excellent repeatability. It should however be noticed that an uncontrolled positioning and stabilization of the patient's body as well as subject's fatigue and lack of motivation are major sources of discrepancies.

The fact that most of our muscles operate dynamically and not statically during daily physical activities may lead to the conclusion that results of isometric testing are not representative of normal muscle activity. However, studies have shown a good correlation between isometric and dynamic (isokinetic) test results.

The major drawback of isometric testing is related to the intrinsic static nature of this test leading to higher muscular and joint forces than with dynamic tests (cf. force-velocity relationship, see section 6.1.2). This test may thus be contraindicated in situations where high joint and muscle forces are undesirable (at the beginning of a rehabilitation period, for instance).

6.4 Isotonic testing and exercise

Isotonic testing corresponds to testing methods that involve an external constant load, usually using free weights or weight-lifting machines such as those found in fitness centers (Figure 6.4). It should however be noticed that the term "isotonic" is not entirely appropriate since, due to inertial forces, the load applied to the muscles is not really held constant throughout the range of motion.

Figure 6.4: Fitness machine used for isotonic testing and exercise (Nautilus)

The force of a particular muscle group is assessed by testing the maximum amount of weight that can be lifted throughout the joint's range of motion in a standardized manner (no excessive acceleration and deceleration, no muscle substitution), for either one or ten repetitions. The ten-repetition maximum or 10RM, originally proposed by (Delorme, 1951), is more a measurement of endurance than pure force (as opposed to the one repetition method). The isotonic testing method is thus time consuming since several evaluations (including rest periods) are required to determine maximum weight values.

Other limitations include the inability to control the test velocity and the fact that a muscle can be overloaded only by the amount of weight that can be lifted through the weakest point of the exercised range of motion (Figure 6.2). Machines equipped with elliptical transmission cams were designed to address this limitation, exhibiting a variable resistance to motion and still using constant weights. However, in such devices, the variation pattern of resistance is

fixed and does not adapt to each pathological situation (Croisier and Crielaard, 1999b).

These various drawbacks limit the use of isotonic devices for muscle force evaluation. In practice, these devices are essentially used for training and exercise. Furthermore, isotonic devices offer exercise configurations that are currently not available with other devices such as exercise of multiple joints simultaneously or exercises in "closed-kinetic-chain" (as opposed to a freely moving extremity) (Perrin, 1993).

6.5 Isokinetic testing and exercise

Isokinetic testing and exercise, introduced in the late 1960s by (Hislop and Perrine, 1967) (Thistle et al., 1967), is the most recent method of muscular evaluation and rehabilitation. In isokinetic devices, commonly called dynamometers (Figure 6.5), the angular velocity of the patient's joint is maintained constant (typical values are between 30°/s and 300°/s) thanks to a variable resistance that self-adapts to changes in torque developed by the patient throughout the range of motion, due to physiological changes (cf. strength curve), pain, fatigue and motivation.

Figure 6.5: Example of dynamometer used for isokinetic measurements (Biodex)

There are two types of dynamometers: passive and active. The passive type makes use of a brake that limits the speed of the patient's limb, allowing only evaluation of concentric contractions. The active type is based on a motor programmed to move at a constant speed as the patient exerts a torque on its output axis through the lever arm of the device. Both concentric and eccentric contractions can be evaluated. Furthermore, it should be noticed that, for both types of dynamometers, an initial acceleration phase, before reaching the predefined constant velocity, as well as a deceleration phase are unavoidable (Figure 6.6a). Depending on the device, the phases can be performed without any resistance or with a controlled acceleration-deceleration ramping, allowing to control the portion of the range of motion over

which velocity is not constant (Sapega, 1990). The portion of the range of motion where the patient's joint velocity is held constant is called the load range (Brown and Whitehurst, 2000), which is becoming increasingly smaller as the predefined constant velocity is increased. Figure 6.6b) shows this trend for knee extension at various predefined isokinetic velocities. This effect is also well illustrated in (Handel et al., 1996).

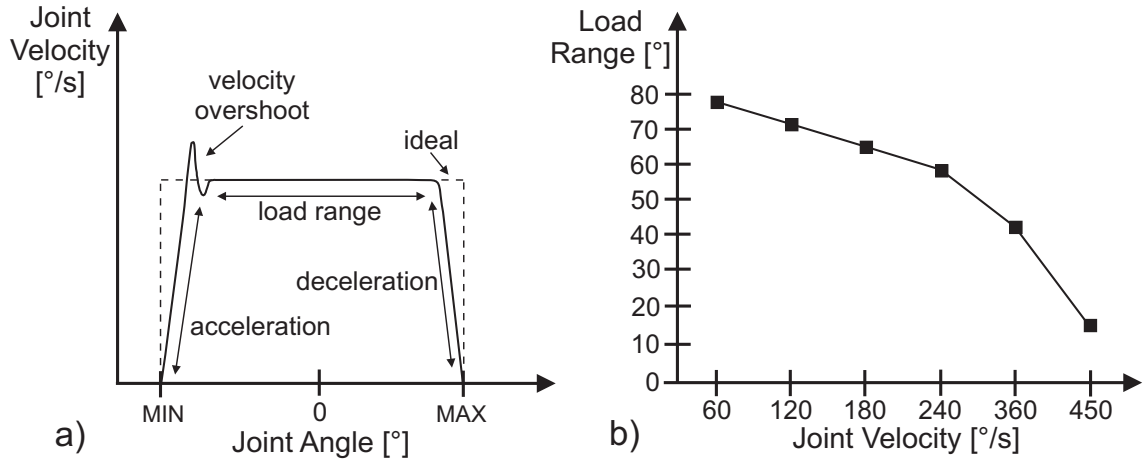

Figure 6.6: a) Typical acceleration and deceleration phases in isokinetic devices - b) Load range versus joint velocity in isokinetic devices [adapted from (Brown and Whitehurst, 2000)]

Since the patient's joint must pass through a free acceleration phase before meeting any resistance from the isokinetic device, inertial forces lead to velocity and torque overshoots (Figure 6.6a), with an amplitude growing with the level of predefined constant velocity.

Another problem linked to torque measurements encountered in isokinetic dynamometry is the effect of gravity (Winter et al., 1981). Indeed, for some motions, such as knee flexion, gravity assists the motion by pulling down on the limb and the device lever arm. On the contrary, for other motions, such as knee extension, the patient must lift the weight of his limb and the device lever arm. In the first situation, measured torque may be artificially increased due to gravity while the opposite is true for the second situation. Current isokinetic devices solve this problem by numerically correcting the effect of gravity before displaying the results (Perrin, 1993).

One major advantage of isokinetic exercises over isotonic exercises is that a muscle group may be dynamically evaluated and exercised to its maximum potential over the joint's entire range of motion, thanks to the variable resistance. Isometric testing also allows to measure maximum muscle force but only statically, at given locations of the range of motion. Figure 6.7 compares isometric, isotonic and isokinetic exercises.

Another advantage of isokinetic testing and exercise is its inherent safety. Indeed, thanks to the self-adapting resistance, any pain experienced by the patient will lead to a reduction in muscle generated torque that will cause the resistive torque of the isokinetic device to be proportionally reduced. This would not happen in an isotonic device, where the load would remain unchanged. An additional comment should be made about the safety of eccentric

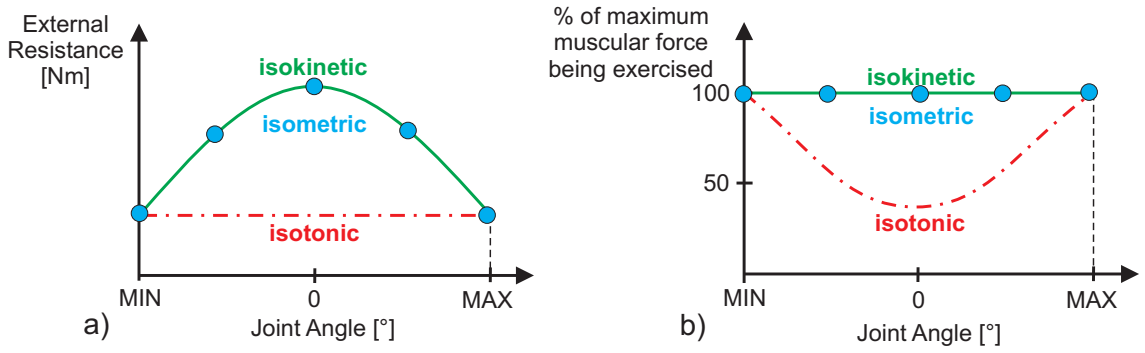

Figure 6.7: Schematic comparison of isometric, isotonic and isokinetic modes. The isokinetic mode auto-adapts its resistance to the muscular capabilities throughout the range of motion, which is not the case of the isotonic mode. The isometric mode provides only discrete measurements.

isokinetic exercise. Indeed, in that case, even if the torque of the device will adapt to patient resistance, motion will still be imposed to patient whatever the level of pain that may be experienced, leading to potential injuries if proper care is not taken by the practitioner.

The major disadvantage of isokinetic devices is their high cost, mainly limiting their use to muscle performance evaluation and testing, rehabilitation exercises being usually performed on less expensive devices (typically isotonic). Another drawback is that the evaluation of maximum muscle performance is highly dependent on patient motivation to apply force on the device. This effect can be reduced by providing the patient with appropriate instructions, strong verbal encouragements and visual feedback (e.g. computer graphic display).

All parameters analyzed during isokinetic testing are derived from four primary measurements: torque, joint angle, angular velocity and time. These can be computed and combined to provide a whole range of parameters that can be divided into three main categories (Wrigley and Grant, 1995):

1) *peak measures*: e.g. peak torque, angle of peak torque, peak power

2) *average parameters*: e.g. average torque, power or work

3) *time-based parameters*: e.g. time to peak torque, acceleration time

Work and power measurements are essentially useful in repetitive tests measuring endurance of the subject. Moreover, ratios comparing the performances achieved for agonist and antagonist motions (e.g. flexion/extension) can also be computed. Values obtained for the various parameters can be normalized by the weight of the subject to allow comparison with a reference population. Comparison between bilateral muscle groups (i.e. identic muscle groups belonging to right and left limbs) are also often realized (Perrin, 1993).

Many studies have shown that the intrinsic repeatability of commercial dynamometers in measuring torques is very high (Perrin, 1993) (Wrigley and Grant, 1995). However, measurement differences between two consecutive test are observed, essentially due to patient physiological

variability and errors in patient positioning relatively to the dynamometer axis. It is important to note that repeatability levels are also dependent on the measured parameter and the body joint that is evaluated. For instance, studies have shown that the repeatability of "peak torque" is much higher than for the "angle of peak torque" (Croisier and Crielaard, 1999a). In general, motions of easily isolated joints, such as the knee, tend to lead to higher repeatability than joints permitting involvement of accessory muscle groups, such as the shoulder. Repeatability is also smaller for joints with a smaller torque range, such as the wrist. Indeed, similar absolute torque variations have a higher relative impact for such joints (Chan and Maffulli, 1996). Table 6.2 summarizes the major characteristics of the previously described exercise modes; table 6.3 summarizes the main advantages and drawbacks of the various evaluation methods.

ISOMETRIC	**ISOTONIC**	**ISOKINETIC**
constant position	constant force	constant speed
static	dynamic	dynamic
applied resistance = max. muscle force but at discrete positions	applied resistance limited to weakest point in ROM	applied resistance = max. muscle force all over the ROM

Table 6.2: Major characteristics of muscular exercise modes

6.6 Degrees of freedom of the wrist

Since the device described in this thesis has been initially designed for the rehabilitation of the the wrist, the description and understanding of wrist biomechanics is of prime importance as it has an impact on some of the prototype's requirements.

6.6.1 Pronation-Supination

This motion can only be described and analyzed when the elbow is flexed at 90° and touching the body. Indeed, if the elbow is fully extended, the forearm is aligned with the upper-arm and the rotation of the upper-arm along its axis adds to the rotation of the forearm. The reference position is defined by the thumb up and the palm oriented towards the body. Full supination is achieved when the palm is up and the thumb is pointing away from the body (maximum amplitude: 90°). Full pronation is achieved when the palm is oriented towards the ground and the thumb is towards the body (maximum amplitude: 85°)(Figure 6.8). Average values of pronation peak torque for untrained male subjects vary from 7.3Nm to 12Nm while average values of supination peak torque vary from 9.1Nm to 11.2Nm (An et al., 1986) (Forthomme et al., 2004).

	ADVANTAGES	DISADVANTAGES
Manual	- easy to perform - no device needed	- high subjectivity in measurements - no real quantitative measures - difficulty to perform comparisons - difficulty to observe strength increase - low inter-observer repeatability - requires the presence of a kinesist
Isometric	- useful when joint motion is contraindicated or painful - no or low device cost - convenient for bed or home exercise - inherently safe	- strength increase specific to exercised joint position - lack of dynamic training
Isotonic	- combines concentric and eccentric resistance - progressive muscular reinforcement achieved from progressive increases in resistance - enables exercise of multiple joints simultaneously - enables closed-kinetic chain exercise - moderate device cost - OK for home exercise	- amount of resistance limited to the weakest point in ROM - high influence of weight inertia - evaluation difficult to perform and time-consuming - stronger muscle groups may compensate for weaker ones - can be unsafe for injured joints
Isokinetic	- enables maximal resistance throughout the range of motion - objective, repeatable and quantifiable measurements - inherently safe (in concentric mode) - enables evaluation and training of a specific joint - well suited for early rehabilitation	- high equipment cost - does not allow home exercise - only open-kinetic chain exercises - requires the presence of a kinesist - repeatability may be limited for some joints

Table 6.3: Comparison of the various modes of testing and exercise [adapted from (Perrin, 1993) (Chan and Maffulli, 1996)]

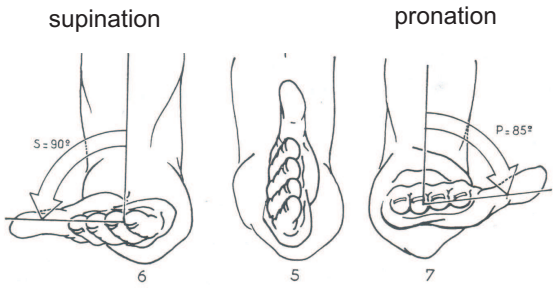

	ROM	Mean peak torque
pronation	0° - 85°	7.3 - 12 Nm
supination	0° - 90°	9.1 - 11.2 Nm

Figure 6.8: Pronation-Supination and associated ROM and peak torque, adapted from (Kapandji, 1980)

6.6.2 Flexion-Extension

For this motion, the reference position is defined by the third finger of the hand being aligned with the forearm axis. In flexion, the palm gets closer to the lower part of the forearm. In extension, the upper part of the hand gets closer to the upper part of the forearm. The amplitude of both motions is 85° (Figure 6.9). Average values of flexion peak torque (measured at speeds between 30°/s and 60°/s) vary from 13.7Nm to 26.2Nm while average values of extension peak torque vary from 4.7Nm to 12.7Nm (Vanswearingen, 1983), (Marley and Thomson, 2000) or (Forthomme et al., 2004).

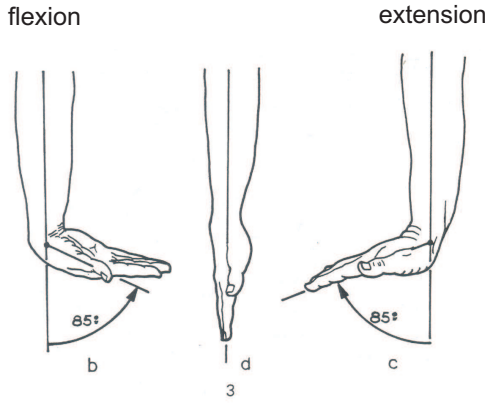

	ROM	Mean peak torque
flexion	0° - 85°	13.7 - 26.2 Nm
extension	0° - 85°	4.7 - 12.7 Nm

Figure 6.9: Flexion-Extension and associated ROM and peak torque, adapted from (Kapandji, 1980)

6.6.3 Abduction-Adduction

The reference position is the same as for the flexion-extension motion. In adduction, also called ulnar deviation, the hand moves in the direction of the fifth finger (maximum amplitude: 45°). In abduction, also called radial deviation, the hand moves in the direction of the thumb (maximum amplitude: 15°)(Figure 6.10). Depending on the source (Vanswearingen, 1983), (An et al., 1986), average values of abduction peak torque vary from 10.1Nm to 20.8Nm while average values of adduction peak torque vary from 7.5Nm to 17.8Nm.

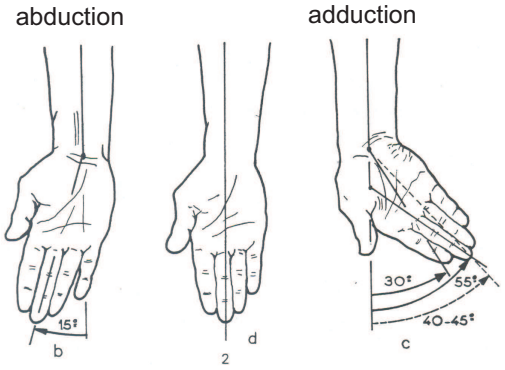

	ROM	Mean peak torque
abduction	0° - 15°	10.1 - 20.8 Nm
adduction	0° - 15°	7.5 - 17.8 Nm

Figure 6.10: Abduction-Adduction and associated ROM and peak torque, adapted from (Kapandji, 1980)

6.7 References

K.N. An, L.J. Askew, and E.Y. Chao. *Trends in Ergonomics/Human Factors III*, chapter : Biomechanics and functional assessment of upper extremities. North-Holland: Elsevier Science Publishers, 1986.

L.E. Brown and M. Whitehurst. *Isokinetics in Human Performance*, chapter 5: Load Range, pages 97–121. Human Kinetics, 2000.

K-M. Chan and N. Maffulli. *Principles and Practice of Isokinetics in Sports Medecine and Rehabilitation*. Williams and Wilkins, Hong-Kong, 1996.

J.L. Croisier and J.M. Crielaard. Exploration isocinétique: Analyse des paramètres chiffrés. *Annales de Réadaptation et de Médecine Physique*, 42:538–545, 1999a.

J.L. Croisier and J.M. Crielaard. Methodes d'exploration de la force musculaire: Une analyse critique. *Annales de Réadaptation et de Médecine Physique*, 42:311–322, 1999b.

T.L. Delorme. *Progressive Resistance Exercise*. Appleton-Century-Crofts, New York, 1951.

B. Forthomme, J.L. Croisier, M. Foidart, and J.M. Crielaard. Exploration isocinétique de l'avant-bras et du poignet - méthodologie et application à une pathologie tendineuse. *Journal de Traumatologie du Sport*, 21:80–87, 2004.

M. Handel, H.H. Dickhuth, F. Mayer, and R.W. Gülch. Prerequiste and limitations to isokinetic measurements in humans. *European Journal of Applied Physiology*, 73:225–230, 1996.

A.V. Hill. The heat of shortening and the dynamic constants of muscle. *Proceedings of the Royal Society*, B126:136–195, 1938.

H. Hislop and I. Perrine. The isokinetic concept of exercise. *Physical Therapy*, 47:114–117, 1967.

I.A. Kapandji. *Physiologie Articulaire*. Maloine S.A. Editeur, 1980.

K. Kulig, J.G. Andrews, and J.G. Hay. *Exercise and Sport Science Reviews*, volume 12, pages 417–466. Macmillan, 1984.

R.W. Lovett and E.G. Martin. Certain aspects of infantile paralysis with a description of a method of muscle testing. *Journal of the American Medical Association*, 66:729–733, 1916.

R.J. Marley and M.R. Thomson. Isokinetic strength characteristics in wrist flexion and extension. *International Journal of Industrial Ergonomics*, 25:633–643, 2000.

L.R. Osternig. *Isokinetics in Human Performance*, chapter 4: Assessing human performance, pages 77–96. Human Kinetics, 2000.

D.H. Perrin. *Isokinetic Exercise and Assessment*. Human Kinetics Publishers, 1993.

A.A. Sapega. Muscle performance evaluation in orthopaedic practice. *Journal of Bone and Joint Surgery*, 72:1562–1574, 1990.

H. Thistle, H. Hislop, M. Moffroid, and E. Lohman. Isokinetic contraction: A new concept of resistive exercise. *Archives of physical medecine and contraction*, 48:279–282, 1967.

J.M. Vanswearingen. Measuring wrist muscle strength. *Journal of Orthopaedic and Sport Physical Therapy*, 4:217–228, 1983.

D.A. Winter, R.P. Wells, and G.W. Orr. Errors in the use of isokinetic dynamometers. *European Journal of Applied Physiology*, 46:397–408, 1981.

T. Wrigley and M. Grant. *Sports Physiotherapy - Applied Science and Practice*, chapter 17: Isokinetic Dynamometry, pages 259–283. Churchill Livingstone, 1995.

Chapter 7

Portable wrist rehabilitation device

7.1 System components

Figure 7.1 shows a schematic view of the system. The rehabilitation device is composed of three major subsystems: mechanical hardware (including sensors), embedded electronics and user interfaces (PC and PDA). The three major exercise modes are implemented: isometric, isotonic and isokinetic.

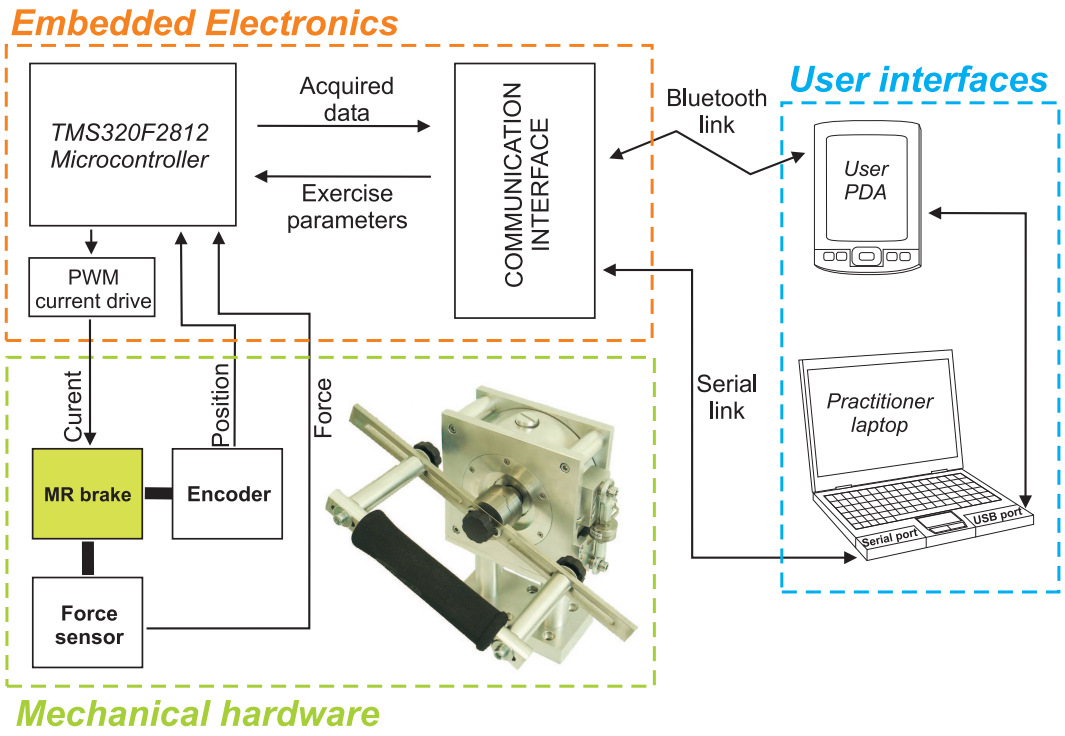

Figure 7.1: Main components of the prototype

The heart of the device is a rotational MR-brake connected to its support through two bearings. A compact tension/compression load cell (ELPF-T3M-2.5kN from Measurement Specialities) provides an indirect torque measurement by blocking the rotation of the brake on its support, measuring in that way the reaction force applied to the brake stator when a

torque is applied on the rotor of the energized brake. A similar configuration can be found in (Krukowski, 1988) describing a rehabilitation device making use of a particle brake clutch. An incremental two channels optical encoder, having 500 pulses/revolution (HEDL55 from HP) is also connected to the rotor of the brake, providing position and speed measurements (Figure 7.2).

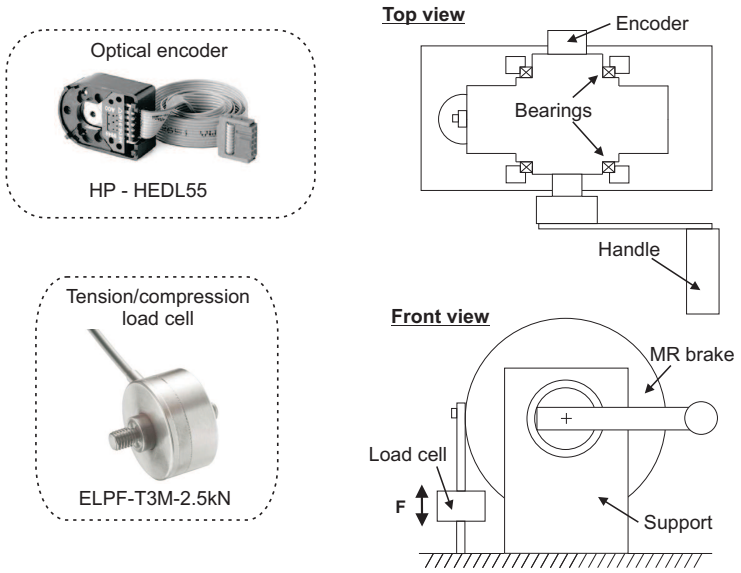

Figure 7.2: Sensors implemented in the device prototype

A mechanical positioning system is also used in combination with the device in order to achieve a repeatable positioning of the patient's wrist relatively to the device between two consecutive exercise sessions (Figure 7.3). This system enables to adjust the three translations (X,Y,Z) and is attached to the patient forearm through an orthosis and an additional part blocking the elbow motion. Various handles have also been designed to allow exercises of all the DOF of the wrist. More details are given in the related patent, available in Appendix B.

7.2 MR brake

In recent years, various groups have been working on the development of portable computerized isokinetic devices. (Mavroidis et al., 2005) have developed various smart portable rehabilitation devices among which a knee rehabilitation orthotic device based on an ER-fluid brake (Nikitczuk et al., 2007). A forearm rehabilitation device, based on the same type of actuator has been developed by (Kikuchi et al., 2003). (Dong, 2005) also developed an isokinetic knee rehabilitation device but actuated by a MR-fluid linear damper. It is however interesting to note that, to our knowledge, only one forearm rehabilitation device using a rotational MR-brake has been reported in the literature (Carlson, 2000). This device only implements isotonic exercises and does not offer any visual feedback to the patient and practitioner.

However, rotational MR-brakes seem particularly well suited to be used in rehabilitation devices. Indeed, on the contrary of D-C motors, they are passive devices that are only able to

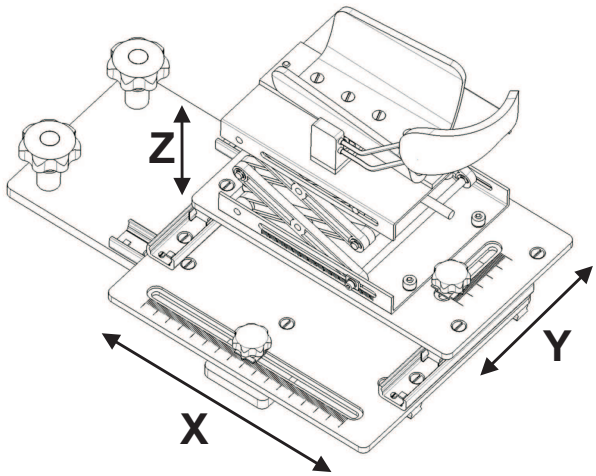

Figure 7.3: Positioning system for the forearm

dissipate power applied by the patient, increasing in that way the inherent safety of the device. Moreover, as one of the commonly implemented exercise mode (isotonic) requires the output shaft to remain blocked in a given position for a long period of time, brakes are preferred to DC-motors since they are very inefficient under such working conditions. MR-brakes exhibit high dynamic ranges and high torque/volume ratios (much higher than other types of brakes and, in particular, ER-brakes), enabling them to be used without reducer and alleviating the need for friction compensation at low torques. MR-brakes are also characterized by low voltage and current requirements as well as fast response time, which are also advantages for portable real-time applications. Finally, rotational MR-brakes are much more suited than linear devices to be used in rehabilitation devices due to the rotational nature of the exercises to be performed. All these elements support the selection of a rotational MR-brake for the portable rehabilitation device considered in this thesis.

To our knowledge, only three models of rotational MR-brakes are commercially available, all of them being manufactured by LORD corporation. The most powerful one exhibits a maximum output torque of 12Nm, which is not enough for a wrist rehabilitation device (see maximum wrist torques in section 6.6).

Various MR-brake architectures can be found in the literature. From the comparative analysis conducted in chapter 4, the T-shaped rotor is a good compromise in terms of compactness, mechanical complexity, power requirements and dynamic range. The device developed in this study has a maximum output torque of 28Nm with an external diameter of 120mm. Figure 7.4 shows a sketch of the internal shape of the brake and the results of the FE magnetic analysis. The magnetic flux intensity reaches the required value in the MR-fluid gap and is just below saturation level in the iron core, as expected. Figure 7.5a) shows a picture of the main brake components.

Various experiments have been conducted to validate the intensity of the magnetic flux in the gap. Values obtained via FE analysis without MR-fluid in the gap have been compared with measurements conducted with a teslameter on both iron cores (Figure 7.5b).

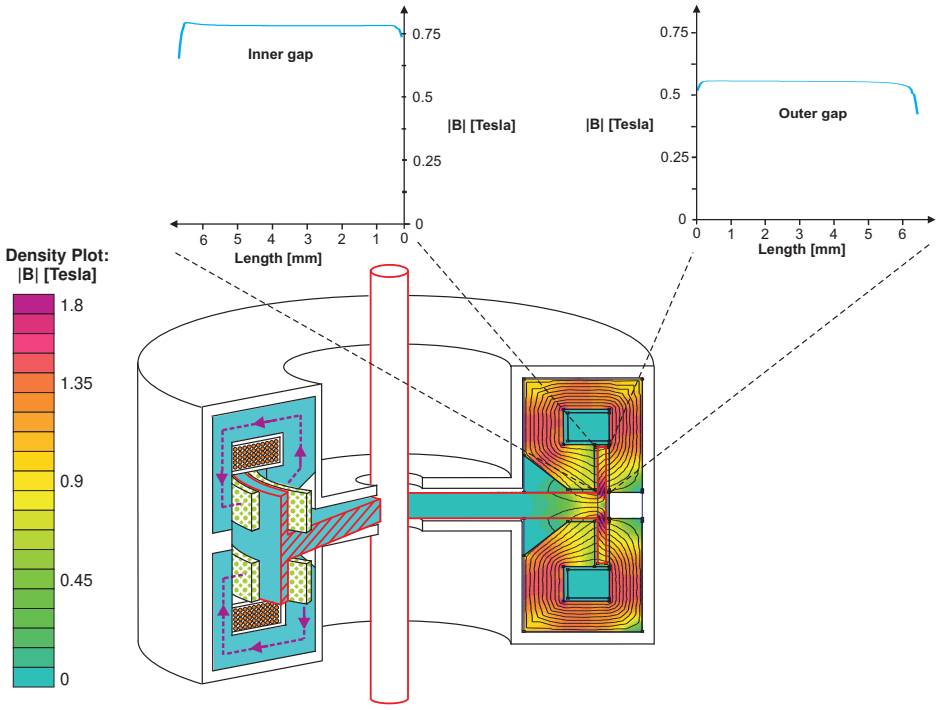

Figure 7.4: FE analysis of the magnetic circuit of the T-shaped MR-brake (obtained with FEMM)

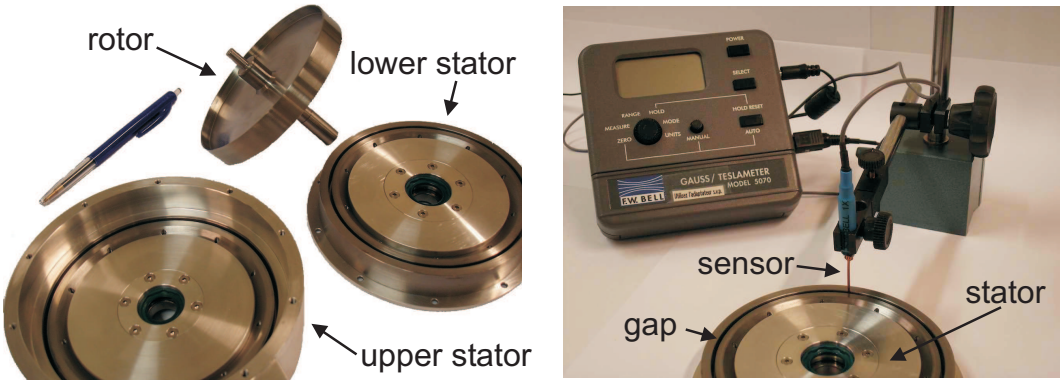

Figure 7.5: a) Picture of the MR-brake main components - b) Experimental setup for B-field measurement in the gap

Curves of the magnetic flux density (B) in the gap versus current in the coil for both iron cores exhibit a good agreement between simulation and experience (Figure 7.6), validating in this way the results obtained via FE analysis below iron core saturation.

The brake design shown at Figure 7.5 is only a laboratory prototype. An illustration of what could be an industrial version of this brake, with a molded carter, is shown at Figure 7.7.

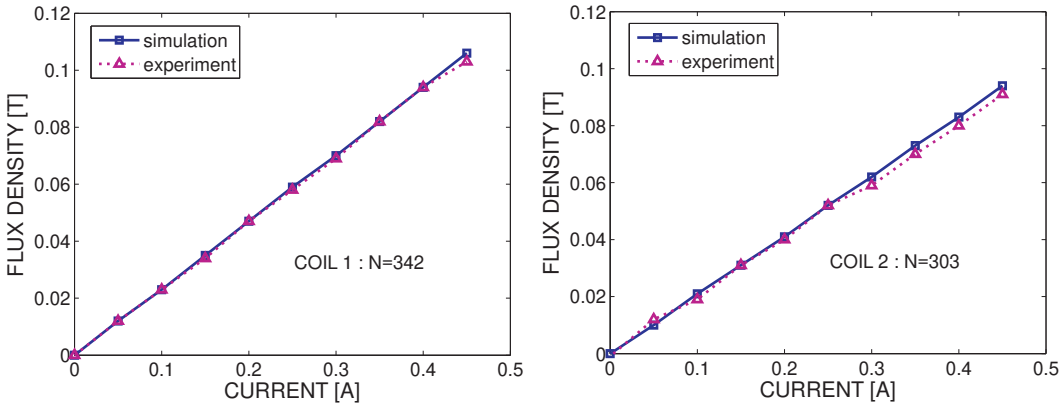

Figure 7.6: Magnetic flux intensity versus coil current in the gap for both iron cores (the number of turns N varies from coil to coil due to the manufacturing process)

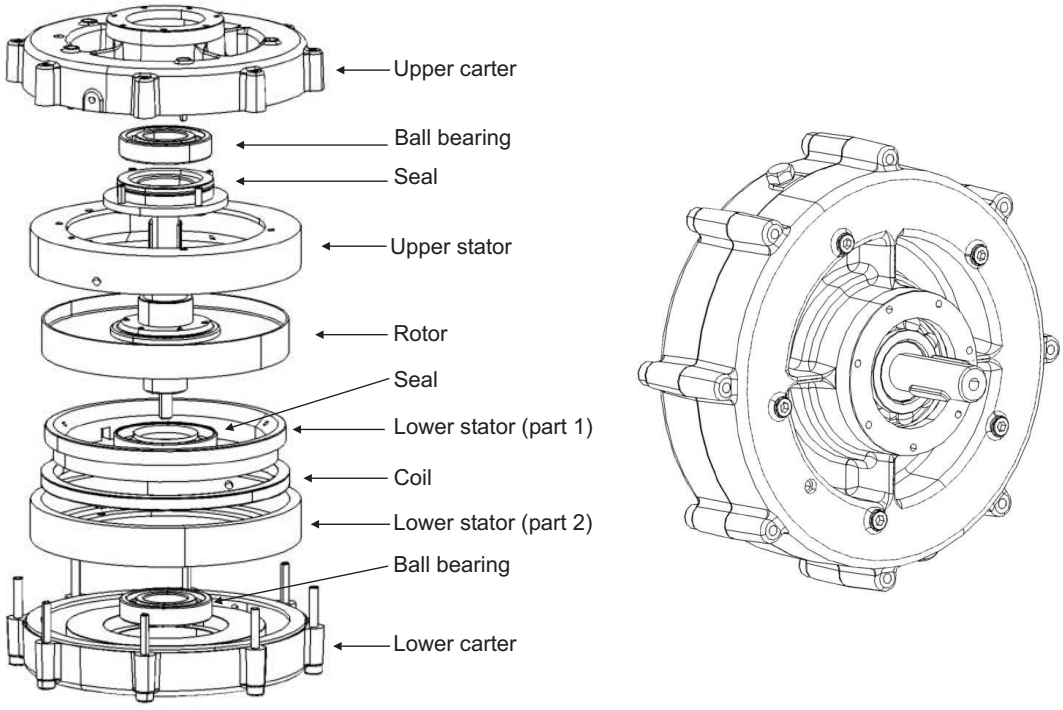

Figure 7.7: Possible industrial version of the MR-brake

Due to the large size of the brake and the very small MR-fluid gap thickness (0.4mm), a vacuum pump is used to fill the MR-fluid in the brake. The first step is to create vacuum inside the brake thanks to a vacuum pump; then, the valve linking the device to the MR-fluid reservoir is opened and the fluid is sucked in the device.

Once the brake was filled with MR-fluid, its performances were measured and compared to its expected behavior obtained from FE analysis. In particular, its torque versus current characteristic has been measured (Figure 7.8). It can be observed that iron core saturation appears earlier than expected due to imprecise modelling of iron core magnetic properties (unknown B-H curve), leading to a lower maximum torque value (about 22.5Nm). As with the early brake prototypes, a hysteretic non-linear behavior can be observed. This MR-brake also exhibits an off-state torque (of about 2Nm) due to remanent magnetic field, which was not observed with the early prototypes. This may be explained by the fact that high speed machining was used to manufacture this prototype, leading to magnetic hardening, which was not the case with the previous ones.

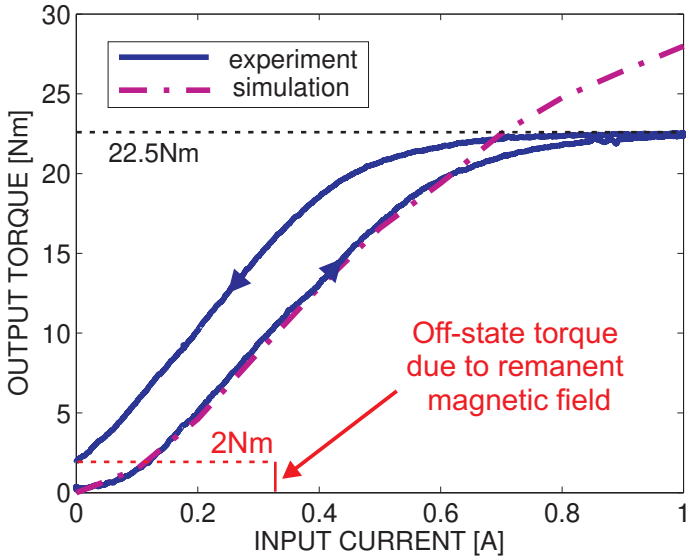

Figure 7.8: Torque-current characteristic of the MR-brake

7.3 Prototype of embedded electronics

Figure 7.9 shows a schematic view of the system with emphasis on the embedded electronics. It consists of three main components: a Texas Instrument eZDSP-F2812 evaluation board, a sensor interface and power board designed by Micromega Dynamics and a Bluetooth evaluation board (Bluegiga WT12).

The eZDSP evaluation board comprises, among other components, the following elements:

- a microprocessor (TMS320F2812), where the control algorithms of the device are implemented. It is also used for speed and torque computation as well as for real time communication management with the user interfaces (based on the SLIP protocol)

- a QEP encoder interface (acquisition of position measurement)

- two analog inputs (AI) (acquisition of force and current measurements)

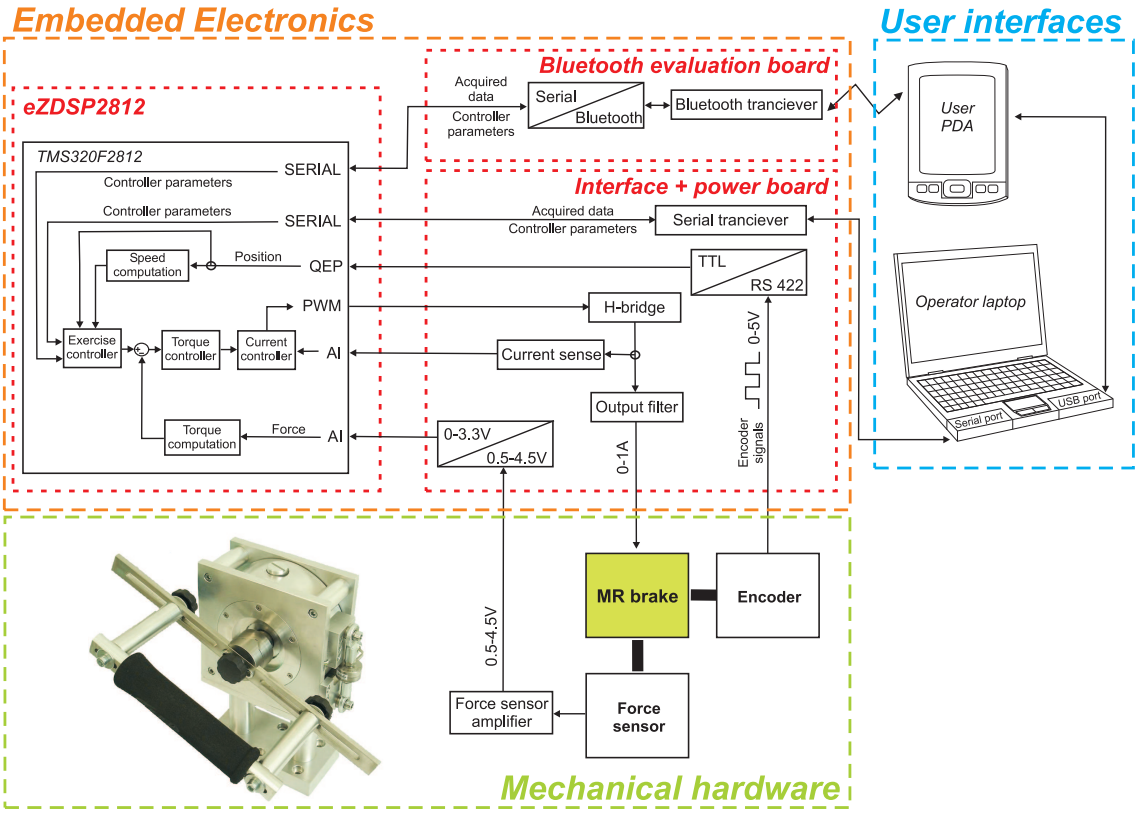

Figure 7.9: Schematic view of the embedded electronics

- a PWM output driving the H-bridge of the power board, delivering current to the MR-brake
- serial input/output for communication with the interfaces

The sensor interface and power board comprises:

- a H-bridge and a current probe required to implement a current loop
- signal converters to adapt encoder and force sensor signals to microprocessor inputs

The Bluetooth evaluation board converts the signals of the serial port into Bluetooth signals and is thus "transparent" to the user. Figure 7.10 shows a picture of the embedded electronics prototype; a commercial product would combine all these components on a single board.

7.4 User interfaces

Since the device was designed for home use, two user interfaces have been considered: the first one is a laptop equipped with a software (similar to those found on commercial isokinetic machines) containing a patient database and that is used by the practitioner to define the various exercises to be performed by the patient, set their parameters, display and analyze

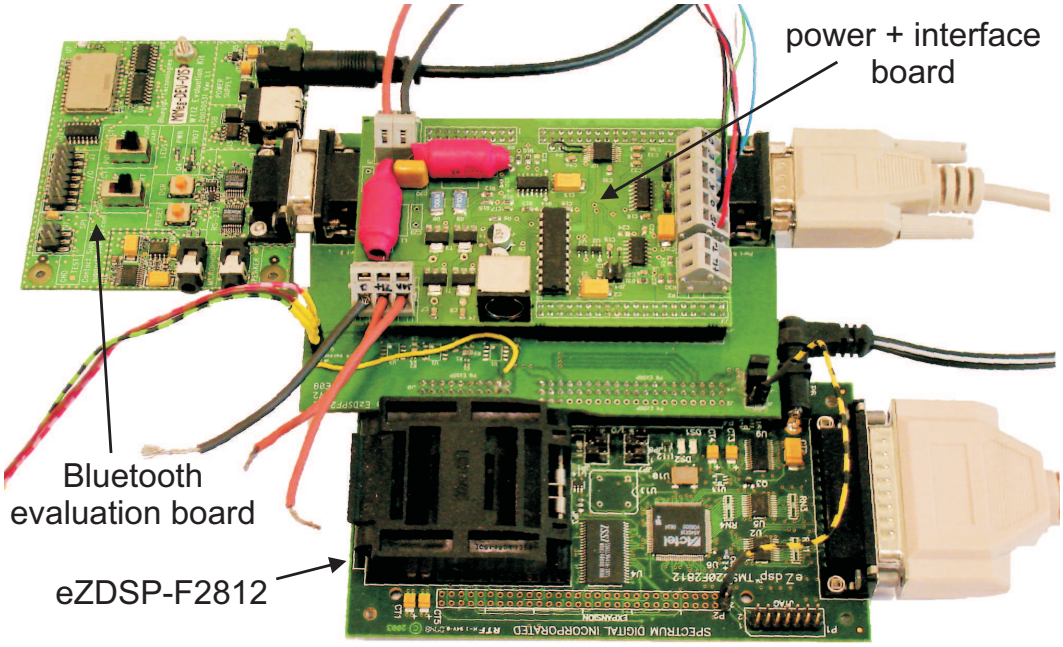

Figure 7.10: Picture of the embedded electronics prototype

the data acquired during the exercise (either in real-time or later on, after several exercises). Figure 7.11 shows a typical report generated by the software for post-exercise analysis by the practitioner. The second one is a PDA that enables the patient to use the device alone at home. The practitioner defines in advance the exercises to be performed by the patient with the software installed on his laptop. Then, the exercise parameters are transferred from the laptop to the PDA that will automatically ask the patient to perform the scheduled exercises every time the device is switched on (Figure 7.12a). A simplified visual feedback (including exercise validation messages) is provided to the patient on the PDA while the exercise is being performed (Figure 7.12b). Exercises are stored on the PDA until the patient transmits them to the practitioner (by connecting the PDA to his laptop), who can analyze them and prescribe new exercises.

7.5 DSP and Control Desk interface

In order to be able to test the device prototype independently from the embedded electronics prototype and allow parallel developments, the mechanical hardware has been initially combined with a dSpace PC-based acquisition board used in combination with the Control Desk software package emulating the future user interface. The control has been implemented using MATLAB Simulink, allowing easy modifications and testing. Figure 7.13 shows a typical view of a Control Desk window emulating the user interface (here, for the isometric mode).

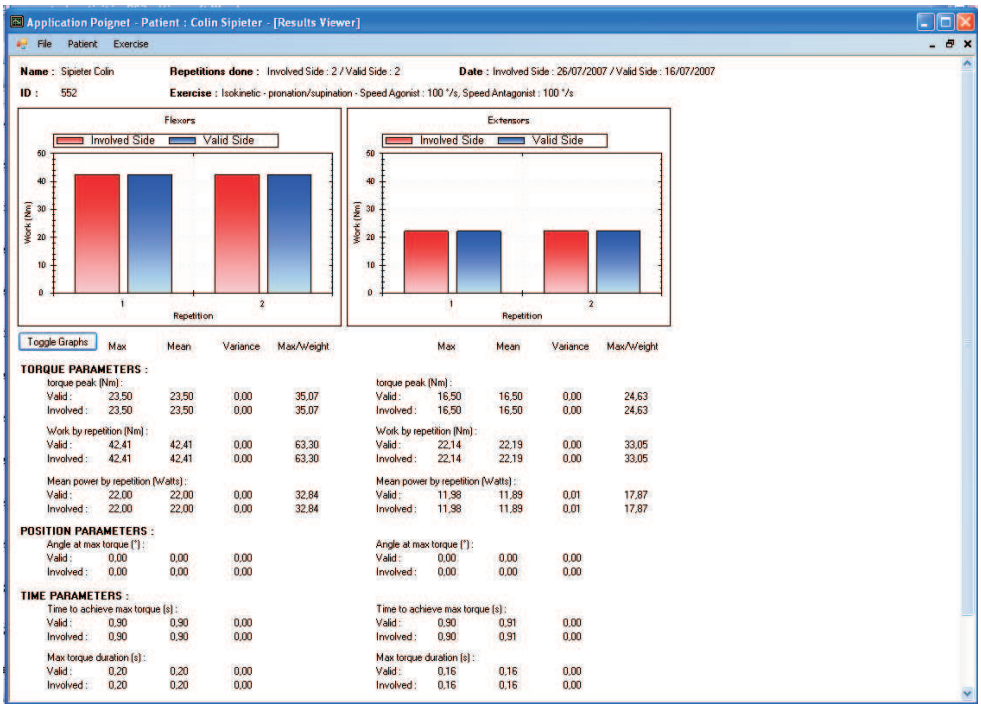

Figure 7.11: Typical report for post-exercise analysis generated by the user interface

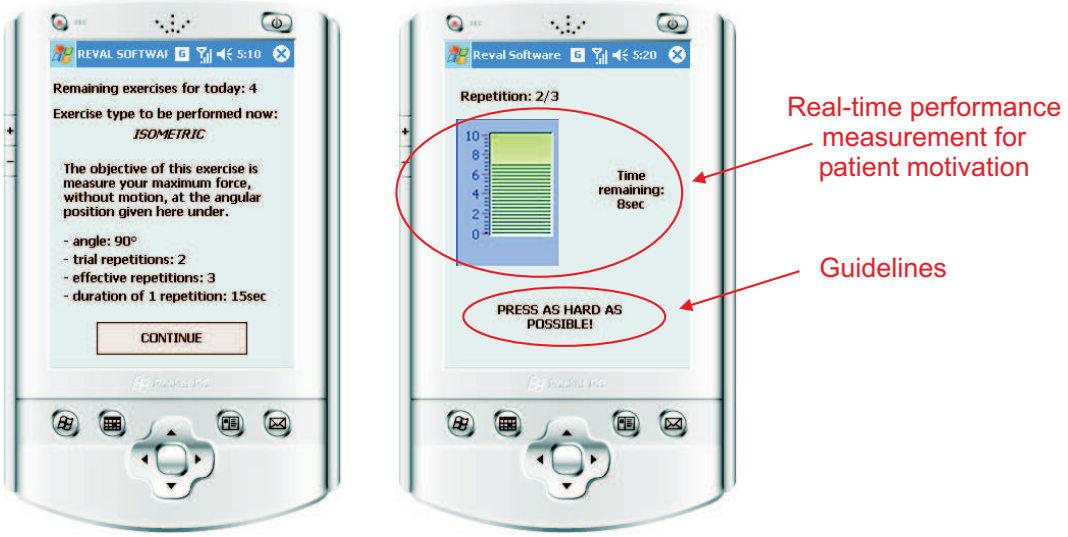

Figure 7.12: a) Exercise description on PDA - b) Exercise simplified feedback on PDA

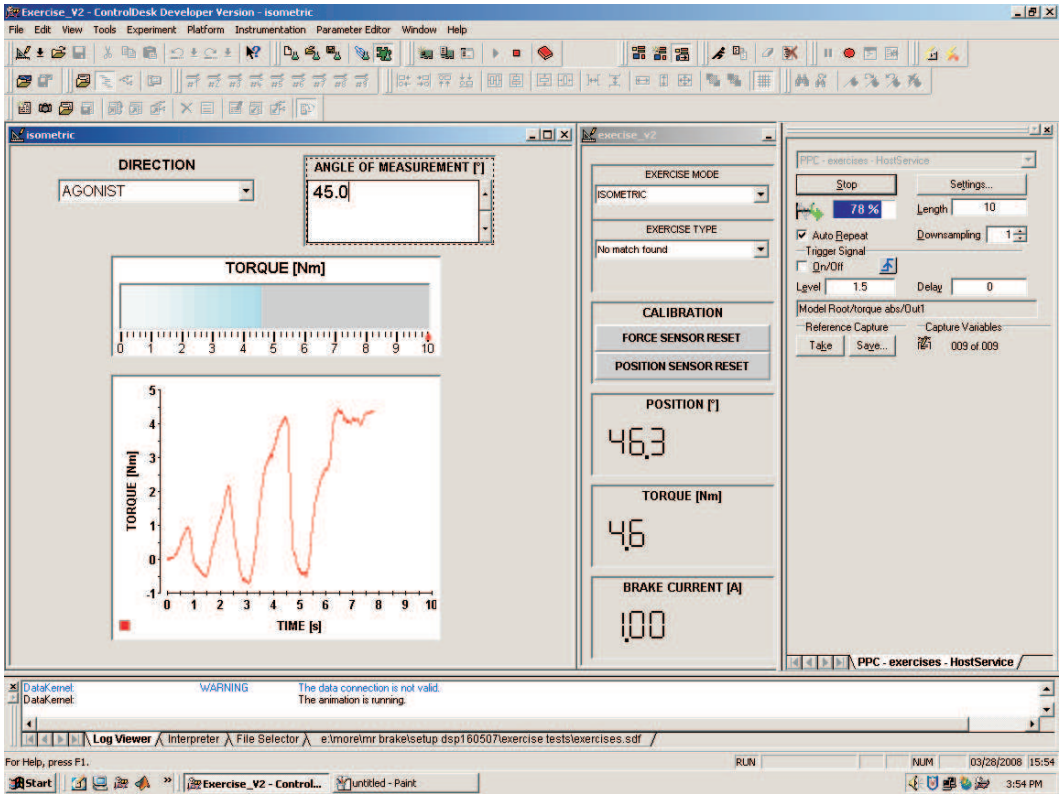

Figure 7.13: Screenshot of emulated user interface with Control Desk

7.6 References

J.D. Carlson. Portable hand and wrist rehabilitation device. US patent 6,117,093, 2000.

S. Dong. *Development and Control of Variable Resistance Exercice Device with Magnetorheological Fluids*. PhD thesis, University of Delaware, 2005.

T. Kikuchi, J. Furusho, and K. Oda. Development of isokinetic exercise machine using ER brake. In *Proceedings of the IEEE International Conference on Robotics and Automation*, pages 214–219, Taipei, Taiwan, 2003.

R. Krukowski. Particle brake clutch muscle exercise and rehabilitation apparatus. US patent 4,765,315, 1988.

C. Mavroidis, J. Nikitczuk, B. Weinberg, G. Danaher, K. Jensen, P. Pelletier, J. Prugnarola, R. Stuart, R. Arango, M. Leahey, R. Pavone, A. Provo, and D. Yasevac. Smart portable rehabilitation devices. *Journal of NeuroEngineering and Rehabilitation*, 2(18), 2005.

J. Nikitczuk, B. Weinberg, and C. Mavroidis. Control of electro-rheological fluid based resistive torque elements for use in active rehabilitation devices. *Smart Materials and Structures*, 16:418–428, 2007.

Chapter 8

Control strategies

8.1 Global control scheme

The control strategy (Figure 8.1) consists of three overlapping control loops (Dong, 2005). The first control loop (not shown in Figure 8.1), implemented within the current drive, is a current loop used to compensate for the electrical phase-shift related to the use of coils to generate the magnetic field inside the brake. The second control loop is a torque loop used to compensate for the imperfections of the relation between the current applied to the brake and its output torque (non-linearity, hysteresis, remanence, etc). The third loop is a motion loop used to control the motion of the shaft of the device according to the selected exercise mode (isometric, isotonic and isokinetic). All these controllers described in more details in the following sections, have been first evaluated on the test bench described in section 5.2 and then implemented on the rehabilitation device.

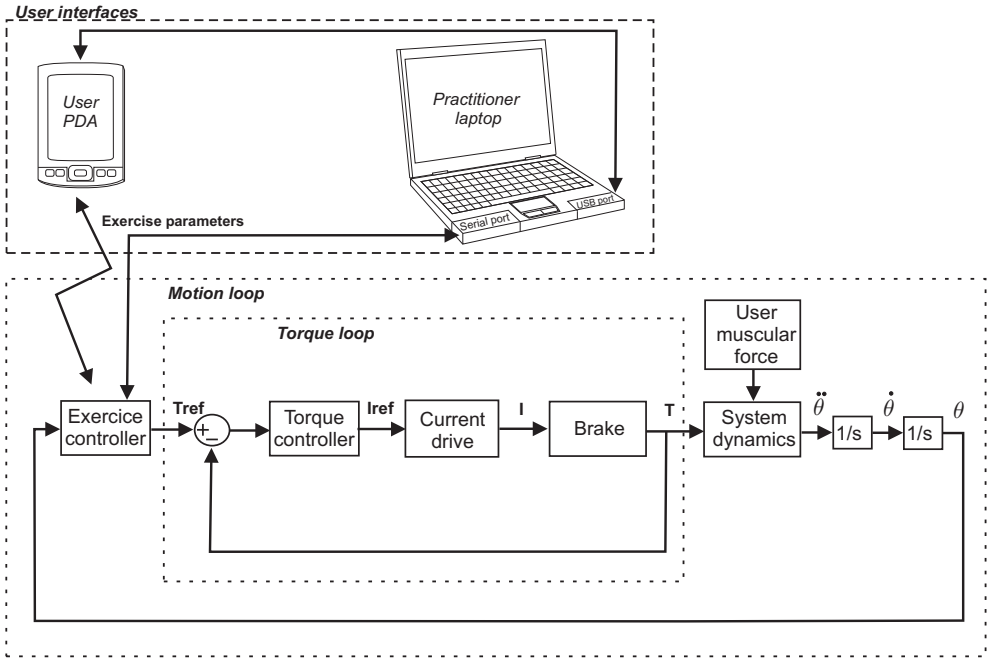

Figure 8.1: Global control scheme of the rehabilitation device

8.2 Simulation of the experimental setup

In order to facilitate the development of the various control algorithms, a simulator of the test bench described at section 5.2 has been developed under MATLAB Simulink.

The DC motor is modelled with the following equations:

$$V - V_{emf} = ri + L\frac{di}{dt} \tag{8.1}$$

$$V_{emf} = k_s\dot{\theta} \tag{8.2}$$

$$T = k_T i \tag{8.3}$$

where V is the applied voltage, i the input current, T the output torque, k_T the motor torque constant, k_s the motor speed constant and V_{emf} the back electromotive force. The saturation of the current drive is also modelled. The gearbox connected to the motor is simply modelled by its reduction ratio (no friction model).

The MR-brake is modelled by the measured torque/current characteristics (see section 5.3.2). The non-linear hysteretic behavior of this relationship is modelled in the same way as in (Liu et al., 2006): the main hysteresis loop is approximated by a parallelogram with inner sub-hysteresis cycles of similar shape (Figure 8.2a). This model is fully characterized by only four parameters (T_0, T_1, S_1, S_2) that were adjusted to fit the experimental curve (Figure 8.2b).

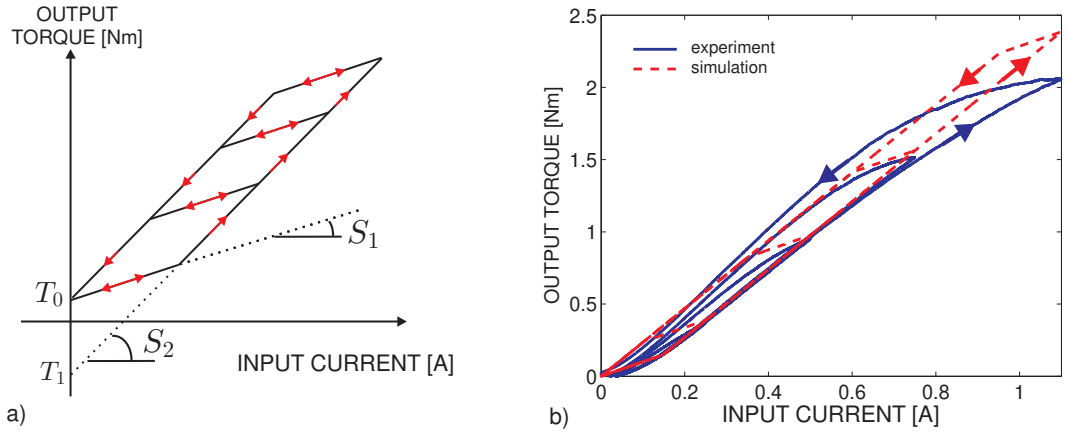

Figure 8.2: a) Hysteresis model - b) Fitting with experimental data

As can be observed from (Figure 8.2b), the selected model does not perfectly fit the experimental data but presents the advantage of being easy to implement. Furthermore, as it will be seen later, it is enough to support the development of the various control laws.

The hysteretic behavior of the torque/current characteristic being essentially determined by the hysteresis within the magnetic core of the brake, models describing the hysteresis in ferromagnetic materials can also be used, such as Preisach or Hodgdon models (Mayergoyz, 1988) (Hodgdon, 1988) (An and Kwon, 2003). Such models may offer a better fit of experimental data but are more complex to implement and require a good knowledge of the

magnetic characteristics of the material used within the magnetic core (B-H curve...).

The core of the simulation is schematically represented at Figure 8.3. The torque delivered by the brake and the seal friction (modelled as dry friction) counteract the motor output torque. By dividing the total torque by the total inertia (I), one gets the acceleration of the system as well as speed and position signals.

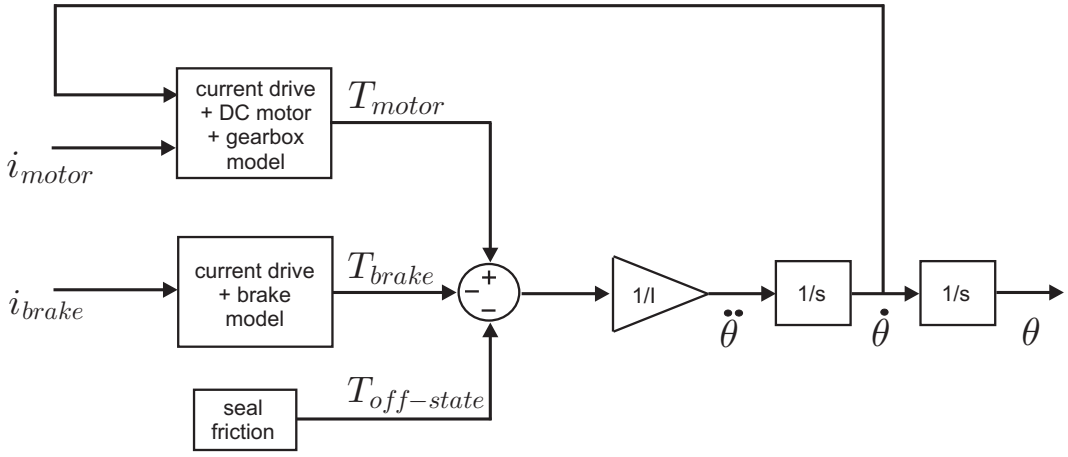

Figure 8.3: Schematic view of the test bench simulator

8.3 Torque controller

Due to the hysteretic torque/current characteristic of the MR-brake, a torque controller is necessary to ensure the desired torque output at all times, independently of the system history.

The MR-brake being non-linear by essence, the torque controller (Figure 8.4) is also non-linear, with two different cases. When the axis of the brake is moving ($speed \neq 0$), the torque measured by the sensor equals the torque produced by the brake. In that case, a simple PID controller (having as input the torque error) is used in combination with a feedforward term (based on the current/torque characteristic of the brake). A saturation is applied to the output of the controller to avoid sending negative currents to the brake, which does not make any sense. When the brake axis is idle ($speed = 0$), the torque measured by the sensor equals the torque produced by the motor (or patient) and does not reflect the resistive torque developed by the brake, and a PID controller based on the torque error can not be used to generate the current command of the brake. Instead, only the feedforward term is used, in open-loop.

It is important to note that, since the system is working at low speeds, the speed signal derived from encoder measurements is of poor quality and thus switching between the two cases is not based on speed but on position measurements. Speed is considered to be different from zero if the position has changed between measurements conducted at sample times t and $(t - X)$ (in our application $X = 100$, with a sampling frequency (f) of 1kHz) or between

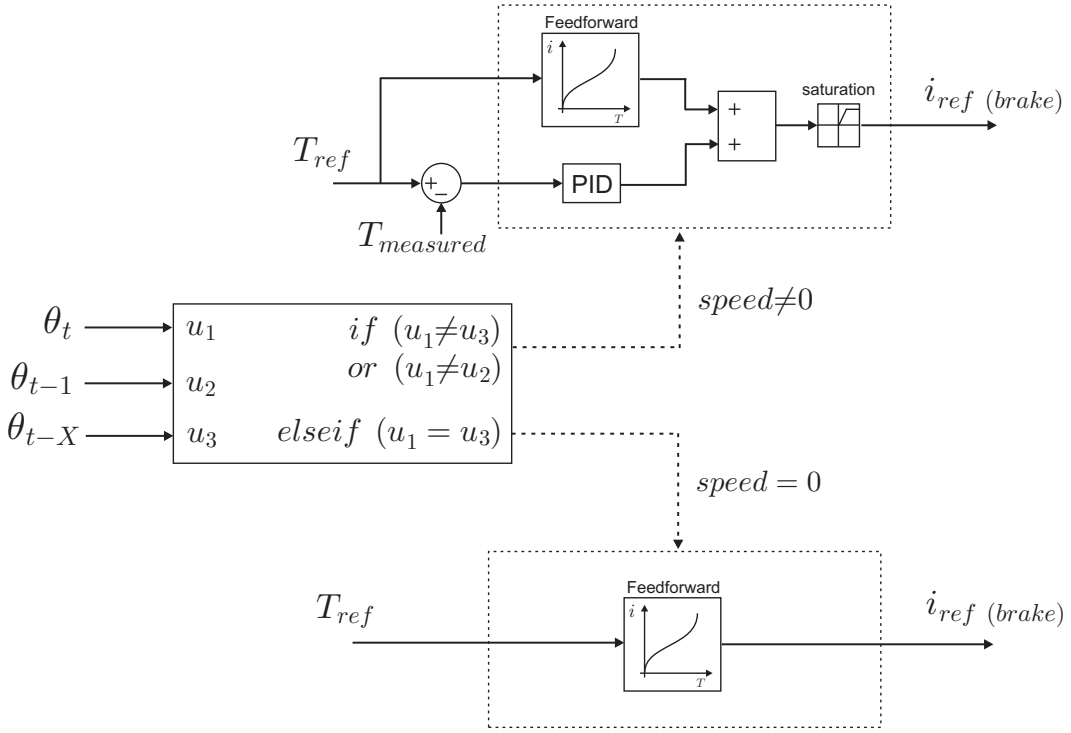

Figure 8.4: Schematic view of the torque controller

two successive sample times (to take into account sudden changes in speed). If the position remains unchanged between t and $(t - X)$, the speed is considered equal to zero.

Knowing the encoder resolution (res):

$$res = \frac{360^\circ}{\#pulses} = \frac{360^\circ}{2000} = 0.18^\circ \tag{8.4}$$

one gets the lowest speed value that can be detected (s):

$$s = \frac{res.f}{X} = 1.8^\circ/s \tag{8.5}$$

In order to validate the usefulness of the torque controller, step variations of the torque set-point have been applied to the brake while the speed of the motor of the test bench was maintained constant ($360^\circ/s$). From Figure 8.5, it can be observed that, without torque control, due to the hysteresis within the brake, a drift appears between the command and the actual torque value when going from a higher to a lower torque command. This phenomenon is fully eliminated when torque control is activated. This effect is observed on both experiment and simulation but with various amplitudes due to differences between the experimental and modelled hysteresis curves.

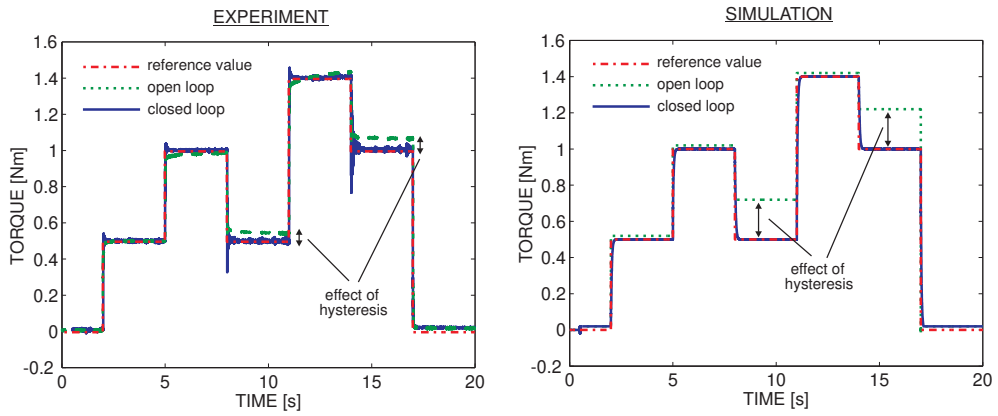

Figure 8.5: Step variations of the torque setpoint of the brake at constant speed

8.4 Exercise controller

8.4.1 Isometric control

The control of the isometric mode is based on a position controller that implements a hard stop if the measurement position (θ_{ref}) is reached and if the patient (or motor) applies a force in the right direction (agonist or antagonist, detected via the sign of the torque measurement). In order to simulate such a hard contact, when the measurement position (θ_{ref}) has been reached, a torque command proportional to the difference between the current position ($\theta_{measured}$) and the reference position (θ_{ref}) is sent to the torque controller:

$$T_{ref} = k(\theta_{measured} - \theta_{ref}) \tag{8.6}$$

where k is the contact stiffness. For the isometric exercise, k is set to a high value. Results obtained for the isometric control ($k = 1\text{Nm}/^\circ$), at various measurement positions, on the test bench and with its simulator, are presented at Figure 8.6. The motion is properly blocked at the reference position and a good level of correspondence can be observed between simulation and experiment. The input of the patient on the system was simulated by commanding the motor with a square periodic speed setpoint (amplitude: $120^\circ/s$).

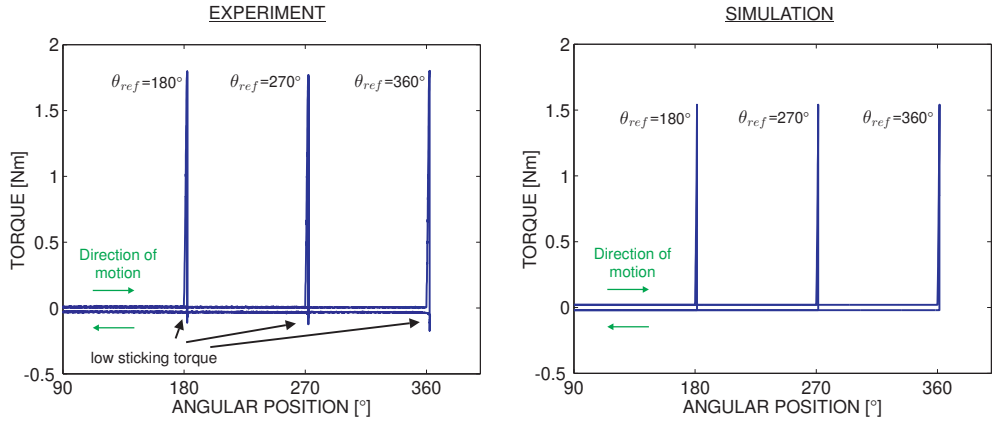

Figure 8.6: Results for the isometric mode on both test bench and simulator

The same control law applied to the rehabilitation device leads to the results of Figure 8.7, for the pronation motion of the wrist, at various measurement positions (θ_{ref}: 0°, 30°, 60°, 90°). The user is perfectly blocked at the various measurement positions (vertical lines) and that he is able to leave these positions with a very limited sticking force (which can hardly be felt) thanks to the control strategy used. Furthermore, the off-state torque remains low, which facilitates wrist motion before reaching the measurement position. It can also be observed that the maximum torque delivered by the user decreases with the angular position, which is linked to the parabolic shape of the strength curve. Maximum torque values are in accordance with values reported in the literature (An et al., 1986) (Forthomme et al., 2004).

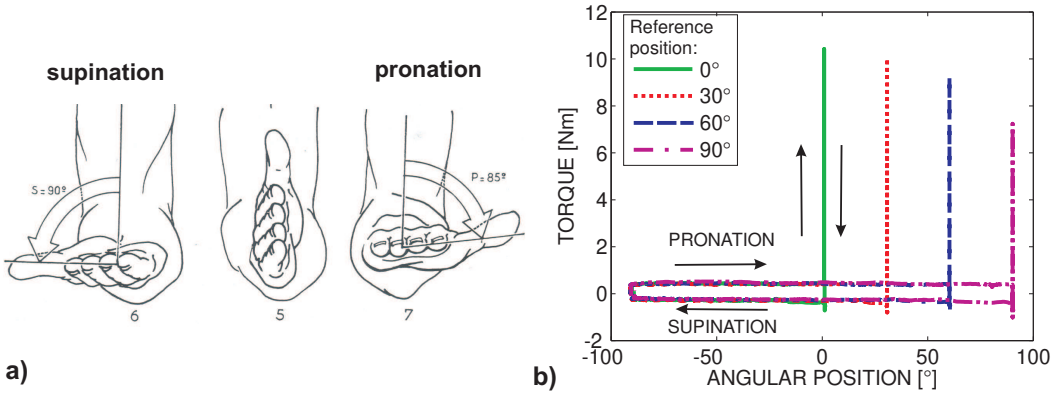

Figure 8.7: a) pronation supination of the wrist, adapted from (Kapandji, 1980) - b) Torque versus position for the isometric mode (pronation)(results obtained with the rehabilitation device)

This controller has also been used to implement end-of-motion stops for the two other exercise modes described below, with a lower stiffness, however, to progressively decelerate the patient motion. Figure 8.8 shows the ability of the system to represent various stiffness values. Experimental and simulated curves are in good agreement.

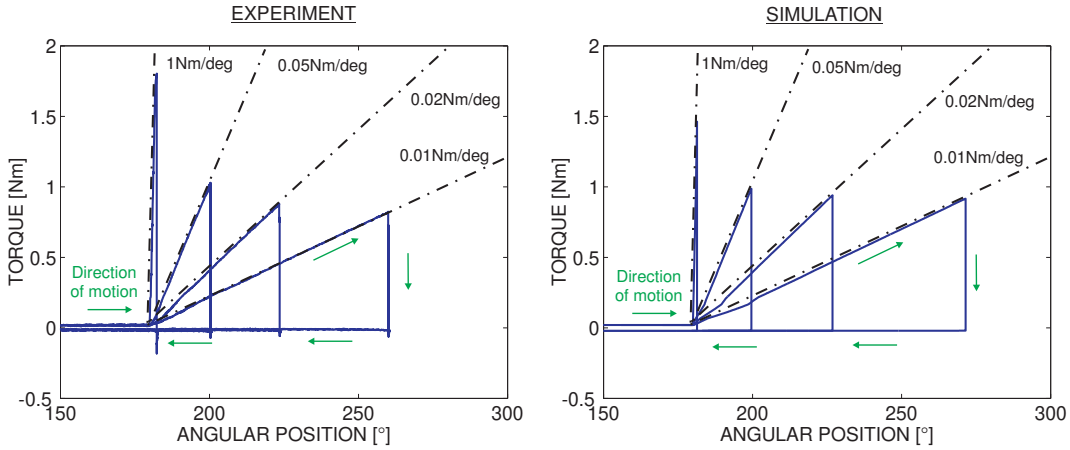

Figure 8.8: Ability of the brake to implement various stiffness (experimental results were obtained on the test bench)

8.4.2 Isotonic control

The isotonic exercise requires to provide the torque controller with the appropriate torque reference as a function of position; it may be either constant, linear or parabolic. Figure 8.9 shows the ability of the MR-brake to provide such torque profiles. Results obtained on both test bench and simulator (with a constant motor speed of 360°/s) are in good agreement.

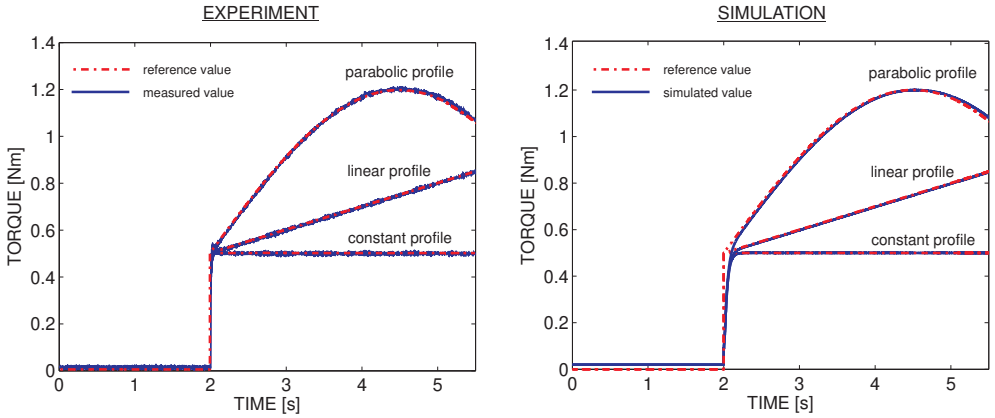

Figure 8.9: Ability of the brake controller to implement various torque profiles: constant linear and parabolic (experimental results obtained on the test bench)

Figure 8.10 shows the results obtained with the same controller implemented on the rehabilitation device. Parabolic and constant reference torque profiles have been applied to the pronation and supination motions respectively. Figure 8.10a) shows the measured torque as a function of angular position. A nearly perfect match between measured and reference torque can be observed. The only deviation is due to the minimum off-state torque of the MR-fluid brake (0.5Nm), which corresponds to the remaining friction after elimination of the remanent magnetic field in the brake. Some peaks in the torque can also be noticed, due to the hard contact implemented when the end-of-motion stops are reached. Figure 8.10b) shows the results of the same experiment for various values of the maximum reference torque (2, 4, 6Nm). A perfect behavior can be observed.

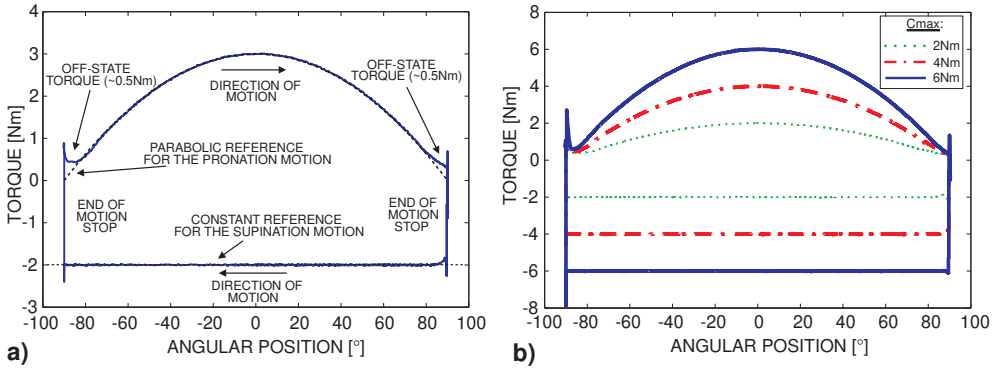

Figure 8.10: Torque versus position curves for the isotonic mode (pronation: parabolic reference - supination: constant reference) (experimental results of the rehabilitation device)

8.4.3 Isokinetic control

For this exercise mode, the control is based on a speed controller that provides a reference torque to the torque loop. A small constant torque (T_0) is also always maintained within the brake. As already mentioned, since the speed of motion is quite low in the application considered here, the quality of the speed signal derived from the encoder measurements is poor and can not be used for control purposes. In order to alleviate this problem, the control is not based on speed but on position measurements that are compared with a reference position signal (consisting of a ramp signal corresponding to a constant speed) (Hisada et al., 2004). The difference between the actual position and the reference signal is used as input of a PID controller (Figure 8.11). Note that the reference position signal only increases when the measured torque is above T_0. When the measured torque is lower than T_0 (i.e.:$speed = 0$), the reference position (θ_{ref}) is reset to the current position ($\theta_{measured}$).

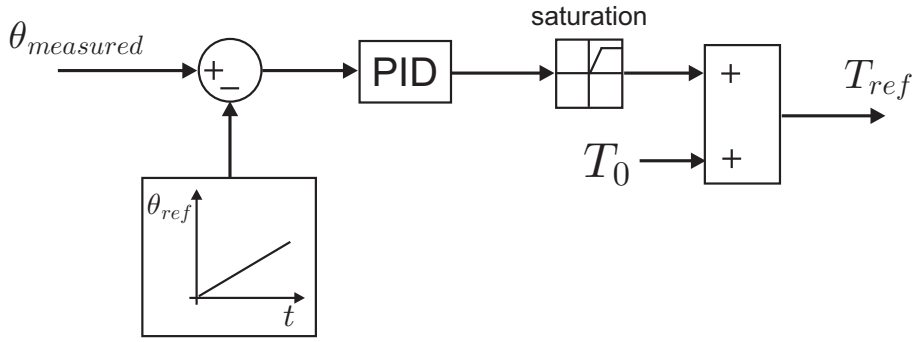

Figure 8.11: Schematic view of the isokinetic controller (results obtained with the rehabilitation device)

This controller has been implemented on the rehabilitation device. Figure 8.12a) shows the evolution of the angular speed as a function of the angular position for various values of the isokinetic reference speed (pronation / supination motion). The corresponding torque applied by the patient is also given (Figure 8.12b). The peak torque tends to decrease with increasing speeds, in accordance with the well known physiological behavior of body joints. It can be seen that despite minor oscillations (that can not be felt by the user), the speed is well maintained at the reference value during the major part of the motion, whatever the torque applied by the patient. A small overshoot can be observed at the beginning of the motion due to the time required by the integral contribution of the controller to act efficiently. After the overshoot, a rise time (increasing with the reference speed) can be observed. It can be explained by limited gain values of the controller selected in order to avoid instabilities in all circumstances. As a consequence, as reported in (Brown and Whitehurst, 2000), the load range (which is the portion of the range of motion where the speed is held constant) decreases when the reference speed increases.

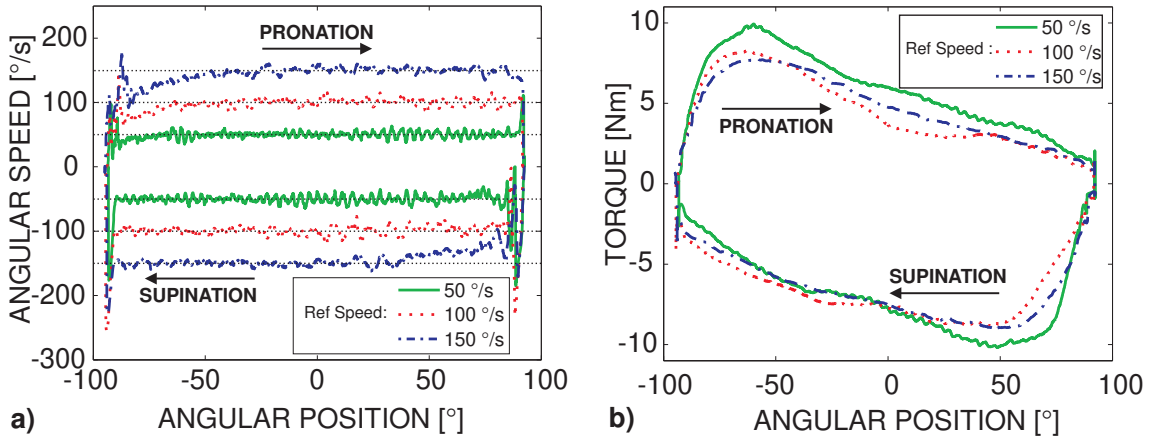

Figure 8.12: Isokinetic mode: a) speed versus position curves for various reference speeds - b) torque versus position curves (results obtained with the rehabilitation device)

8.5 References

J. An and D-G. Kwon. Modeling of a magnetorheological actuator including magnetic hysteresis. *Journal of Intelligent Material Systems and Structures*, 14:541–550, 2003.

K.N. An, L.J. Askew, and E.Y. Chao. *Trends in Ergonomics/Human Factors III*, chapter : Biomechanics and functional assessment of upper extremities. North-Holland: Elsevier Science Publishers, 1986.

L.E. Brown and M. Whitehurst. *Isokinetics in Human Performance*, chapter 5: Load Range, pages 97–121. Human Kinetics, 2000.

S. Dong. *Development and Control of Variable Resistance Exercice Device with Magnetorheological Fluids*. PhD thesis, University of Delaware, 2005.

B. Forthomme, J.L. Croisier, M. Foidart, and J.M. Crielaard. Exploration isocinétique de l'avant-bras et du poignet - méthodologie et application à une pathologie tendineuse. *Journal de Traumatologie du Sport*, 21:80–87, 2004.

T. Hisada, N. Okuyama, S. Komada, and J. Hirai. Preliminary study on robotic exercise therapy. In *Proceedings of the 30th Annual Conference of the IEEE Industrial Electronics Society*, pages 2780–2785, Busan, Korea, 2004.

M.L. Hodgdon. Mathematical theory and calculations of magnetic hysteresis curves. *IEEE Transactions on Magnetics*, 24(6):3120–3122, 1988.

I.A. Kapandji. *Physiologie Articulaire*. Maloine S.A. Editeur, 1980.

B. Liu, W.H. Li, P.B. Kosasih, and X.Z. Zhang. Development of an MR-brake-based haptic device. *Smart Material and Structures*, 15:1960–1966, 2006.

I.D. Mayergoyz. Dynamic preisach models of hysteresis. *IEEE Transactions on Magnetics*, 24(6):2925–2927, 1988.

Chapter 9

Preliminary clinical validation

9.1 Introduction

9.1.1 Test/re-test repeatability analysis

When repeated measurements are done on the same subject using a single instrument (here, our prototype or the CYBEX), the value obtained may substantially vary from one measurement to the other. This is particularly true for biological measurements.

Measurement errors can have various sources: the instrument, the position of the subject, the skill and experience of the observer and even the interaction between the observer and the subject (e.g. the type of instructions given by the observer to the subject...) Some of these factors, such as the error due to the instrument, are outside the control of the observer. Others, such as the position of the subject relatively to the instrument, are not and should thus be standardized for a given measurement.

The natural continual variation of the biological quantity to be measured will also have an impact on measurement error. (Bland, 1995) gives the example of the blood pressure that varies continuously, not only from heart beat to heart beat but from day to day, season to season, and even with the sex of the observer. In the case of measurements of the muscular capabilities of subjects, the quantity measured may vary due to subject fatigue, motivation... (even if no particular muscular training has been performed between two consecutive measurements).

Let's suppose that each subject exhibits, for a given parameter to be measured (e.g. peak torque in isokinetic wrist flexion), a "true" average value over all possible measurements. Due to measurement errors, the measured values will vary around this "true" average value. Various methods and parameters (such as the paired t-test, the correlation coefficient, the within-subject standard deviation...) can be used to quantitatively evaluate the size of the measurement errors and to assess the level of repeatability of a given measurement. More details about these methods and statistical tools can be found in Appendix A.

9.1.2 Analysis of agreement between devices

The problem arising when comparing a new device (here, our prototype) measuring a biological quantity with an old one (here, the CYBEX) is that neither the old nor the new device is giving the "true" value of the quantity to be measured. This is very different from a calibration procedure where known reference quantities can be used to assess the accuracy of the device.

The question to be answered is thus: "Do the two devices agree sufficiently closely so that the new device can replace the old one?".

It should be noticed that the analysis of the level of agreement between devices will be highly influenced by the repeatability of the two devices to be compared. Indeed, as mentioned in (Bland and Altman, 1986), if one device has poor repeatability (i.e. there is considerable variation in repeated measurements on the same subject), the agreement between the two devices is bound to be poor. When the old device is the more variable one, even a new device which is perfect will not agree with it. If both devices have poor repeatability, the problem is even worse. Repeatability analysis has thus to be conducted separately on each device before drawing any conclusion on devices agreement. Most of the methods and statistic tools used for the repeatability analysis can also be used to assess agreement. More details are given in Appendix A.

9.2 Test protocol

The objective of these preliminary tests was to validate the measurements obtained with our prototype in the isokinetic mode by comparing them with the results obtained with a commercial device (CYBEX). This mode was selected for this comparison since it is the most common mode in muscular evaluation and the principal operating mode of the CYBEX. All the tests have been conducted on the wrist joint along its three DOF (pronation/supination, flexion/extension, adduction/abduction). The test subjects were positioned in a similar way on both devices. A custom positioning device was used with the prototype (see section 7.2). The complete list of exercises that have been performed is detailed as follows:

- pronation/supination:	- isokinetic 60°/s	(ROM: $-60°/60°$)
	- isokinetic 90°/s	(ROM: $-60°/60°$)
- flexion/extension:	- isokinetic 60°/s	(ROM: $-45°/45°$)
	- isokinetic 90°/s	(ROM: $-45°/45°$)
- adduction/abduction:	- isokinetic 60°/s	(ROM: $-20°/30°$)
	- isokinetic 90°/s	(ROM: $-20°/30°$)

The comparison between the two machines has been more specifically focused on comparing the repeatability level achieved by each machine between two consecutive measurements and on the agreement of the measurement values obtained with each machine for the same subject.

Measurements have been conducted on 8 healthy right-handed male subjects (age between 21 and 25 years) on both right and left hands. Two measurements have been conducted on each machine, with an interval of at least 20 minutes, allowing the subject to rest between two successive exercises. The aim of conducting measurements on both right and left wrists was to combine these measurements in order to draw conclusions on the repeatability and agreement based on a sample of larger size while limiting the number of subjects to be tested.

Repeatability was measured by using four indicators. Given the small sample size, only indicators not relying on any distribution assumption have been used since the reliability of tests such as the Normality test cannot be guaranteed for small samples. The first indicator was the result of a Wilcoxon matched pairs test (P-value) (see section A.1.4 for more details) where each pair of data was the same measurement obtained during observations 1 and 2. It was combined to a second indicator, the inter-quartile range of the differences (IR), giving an idea of the spread of the differences between the two observations. The third indicator was the within-subject standard deviation (S_w). For completeness, the correlation coefficient (ρ) between measurements obtained with the two observations has also been evaluated although its limitations (detailed in section A.1.2) should be kept in mind. The P-value and ρ should be as close to 1 as possible. Both IR and S_w should be as small as possible.

For the analysis of agreement between our prototype and the CYBEX, as for the repeatability analysis, the first indicator was the result of a Wilcoxon matched pairs test but, here, each pair of data was the same measurement obtained on each machine. In order to avoid misinterpretations, as described in section A.1.4, it was combined to a second indicator, the inter-quartile range of the differences, giving an idea of the spread of the differences between the observations made on each machine. The within-subject standard deviation was also evaluated. However, the correlation coefficient was not used for the agreement analysis for the reasons described in section A.2. Measurements obtained on each machine for the first and second observations could have been compared with each other independently. However, as none of these measurements had to be preferred to the other, the mean of these two measurements were used for comparison.

9.3 Isokinetic mode: analysis of measurement repeatability

9.3.1 Selection of the reference parameter

Most studies of the isokinetic literature are devoted to the analysis of the evolution of the peak torque (Forthomme et al., 2004)(Marley and Thomson, 2000)(Ellenbecker et al., 2006)(Poulis et al., 2003). This measurement is indeed considered to be the most reproductible data that can be obtained while using an isokinetic dynamometer (Croisier and Crielaard, 1999). It is the reason why we focused our analysis on this specific parameter.

9.3.2 Analysis of the results for combined motions

In order to have a global picture of the level of repeatability for the isokinetic exercise and avoid possible misinterpretations due to the small sample size, data collected for all the

different wrist motions (at 60°/s and at 90°/s) have been combined. The results are presented in Table 9.1. P is the probability returned by the Wilcoxon matched pairs test (if $P > 0.05$, there is no sigificative difference between the two observations), IR is the interquartile range of the differences (which should be as small as possible), ρ is the correlation coefficient between the two observations (which should be as close to 1 as possible) and S_w is the within-subject standard deviation (which should be as small as possible).

	ALL ISOKINETIC EXERCISES				
	P	median difference (obs1-obs2) [Nm]	IR [Nm]	ρ	S_w
ULB	0.79	-0.03	1.92	0.92	1.1
CYBEX	0.17	-0.17	2	0.86	1.64

Table 9.1: Repeatability between OBS1 and OBS2 (all motions combined)

These results can also be presented graphically. Figure 9.1 shows, for each machine, a scatter diagram of the second observation as a function of the first one. Figure 9.2 shows a box and wiskers plot of the differences between the two observations on each machine.

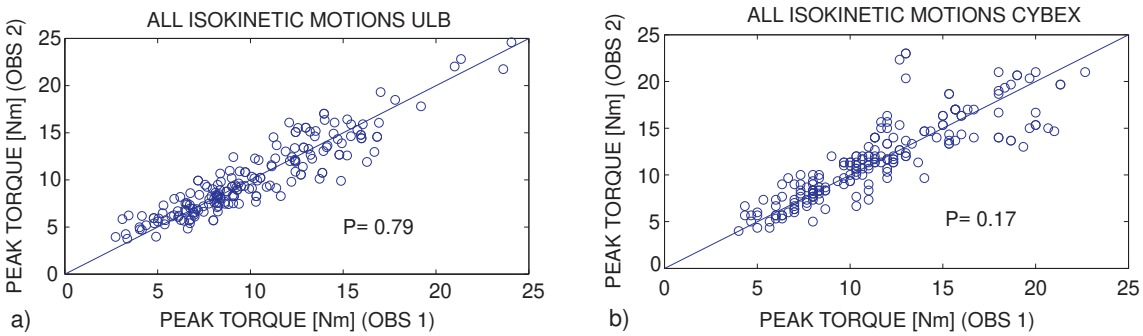

Figure 9.1: Scatter diagram comparing two observations made on the same machine

From Table 9.1, it can be concluded that the repeatability of both machines is very similar. Indeed, the median difference obtained on both machines is very small (the null hypothesis is not rejected by the Wilcoxon test although the P-value is somewhat higher for the ULB prototype) and the inter-quartile range is also similar for both machines. The correlation coefficient is also similar for both machines. Furthermore, from Figures 9.1 and 9.2a), it can be seen that the spread of the differences outside the inter-quartile range is also similar for both machines with, however, a little bit more outliers with the CYBEX device.

Figure 9.2a) and Table 9.1 show that the median difference is around zero. This means that the dispersion of the differences is globally symmetrical around zero. It is however also interesting to have a look at the absolute value of the differences to avoid compensation between data of opposite signs. As can be seen from Figure 9.2b), the results are very similar for both machines, the median absolute difference being around 1Nm with a similar inter-quartile range (25% of the differences lie under 0.4Nm and 75% of the differences lie under 2 Nm).

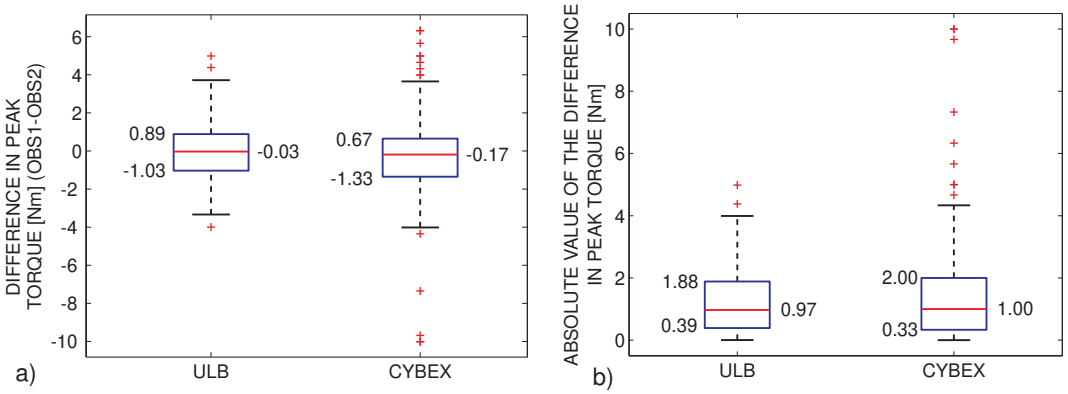

Figure 9.2: Box and wiskers plot for the difference between two observations made on the same machine

9.4 Isokinetic mode: agreement with CYBEX

The objective of this section is to compare the results obtained on both machines in terms of absolute value. As there was no reason to prefer the results obtained for observation 1 over the results obtained for observation 2, we have compared the mean of the two observations obtained on each machine.

9.4.1 Analysis of the results for combined motions

In order to draw generic conclusions for the agreement between machines for the isokinetic mode, we have combined the results obtained for the various wrist motions and the various exercise speeds. The results are presented at Figure 9.3, showing a scatter diagram of the mean observation on the CYBEX as a function of the mean observation on the ULB prototype (for all isokinetic exercises) and a box and wiskers plot of the differences between the two mean observations.

As can be seen from Figure 9.3, there seems to be a bias between the measurements made on the ULB prototype and the ones made on the CYBEX (null hypothesis for the median rejected by the Wilcoxon test and median value of the differences = -1.46Nm). In order to better analyze the source of such a bias, it is worth splitting the results in two categories: motions causing the device axis to move in the anti-clockwise direction (Figure 9.4) and the motions going in the clockwise direction (Figure 9.5). Results are also summarized in Table 9.2.

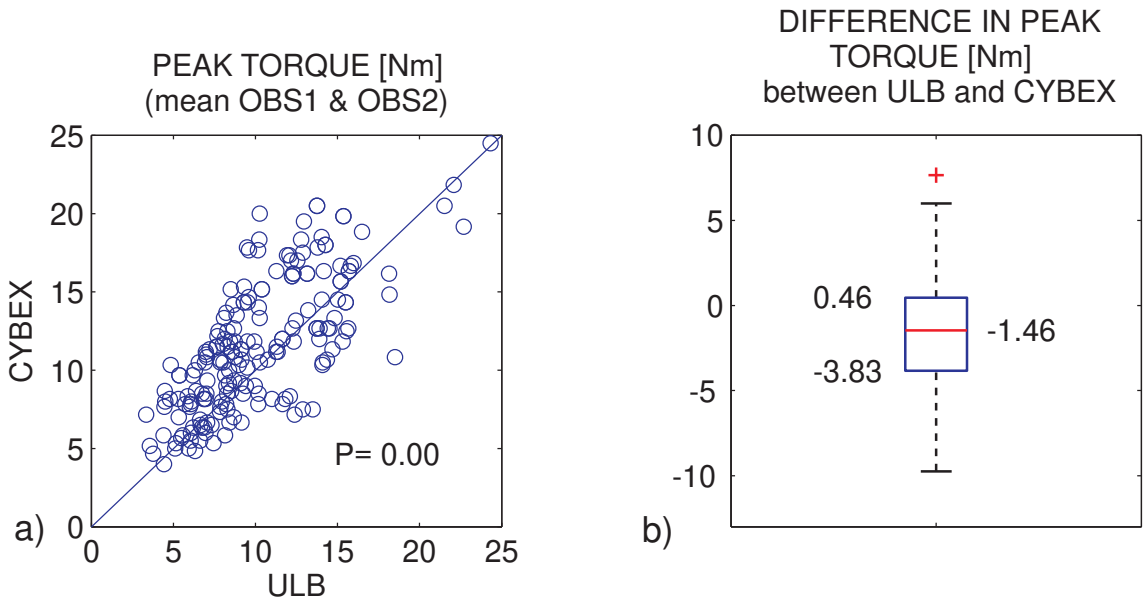

Figure 9.3: a) Scatter plot of peak torque measurements made on ULB prototype and CYBEX - b) Box and wiskers plot of the differences in peak torque between ULB prototype and CYBEX

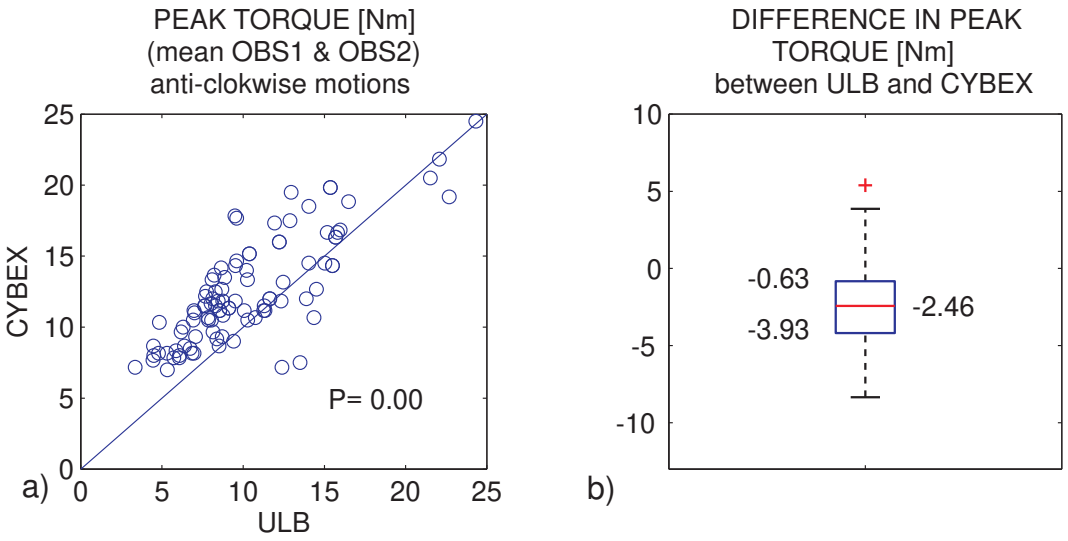

Figure 9.4: a) Scatter plot of peak torque measurements made on ULB prototype and CYBEX - b) Box and wiskers plot of the differences in peak torque between ULB prototype and CYBEX (anti-clockwise motions only)

By comparing Figures 9.4 and 9.5, it is clear that the bias is much larger for the anti-clockwise motions. This bias is negative, meaning that the measurements made on the CYBEX are larger than the one made on the ULB prototype. When looking back at the CYBEX behavior during tests, we noticed that the device that we used had a tendency to move freely in the anti-clockwise direction, sometimes counteracting the effect of gravity, leading to a non-null reading (around 2Nm) for the torque measurement. This might be the cause of the observed

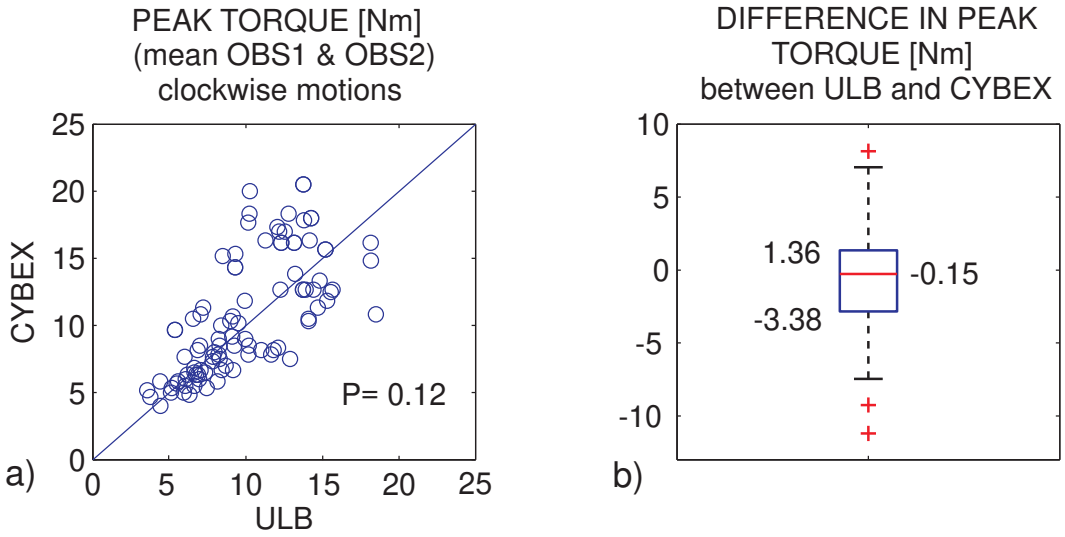

Figure 9.5: a) Scatter plot of peak torque measurements made on ULB prototype and CYBEX - b) Box and wiskers plot of the differences in peak torque between ULB prototype and CYBEX (clockwise motions only)

	all motions	**anti-clockwise motions**	**clockwise motions**
P	0	0	0.12
median difference [Nm]	-1.46	-2.46	-0.15
IR [Nm]	4.29	3.3	4.74
S_w	2.36	2.39	2.33

Table 9.2: Agreement between ULB prototype and CYBEX (all motions combined)

bias. Based on these observations, we have decided to limit the rest of the agreement analysis on the data for the clockwise motion. It is also interesting to note that the spread of the differences remains nearly unaffected whatever the way in which data is combined (look at IR and S_w values in Table 9.2).

For the clockwise motions, the median difference can be considered as null (null hypothesis not rejected by the Wilcoxon test). This means that the dispersion of the differences is globally symmetrical around zero. It is however also interesting to have a look at the absolute value of the differences. As can be seen on Figure 9.6a), the inter-quartile range and the median absolute difference are nearly twice larger than what was observed for the repeatability on each machine separately (see Figure 9.2).

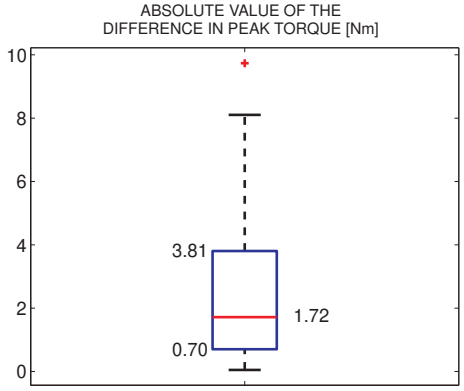

Figure 9.6: a) Box and wiskers plot for the absolute value of the differences between peak torque measurements made on the ULB prototype and the CYBEX (clockwise motions)

9.5 Conclusions of the preliminary clinical tests

By grouping all the results, we have removed the effect of the small sample size on the variability of the data and have shown a good repeatability for both machines (null median) with an inter-quartile range of around 2Nm for both, for the difference between repeated measurements. ρ and S_w values are also similar for both machines.

By looking at all these results, it can be concluded that the level of repeatability is similar for both machines for isokinetic exercises. So, if the CYBEX device is considered by users as being reliable for isokinetic wrist measurements in terms of repeatability, the ULB device should be reliable too.

In order to measure agreement, we have compared mean peak torque measurements obtained with each machine. By grouping the results by motion direction (clockwise and anti-clockwise), we have shown the existence of a bias only for anti-clockwise motions. We attribute the origin of this bias to a drift in the gravity compensation performed by the CYBEX. We have also observed a global inter-quartile range of about 4Nm for the difference between measurements made on both machines. This is twice higher than the IR obtained for repeated measurements.

Given these results we can conclude that the two machines can hardly be used interchangeably for the measurement of peak torque in isokinetic mode but that both might be used in the same way to follow the evolution of patient performances over time since they offer the same repeatability level.

Finally, it should be noticed that all these conclusions are based on measurements made on only 8 subjects. Even if multiple measurements have been combined, this might have an impact on the results. Ideally this clinical validation should have been conducted on a much larger number of subjects and for a larger number of parameters.

9.6 References

J.M. Bland. *An Introduction to Medical Statistics*. Oxford University Press, 1995.

J.M. Bland and D.G. Altman. Statistical methods for assessing agreement between two methods of clinical measurement. *Lancet*, i:307–310, 1986.

J.L. Croisier and J.M. Crielaard. Exploration isocinétique: Analyse des paramètres chiffrés. *Annales de Réadaptation et de Médecine Physique*, 42:538–545, 1999.

T.S. Ellenbecker, E.P. Roetert, and S. Riewald. Isokinetic profile of wrist and forearm strength in elite female junior tennis players. *British Journal of Sports Medicine*, 40:411–414, 2006.

B. Forthomme, J.L. Croisier, M. Foidart, and J.M. Crielaard. Exploration isocinétique de l'avant-bras et du poignet - méthodologie et application à une pathologie tendineuse. *Journal de Traumatologie du Sport*, 21:80–87, 2004.

R.J. Marley and M.R. Thomson. Isokinetic strength characteristics in wrist flexion and extension. *International Journal of Industrial Ergonomics*, 25:633–643, 2000.

S. Poulis, R. Rapanakis, X. Pastra, I. Poulis, and R.W. Soames. Force-velocity relationship of the wrist flexors and extensors: The influense of small and large handgrips. *Isokinetics and exercise science*, 11:101–108, 2003.

Chapter 10

Summary and conclusions

The aim of this thesis is the development of a magneto-rheological (MR) fluid brake and its application to a portable muscular rehabilitation device.

Chapter 2 gives an overview of the composition, the rheological behavior and magnetic properties of MR-fluids. Their various operating modes are also described together with their application within mechatronic devices (dampers, brakes...).

Chapter 3 provides the theoretical background for the design of magnetic circuits with an MR-fluid gap, which are at the heart of any magneto-rheological device.

Based on chapter 3, analytical models of various MR-brake architectures are developed in chapter 4. These relationships enable a quantitative comparison of the major MR-brake designs (drum, inverted drum, disk, multiple disks, T-shaped rotor) based on four figures of merit: dynamic range, torque/volume ratio, rotor radius, electric power consumption.

In order to validate the relationships described in chapter 4, two early MR-brake prototypes (drum and T-shaped rotor) have been built. Their respective performances have been experimentally evaluated and compared on a dedicated test bench. The results of these experiments are extensively reported at chapter 5. Curves such as the hysteretic torque vs current or the torque vs speed characteristics have been obtained for both prototypes and for two different MR-fluids. As expected, the T-shaped rotor brake exhibits a much higher torque than the drum brake for similar dimensions. No significant difference has been observed between the results obtained for both fluids and results are in good agreement with FE simulations. The torque response time has also been evaluated, showing the importance of the material selected for the coil support.

Chapter 6 introduces the fundamentals of muscle biomechanics and wrist kinematics. Methods for muscular evaluation and exercise are also briefly described and compared. The physiological advantages of the isokinetic exercise are highlighted as well as the major drawbacks of existing isokinetic devices: cost, complexity and bulkiness.

Chapter 7 describes the major components of the portable wrist rehabilitation device developed in this work, with particular emphasis on its MR-brake actuator. Following an extensive

market analysis and practitioners advice and requests, this device implements most of the exercise modes that can be found in expensive and bulky multi-function devices, including the isokinetic mode. The control strategies required to implement all these exercise modes are described in chapter 8. The experimental results obtained with both the rehabilitation device and the early MR-brake prototypes show good performances for all exercise modes and are in good agreement with simulations.

Finally, a comparison of our prototype with a commercial device (CYBEX) has been conducted. Results are discussed in chapter 9. For the isokinetic mode, the repeatability level of peak torque measurements is similar for both machines. However, our comparison highlighted a possible drift of the gravity compensation of the CYBEX device.

Original aspects of the work

- A wide range of MR-brake architectures have been quantitatively compared based on the analytical expression of various figures of merit (dynamic range, torque/volume ratio, rotor radius, electric power consumption).

- Various MR-brake prototypes have been built and tested with a specially designed test-bench; their performances have been evaluated with two different MR-fluids.

- A portable rehabilitation device (offering, among others, the isokinetic mode) based on MR-fluid actuation has been designed and manufactured.

- The performances of the prototype of rehabilitation device have been compared with a commercial device (CYBEX) based on measurements conducted on a sample of healthy subjects.

Future work

The work reported in this thesis has led to the development of a portable rehabilitation device specifically designed for small body joints (the wrist, in particular) and ready for an industrial transfer. However, in order to be able to exercise other body joints, a brake delivering higher output torques should be developed, possibly based on the multiple disks architecture in order to keep the compactness of the device unchanged.

A commercial product would require a dedicated electronic board, an improved user interface, and, of course, a redesign of some mechanical parts to allow production by injection molding. Furthermore, a large scale clinical study on patients suffering from muscular disorders should be conducted to confirm the efficiency of the device.

Related publications

The work reported in this thesis has led to the following publications:

Journal papers:

- M. Avraam, M. Horodinca, A. Preumont, MR-Tech: A Portable Smart Wrist Rehabilitation Device, *Journal of Physics: Conference Series* **149**, 2009.

- M. Avraam, M. Horodinca, I. Romanescu and A. Preumont, Computer controlled rotational MR-brake for wrist rehabilitation device, submitted to the *Journal of Intelligent Materials Systems and Structures*, 2009.

Patent application:

- M. Avraam and A. Preumont, Joint rehabilitation device and method, patent number WO 2009/063027, 2008

Conference proceedings:

- M. Avraam, M. Horodinca, P. Letier, A. Preumont, Portable Smart Wrist Rehabilitation Device Driven by Rotational MR-fluid Brake Actuator for Telemedecine Applications, *Proceedings of IEEE IROS 08*, Nice, France, September 2008.

- P. Letier, M. Avraam, M. Horodinca, A. Schiele, A. Preumont, Survey of actuation technologies for body-grounded exoskeletons, *Proceedings of Eurohaptics 2006*, Paris, France, July 2006.

- M. Avraam, P. Letier, M. Horodinca, I. Romanescu, A.Preumont, MR fluid brake prototypes for portable haptic interfaces, *Proceedings of Actuator 2006*, Bremen, Germany, June 2006.

- M. Avraam, P. Letier, I. Romanescu, M. Horodinca, A. Preumont, Exoskeleton haptic device for extravehicular space robotic activities: a survey of actuation technology, *Proceedings of the 15th International Symposium on Measurement and Control in Robotics*, Brussels, Belgium, November 2005.

Appendix A

Statistics for clinical analysis

A.1 Methods for test/re-test repeatability analysis

OBS1	**OBS2**	**OBS1-OBS2**	**VARIANCE**
subject 1: x_1	y_1	$\delta_1 = x_1 - y_1$	$\sigma_1^2 = \frac{1}{2}(x_1 - y_1)^2$
subject 2: x_2	y_2	$\delta_2 = x_2 - y_2$	$\sigma_2^2 = \frac{1}{2}(x_2 - y_2)^2$
$\vdots$	$\vdots$	$\vdots$	$\vdots$
subject i: x_i	y_i	$\delta_i = x_i - y_i$	$\sigma_i^2 = \frac{1}{2}(x_i - y_i)^2$
$\vdots$	$\vdots$	$\vdots$	$\vdots$
subject n: x_n	y_n	$\delta_n = x_n - y_n$	$\sigma_n^2 = \frac{1}{2}(x_n - y_n)^2$
$\bar{x} = \frac{1}{n}\sum_{i=1}^{n} x_i$	$\bar{y} = \frac{1}{n}\sum_{i=1}^{n} y_i$	$\bar{\delta} = \frac{1}{n}\sum_{i=1}^{n} \delta_i$	
$\sigma_x^2 = \frac{1}{n-1}\sum_{i=1}^{n}(x_i - \bar{x})^2$	$\sigma_y^2 = \frac{1}{n-1}\sum_{i=1}^{n}(y_i - \bar{y})^2$	$s^2 = \frac{1}{n-1}\sum_{i=1}^{n}(\delta_i - \bar{\delta})^2$	$S_w = \sqrt{(\frac{1}{n})\sum_{i=1}^{n}\sigma_i^2}$

Table A.1: Measured data (x_i and y_i) for a sample of n subjects, during two observations of the same variable (OBS1 and OBS2), and associated values (difference, mean and variance)

A.1.1 Paired t-test

At least two observations have to be taken for a given subject in order to assess the repeatability of a given measurement. A common experiment design in clinical studies is to take only two observations per subject, but for a sample of n subjects (typically $n = 20$ for preliminary studies).

The most obvious test to assess repeatability is to compute the mean difference between the first and second measurement over the whole sample of subjects ($\bar{\delta}$). If this mean difference may be considered as null, it gives a first hint on the repeatability of the measurement. The

objective of the *t-test* is thus to test the null hypothesis that the **mean** difference is zero. If the data are not consistent with the null hypothesis, the difference between the first and the second measurement is said to be *statistically significant*. The t-test is based on the evaluation of the following ratio for the given sample:

$$\frac{\left(\bar{\delta}-\mu\right)}{\sqrt{\frac{s^2}{n}}} \tag{A.1}$$

where $\bar{\delta}$ is the mean difference of the sample, μ is the mean of the whole population of differences (considered as null, cf. hypothesis), s^2 is the sample variance and n is the sample size (Table A.1). *If the differences are normally distributed*, it can be shown that ratio (A.1) follows a *Student t* distribution with $n-1$ degrees of freedom (dof) (Bland, 1995) (Figure A.1a). For a given value of the ratio, the corresponding probability (called P-value) can thus be computed. It corresponds to the probability to obtain this ratio under the null hypothesis. If this probability is lower than 0.05, the mean difference is considered as being different from zero (the null hypothesis is said to be rejected at the statistical significance level of 0.05). For example, if $n = 6$ (5dof), the difference between the 1st and 2nd measurement is statistically significant, at the 0.05 level, if the ratio (A.1) is higher than 2.57 (Figure A.1b). This limit should however be considered as a guideline and not as an absolute limit.

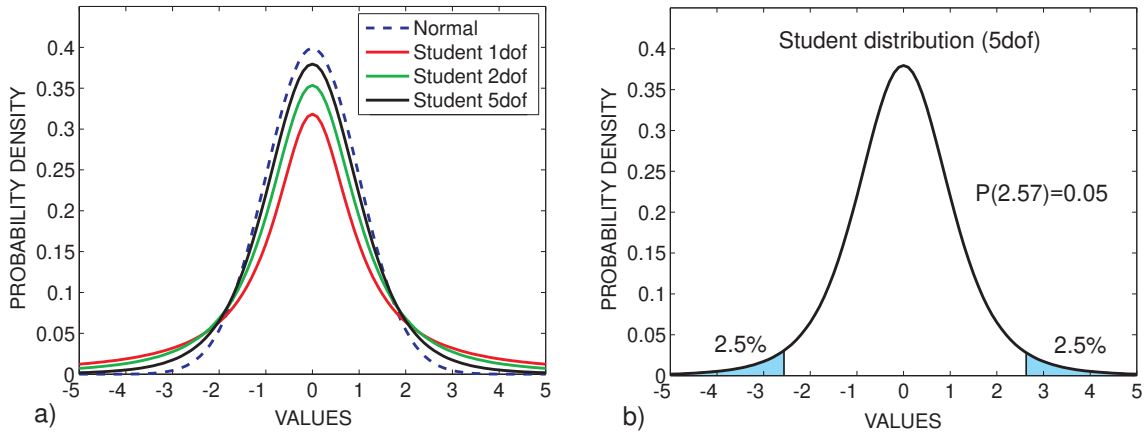

Figure A.1: a)Probability density of the Normal and Student distributions - b) 5% point of the Student distribution with 5 degrees of freedom

Together with the hypothesis of normality for the data, another major drawback of the t-test should also be pointed out: a broad range of variability for the readings of each observation results in widely dispersed distributions (large s^2) and may contribute to the acceptance of the null hypothesis. So, by this criterion, the greater the measurement error, and hence the less chance of a significant difference, the better!

A.1.2 Correlation coefficient

The common experiment design used to assess the repeatability of a measurement usually comprising two observations per subject, it seems appropriate to calculate a correlation coef-

ficient (ρ) between first and second measurement:

$$\rho = \frac{1}{n}\sum_{i=1}^{n}\left(\frac{x_i - \overline{x}}{\sigma_x}\right).\left(\frac{y_i - \overline{y}}{\sigma_y}\right) \tag{A.2}$$

where x_i and y_i are the measurements for the first and second observation for the i^{th} subject, $\overline{x}$ and $\overline{y}$ the mean measurement of first and second observation, σ_x and σ_y the standard deviation of first and second observation (Table A.1). The closer ρ is to 1, the highest is the correlation between the first and second measurement.

However, as illustrated in (Bland and Altman, 1996), this correlation coefficient will depend on the variability between subjects. Samples containing subjects who differ greatly will produce larger correlation coefficients than samples containing similar subjects. This method should thus only be used if the sample is representative of the whole population of possible subjects.

Furthermore, the correlation coefficient is sensitive to the order between first and second observation. Indeed, if this order is reversed for some of the subjects, the correlation coefficient will differ. This is not acceptable as first and second observations are repeated observations of the same thing. A solution to this later problem is to make use of the *intra-class correlation coefficient* (ICC) that estimates the average correlation among all possible orderings of pairs (Bland and Altman, 1996). However, the ICC is still influenced by the variability of the measurements (Bland and Altman, 1990), a property that makes it difficult to compare between studies (Rothwell, 2000).

A.1.3 Within-subject standard deviation and repeatability coefficient

Another tool to assess measurement repeatability is the within-subject standard deviation (S_w), which is assumed to be the same for all subjects. S_w is obtained by first calculating, for each subject (i), the variance between first and second measurement (σ_i^2), then the mean of these values, called the within-subject variance (S_w^2). S_w is the square-root of this value (Table A.1). The smaller S_w is, the better the repeatability is.

It is important to note that the statement that the standard deviation is the same for all subjects is based on the underlying assumption that the measurement error is independent of the size of the measurement. This assumption should be checked either graphically (by plotting the subject's standard deviations against their means) or analytically by calculating the correlation coefficient between the standard deviations and the means.

Another way to present the size of the measurement error is the repeatability coefficient, defined by the British Standard Institution as the value below which the difference between two measurements will lie with a probability of 95%. *If the measurement errors are from a Normal distribution*, it can be estimated by: $1.96\sqrt{2S_w^2} = 2.77\ S_w$.

A.1.4 Wilcoxon matched pairs test / Box and wiskers plot

As previously highlighted, the t-test and the BSI coefficient of repeatability are based on the assumption that the distribution of the differences (between two observations) come from a Normal distribution. These methods are called *parametric*. Before applying them, it is then required to test the hypothesis of normality.

However, experimental data are not always normally distributed and sometimes, due to the small sample size for example, it can also be difficult to assess the normality of the data. In this case, it is, of course, always possible to make the hypothesis of normality but this approach is not very rigorous. An alternative approach is to make use of *non-parametric methods* which do not assume any particular family of distribution for the data. The Wilcoxon matched pairs test is one of them.

This test is an analog of the paired t-test but makes use of the rank order of the data instead of relying on the Student distribution. The objective of this test is to check the null-hypothesis stating that *the difference between the members of each pair of data* (in our case two successive observations for the same subject, δ_i) *has a* ***median*** *value of zero*. It is interesting to note that, for small samples, testing the median instead of the mean is more efficient as it is less sensitive to outliers.

The Wilcoxon test works in the following way. The differences δ_i are ranked by their absolute value. Tied observations are given the average of their ranks. Ranks of positive and negative differences are summed separately. If the null hypothesis was true and there was no difference between the two data sets, one would expect that the rank sums for positive and negative differences to be about the same. The test statistics is the lesser of theses sums, T. The test will return the probability (P) to obtain the observed value of T if the null hypothesis were true. If this probability is lower than a given significance level (usually 5%), the null hypothesis can be rejected (for more details, refer to (Bland, 1995)).

It is important to note that this test enables to identify any bias between the two data sets. However, if the differences between the data sets are equally distributed (in sign and magnitude) on each side of the equality line, the test will still conclude to a null median difference which could be misleading if used alone to assess the repeatability of a given method. Moreover the Wilcoxon test does not tell anything about the size of the difference, only its existence.

It is thus interesting to combine this test with a plot that will give an idea of the distribution of the differences. The box and whisker plot (Figure A.2) can be used for that purpose. The box shows the distance between the lower and upper quartiles (50% of the observations lie within the box), with the median marked as a line, and the 'whiskers' show the most extreme values that lie within *limit of the box+1.5 IR*. Values that are larger than *limit of the box+1.5 IR* the interquartile range are considered as outliers and are displayed with a '+' sign.

A.1.5 Scatter plot

Another way to represent the data is to plot, for each subject, the results of the second observation (OBS2) against those of the first (OBS1). This plot should also include the line of

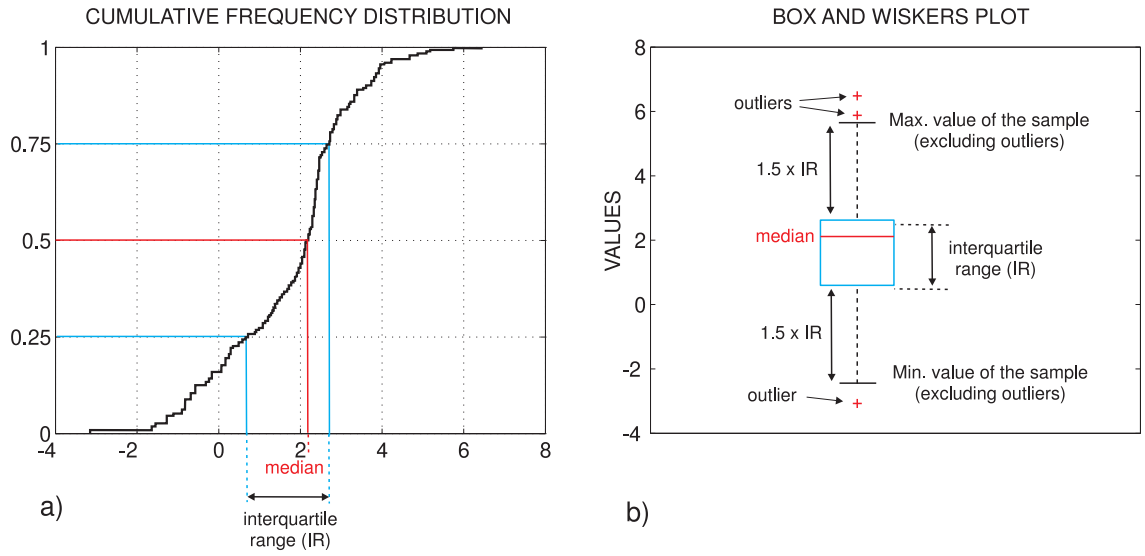

Figure A.2: a) Cumulative frequency distribution with the corresponding median and interquartile range - b) Corresponding Box and Wiskers plot

identity (where OBS1=OBS2) to enable a first visual assessment of the relationship between measurements obtained during both observations (Figure A.3). The closest to the identity line the points cluster, the best repeatability level is achieved. It should be noticed that, very often, this kind of plot has a regression line drawn through the data, which has much less significance in terms of repeatability evaluation than the line of identity.

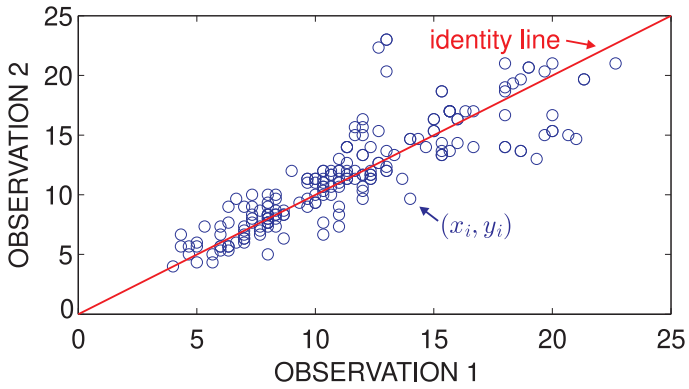

Figure A.3: Example of data plot of Observation 2 against Observation 1

A.2 Methods for agreement analysis

Most methods and tools described above for the repeatability analysis also apply to the agreement analysis between two machines. The only difference is that instead of comparing two measurements obtained during two successive observations (OBS1 and OBS2) on the same machine, the comparison is made between two measurements obtained on each machine. The

correlation coefficient (ρ) alone cannot be used to measure agreement. Indeed, as stressed in (Bland and Altman, 1986), the correlation coefficient (ρ) measures the strength of association between two variables and not the agreement between them. Perfect agreement means that one measurement equals the other. For instance, if one measurement consistently doubles the other, the two measurements will be perfectly correlated but will not agree at all.

Moreover, as mathematically demonstrated in (Altman and Bland, 1983), the correlation coefficient depends on both the variation between individuals (i.e. between the true values) and the variation within individuals (measurement error). Indeed, if the variation between individuals is high compared to the measurement error, the correlation will be high, and if the variation between individuals is low, the correlation will be low. This property of the correlation coefficient can be very misleading. Since investigators usually try to compare two methods over the whole range of values typically encountered, a high correlation coefficient is almost guaranteed. Data which seems to be in poor agreement can thus produce quite high correlations.

An illustration of this phenomenon is given by the two samples of Table A.2 (Bland and Altman, 1990). For both samples, the differences between method A and B are the same for all subjects. From these results, the conclusion about the agreement between method A and B should be the same for both samples. However, the subject variability of sample 1 is much lower than that of sample 2, leading to a much lower correlation coefficient (sample 1: ρ=0.17, sample 2: ρ=0.99). By observing only the correlation coefficient of sample 1, one may thus conclude that method A and B poorly agree and by observing only the correlation coefficient of sample 2, the agreement seems nearly perfect, despite the fact that the differences between methods A and B are the same for both samples!

SAMPLE 1				SAMPLE 2			
	Method				Method		
subject	A	B	A-B	subject	A	B	A-B
1	90	95	-5	1	120	125	-5
2	95	90	5	2	95	90	5
3	90	90	0	3	80	80	0
4	95	95	0	4	75	75	0
5	90	90	0	5	70	70	0
ρ=0.17				ρ=0.99			

Table A.2: Example of the calculation of ρ between methods A and B for two samples with different subject variability but similar differences between methods

A.3 References

D.G. Altman and J.M. Bland. Measurement in medicine: The analysis of method comparison studies. *The Statistician*, 32(3):307–317, 1983.

J.M. Bland. *An Introduction to Medical Statistics*. Oxford University Press, 1995.

J.M. Bland and D. G. Altman. Statistics notes: Measurement error. *British Medical Journal*, 312:1654, 1996.

J.M. Bland and D.G. Altman. Statistical methods for assessing agreement between two methods of clinical measurement. *Lancet*, i:307–310, 1986.

J.M. Bland and D.G. Altman. A note on the use of intraclass correlation coefficient in the evaluation of agreement between two methods of measurement. *Computers in Biology and Medecine*, 20(5):337–340, 1990.

P.M. Rothwell. Analysis of agreement between measurement of continuous variables: General principles and lessons from studies of imaging of carotid stenosis. *Journal of Neurology*, 415:825–834, 2000.

Appendix B

Patent application

(12) INTERNATIONAL APPLICATION PUBLISHED UNDER THE PATENT COOPERATION TREATY (PCT)

(19) World Intellectual Property Organization
International Bureau

(43) International Publication Date
22 May 2009 (22.05.2009)

PCT

(10) International Publication Number
WO 2009/063027 A1

(51) International Patent Classification:
A61H 1/02 (2006.01) *A63B 23/14* (2006.01)
A63B 21/005 (2006.01) *A63B 23/16* (2006.01)
A63B 23/04 (2006.01) *A63B 24/00* (2006.01)
A63B 23/08 (2006.01) *G06F 1/16* (2006.01)

(21) International Application Number:
PCT/EP2008/065509

(22) International Filing Date:
13 November 2008 (13.11.2008)

(25) Filing Language: English

(26) Publication Language: English

(30) Priority Data:
07120616.3 13 November 2007 (13.11.2007) EP
07120730.2 14 November 2007 (14.11.2007) EP
08151136.2 6 February 2008 (06.02.2008) EP

(71) Applicant *(for all designated States except US)*: **UNIVERSITE LIBRE DE BRUXELLES** [BE/BE]; Avenue Franklin Roosevelt 50 CP 161, B-1050 Bruxelles (BE).

(72) Inventors; and
(75) Inventors/Applicants *(for US only)*: **PREUMONT, André** [BE/BE]; Rue du centre 6, B-1450 Chastre (BE). **AVRAAM, More** [BE/BE]; Rue des glaïeuls 37, B-1180 Bruxelles (BE).

(74) Agent: **PRONOVEM - Office Van Malderen**; Avenue Josse Goffin 158, 100762565, B-1082 Bruxelles (BE).

(81) Designated States *(unless otherwise indicated, for every kind of national protection available)*: AE, AG, AL, AM, AO, AT, AU, AZ, BA, BB, BG, BH, BR, BW, BY, BZ, CA, CH, CN, CO, CR, CU, CZ, DE, DK, DM, DO, DZ, EC, EE, EG, ES, FI, GB, GD, GE, GH, GM, GT, HN, HR, HU, ID, IL, IN, IS, JP, KE, KG, KM, KN, KP, KR, KZ, LA, LC, LK, LR, LS, LT, LU, LY, MA, MD, ME, MG, MK, MN, MW, MX, MY, MZ, NA, NG, NI, NO, NZ, OM, PG, PH, PL, PT, RO, RS, RU, SC, SD, SE, SG, SK, SL, SM, ST, SV, SY, TJ, TM, TN, TR, TT, TZ, UA, UG, US, UZ, VC, VN, ZA, ZM, ZW.

(84) Designated States *(unless otherwise indicated, for every kind of regional protection available)*: ARIPO (BW, GH, GM, KE, LS, MW, MZ, NA, SD, SL, SZ, TZ, UG, ZM, ZW), Eurasian (AM, AZ, BY, KG, KZ, MD, RU, TJ, TM), European (AT, BE, BG, CH, CY, CZ, DE, DK, EE, ES, FI, FR, GB, GR, HR, HU, IE, IS, IT, LT, LU, LV, MC, MT, NL, NO, PL, PT, RO, SE, SI, SK, TR), OAPI (BF, BJ, CF, CG, CI, CM, GA, GN, GQ, GW, ML, MR, NE, SN, TD, TG).

Published:
— *with international search report*
— *before the expiration of the time limit for amending the claims and to be republished in the event of receipt of amendments*

(54) **Title:** JOINT REHABILITATION DEVICE AND METHOD

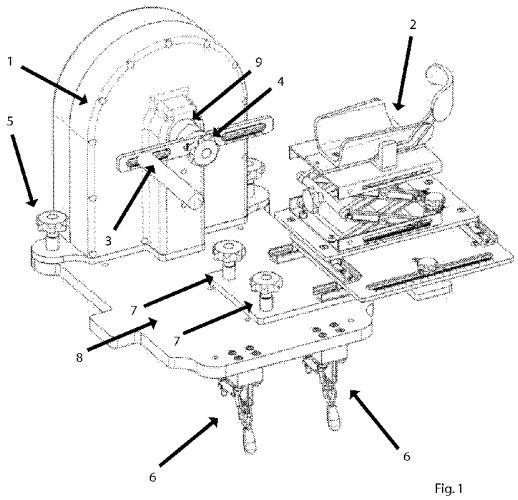

Fig. 1

(57) **Abstract:** A device for exercise rehabilitation and evaluation of a joint between bone elements of the hand, of the arm or of the leg of a user comprising at least : - a portable housing (1), - magnetically controllable resistance means (10,11,13), - a rotable output shaft (9), - control means (18), - tool means (40, 41) gripable by or attached to the user, said tool means being in direct connection with the rotable output shaft extending out of the housing, - mechanical positioning means (20, 21, 22) adapted to user's morphology that enable to position the joint at a pre-determined position (x,y,z) regarding a three dimensional reference system attached to the housing, - mechanical constraint means (30,31) for blocking at least one bone element of the hand, the arm, or the leg at said position while at least one degree of freedom is given to the joint.

WO 2009/063027 A1

General Bibliography

B. Ackermann and R. Elferich. Application of magnetorheological fluids in programmable haptic knobs. In *Proceedings of Actuator 2000*, Bremen, Gremany, 2000.

D.G. Altman and J.M. Bland. Measurement in medicine: The analysis of method comparison studies. *The Statistician*, 32(3):307–317, 1983.

J. An and D-G. Kwon. Modeling of a magnetorheological actuator including magnetic hysteresis. *Journal of Intelligent Material Systems and Structures*, 14:541–550, 2003.

J. An and D-S. Kwon. Haptic experimentation on a hybrid Active/Passive force feedback device. In *Proceedings of the IEEE International Conference on Robotics and Automation*, pages 4217–4222, Washington DC, 2002.

K.N. An, L.J. Askew, and E.Y. Chao. *Trends in Ergonomics/Human Factors III*, chapter : Biomechanics and functional assessment of upper extremities. North-Holland: Elsevier Science Publishers, 1986.

ANAES. Les appareils d'isocinétisme en évaluation et rééducation musculaire: Intérêt et utilisation. 2001.

M. Avraam, P. Letier, I. Romanescu, M. Horodinca, and A. Preumont. Exoskeleton haptic device for extravehicular space robotic activities: A survey of actuation technology. In *Proceedings of the 15th International Symposium on Measurment and Control in Robotics*, Brussels, Belgium, 2005.

A. Baker. Brake cuts exercise-equipment cost. *Design news*, 1995.

D.E. Barber and J.D. Carlson. Performance characteristics of prototype MR engine mounts containing LORD glycol MR fluids. In *Proceedings of ERMR'08*, Dresden, Germany, 2008.

BASF. Product datasheet: Carbonyl iron powders. 2006.

L. Biedermann. Leg prosthesis with an artificial knee joint provided with adjustment device. US patent 6,423,098, 2002.

L. Biedermann, W. Matthis, and C. Schulz. Leg prosthesis with an artificial knee joint and method for controlling a leg prosthesis. US patent 6,755,870, 2004.

T. Black and J.D. Carlson. *Synthetic, Mineral Oils and Bio-Based Lubricants*, chapter 35: Magnetizable Fluids, pages 565–583. Taylor and Francis, 2006.

J.M. Bland. *An Introduction to Medical Statistics*. Oxford University Press, 1995.

J.M. Bland and D. G. Altman. Statistics notes: Measurement error. *British Medical Journal*, 312:1654, 1996.

J.M. Bland and D.G. Altman. Statistical methods for assessing agreement between two methods of clinical measurement. *Lancet*, i:307–310, 1986.

J.M. Bland and D.G. Altman. A note on the use of intraclass correlation coefficient in the evaluation of agreement between two methods of measurement. *Computers in Biology and Medecine*, 20(5):337–340, 1990.

R. Bölter and H. Janocha. Design rules for MR-fluid actuators in different working modes. In *Proccedings of SPIE Smart Structures and Materials 1997*, pages 148–159, San Diego, California, 1997.

H. Böse, A. Trendler, A. Kramlich, and J. Ehrlich. A haptic knob with different magnetorheological fluids. In *Proceedings of Actuator 2006*, pages 245–248, Bremen, 2006.

L.E. Brown and M. Whitehurst. *Isokinetics in Human Performance*, chapter 5: Load Range, pages 97–121. Human Kinetics, 2000.

P. Campbell. *Permanent Magnet Materials and their Application*. Cambridge university press, 1994.

J.D. Carlson. Portable hand and wrist rehabilitation device. US patent 6,117,093, 2000.

J.D. Carlson. Magnetorheological brake with integrated flywheel. US patent 6,186,290, 2001a.

J.D. Carlson. What makes a good MR-fluid? In *Proceedings of the 8th ERMR Conference*, pages 63–69, Nice, France, 2001b.

J.D. Carlson. What makes a good MR fluid. *Journal of Intelligent Material Systems and Structures*, 13:431–435, 2003.

J.D. Carlson. Semi-active vibration supression. In *CISM Course: Semi-Active Vibration Suppression - the Best from Active and Passive Technologies*, Udine, October 2007.

J.D. Carlson. *Smart Materials*, chapter 17: Magnetorheological Fluids, pages 17.1–17.8. CRC Press, 2009.

J.D. Carlson. Multi-degree of freedom magnetorheological devices and system for using same. US patent 5,492,312, 1996.

J.D. Carlson. Portable magnetically controllable fluid rehabilitation devices. World patent WO 97/33658, 1997.

J.D. Carlson and A.R. Johnson. Electro-rheological and magnetorheological fluids: A state-of-the-art report. In *Proceedings of Actuator'04*, Bremen, Germany, 2004.

J.D. Carlson and M.R. Jolly. MR fluid, foam and elastomer devices. *Mechatronics*, 10: 555–569, 2000.

J.D. Carlson and J.L. Sproston. Controllable fluids in 2000 - status of ER and MR fluid technology. In *Proceedings of Actuator'00*, Bremen, Germany, 2000.

J.D. Carlson, D.F. LeRoy, J.C. Holzheimer, D.R. Prindle, and R.H. Marjoram. Controllable brake. US patent 5,842,547, 1998.

K-M. Chan and N. Maffulli. *Principles and Practice of Isokinetics in Sports Medecine and Rehabilitation*. Williams and Wilkins, Hong-Kong, 1996.

B.D. Chin, J.H. Park, M.H. Kwon, and O.O. Park. Rheological properties and dispersion stability of magnetorheological (MR) suspensions. *Rheologica Acta*, 40:211–219, 2001.

S-B Choi, S-R Hong, C-C Cheong, and Y-K Park. Comparison of field-controlled characteristics between ER and MR clutches. *Journal of Intelligent Material Systems and Structures*, 10:615–619, 1999.

J.L. Croisier and J.M. Crielaard. Exploration isocinétique: Analyse des paramètres chiffrés. *Annales de Réadaptation et de Médecine Physique*, 42:538–545, 1999a.

J.L. Croisier and J.M. Crielaard. Methodes d'exploration de la force musculaire: Une analyse critique. *Annales de Réadaptation et de Médecine Physique*, 42:311–322, 1999b.

B.W. Deffenbaugh, H.M. Herr G.A. Pratt, and M.B. Wittig. Electronically controlled prosthetic knee. US patent application 2001/0029400, 2001.

T.L. Delorme. *Progressive Resistance Exercise*. Appleton-Century-Crofts, New York, 1951.

S. Dong. *Development and Control of Variable Resistance Exercice Device with Magnetorheological Fluids*. PhD thesis, University of Delaware, 2005.

S. Dong, K-Q. Lu, J.Q. Sun, and K. Rudolph. Rehabilitation device with variable resistance and intelligent control. *Medical Engineering and Physics*, 27:249–255, 2005.

V. Dwivedi, G.V. Strikis, J.M. Ginder, L.D. Ellie, S.A. Harte, and K. Bhatia. Magnetic powder clutch. US patent 6,394,244, 2002.

J. A. Edminister. *Schaum's Outline of Theory and Problems of Electromagnetics (2nd Edition)*. McGraw-Hill, 1993.

T.S. Ellenbecker, E.P. Roetert, and S. Riewald. Isokinetic profile of wrist and forearm strength in elite female junior tennis players. *British Journal of Sports Medicine*, 40:411–414, 2006.

R.T. Foister. Magnetorheological fluids. US patent 5,667,715, 1997.

B. Forthomme, J.L. Croisier, M. Foidart, and J.M. Crielaard. Exploration isocinétique de l'avant-bras et du poignet - méthodologie et application à une pathologie tendineuse. *Journal de Traumatologie du Sport*, 21:80–87, 2004.

Frost and Sullivan. US rehabilitation equipment markets: Market study, 1998.

J. Furusho, T. Kikuchi, M. Tokuda, T. Kakehashi, K. Ikeda, S. Morimoto, Y. Hashimoto, H. Tomiyama, A. Nakagawa, and Y. Akazawa. Development of a shear type compact MR brake for the intelligent ankle-foot orthosis and its control. In *Proceedings of the 2007 IEE 10th International Conference on Rehabilitation and Robotics*, pages 89–94, Noordwijk, The Netherlands, 2007.

D.R. Gamota and F.E. Filisko. Dynamic mechanical studies of electrorheological materials: Moderate frequencies. *Journal of Rheology*, 35:399–425, 1991.

F. Gandhi and W.A. Bullough. On the phenomenological modeling of electrorheological and magnetorheological fluid preyield behavior. *Journal of Intelligent Material Systems and Structures*, 16:237–248, 2005.

S. Genç. *Synthesis and Properties of Magnetorheological (MR) Fluids*. PhD thesis, University of Pittsburg, 2002.

J.M. Ginder, L.C. Davis, and L.D. Elie. Rheology of magnetorheological fluids: Models and measurements. *International Journal of Modern Physics B*, 10:3293–3303, 1996.

M.A. Golden, J.C. Ulicny, K.S. Snavely, and A.L. Smith. Magnetorheological fluids. US patent 6,932,917, 2005.

F.D. Goncalves and J.D. Carlson. An alternate operation mode for MR-fluids - magnetic gradient pinch. In *Proceedings of the 11th ERMR Conference*, Dresden, Germany, 2008.

F.D. Goncalves, J-H. Koo, and M. Ahmadian. A review of the state of the art in magnetorheological fluid technologies - part i: MR fluid and MR fluid models. *The Shock and Vibration digest*, 38:203–219, 2006.

S. Gopalswamy and G.L. Jones. Magnetorheological transmission clutch. US patent 5,823,309, 1998.

N. Gstöttenbauer. *Magneto-Rheological Fluids in Squeeze Mode*. PhD thesis, Johannes Kepler University of Linz, 2008.

K.H. Gudmundsson, F. Jonsdottir, H. Palsson, and S.G. Karlsson. Optimization a magnetorheological rotary brake. In *Proceedings of 3rd ECCOMAS Thematic Conference on Smart Structures and Materials*, Gdansk, Poland, 2007.

M. Handel, H.H. Dickhuth, F. Mayer, and R.W. Gülch. Prerequiste and limitations to isokinetic measurements in humans. *European Journal of Applied Physiology*, 73:225–230, 1996.

A.V. Hill. The heat of shortening and the dynamic constants of muscle. *Proceedings of the Royal Society*, B126:136–195, 1938.

T. Hisada, N. Okuyama, S. Komada, and J. Hirai. Preliminary study on robotic exercise therapy. In *Proceedings of the 30th Annual Conference of the IEEE Industrial Electronics Society*, pages 2780–2785, Busan, Korea, 2004.

H. Hislop and I. Perrine. The isokinetic concept of exercise. *Physical Therapy*, 47:114–117, 1967.

M.L. Hodgdon. Mathematical theory and calculations of magnetic hysteresis curves. *IEEE Transactions on Magnetics*, 24(6):3120–3122, 1988.

J. Huang, J.Q. Zhang, Y. Yang, and Y.Q. Wei. Analysis and design of a cylindrical magnetorheological fluid brake. *Journal of Materials Processing Technology*, 129:559–562, 2002.

M.R. Jolly and J.D. Carlson. A controllable squeeze film damper using magnetorheological fluid. In *Proceedings of Actuator 96*, pages 333–336, Bremen, Germany, 1996.

M.R. Jolly, J.W. Bender, and J.D. Carlson. Properties and applications of commercial magnetorheological fluids. In *Proceedings of SPIE 5th International Symposium on Smart Structures and Materials*, San Diego, California, 1998.

M.R. Jolly, R.H. Majoram, S. Koester, and K.A. St Clair. Brake with field responsive material. US patent 6,854,573, 2005.

I.A. Kapandji. *Physiologie Articulaire*. Maloine S.A. Editeur, 1980.

B. Kavlicoglu, F. Gordaninejad, C. Evrensel, A. FUchs, and G. Korol. A semi-active, high torque, magnetorheological fluid limited slip differential clutch. *Journal of Vibration and Acoustics*, 128:604–610, 2006.

C. Kieburg. MR all-wheel-drive prototype car driving tests and durability requierements for the MR fluids used. In *Proceedings of ERMR'08*, Dresden, Germany, 2008.

T. Kikuchi, J. Furusho, and K. Oda. Development of isokinetic exercise machine using ER brake. In *Proceedings of the IEEE International Conference on Robotics and Automation*, pages 214–219, Taipei, Taiwan, 2003.

J-H. Koo, F.D. Goncalves, and M. Ahmadian. A comprehensive analysis of the response time of MR dampers. *Smart Materials and Structures*, 15:351–358, 2006.

W.I. Kordonski, S.R. Gorodkin, and Z.A. Novikova. The influence of ferroparticle concentration and size on MR-fluid properties. In *Proceedings of the 6th ERMR Conference*, pages 532–542, Yonezawa, Japan, 1997.

R. Krukowski. Particle brake clutch muscle exercise and rehabilitation apparatus. US patent 4,765,315, 1988.

K. Kulig, J.G. Andrews, and J.G. Hay. *Exercise and Sport Science Reviews*, volume 12, pages 417–466. Macmillan, 1984.

D. Lampe and R. Grundmann. Transitional and solid state behaviour of a magnetorheological clutch. In *Proceedings of Actuator 2000*, 2000.

H. M. Laun, G. Schmidt, and C. Gabriel. Reliable plate-plate MRF magnetorheometry based on validated radial magnetic flux density profile simulations. *Reologica Acta*, 47(9):1049–1059, 2008.

E. Leclerq. Etude isocinétique de l'articulation du poignet et dynamométrie manuelle. Master's thesis, Université Libre de Bruxelles, 1999.

P. Letier, M. Avraam, M. Horodinca, A. Schiele, and A. Preumont. Survey of actuation technologies for body-grounded exoskeletons. In *Proceedings of Eurohaptics*, Paris, France, 2006.

P. Letier, M. Avraam, S. Veillerette, M. Horodinca, and A. Preumont. SAM : A 7-DOF portable arm exoskeleton with local joint control. In *Proceedings of IEEE IROS 08*, Nice, France, 2008.

W.H. Li and H. Du. Design and experimental evaluation of a magnetorheological brake. *International Journal of Advanced Manufacturing Technology*, 21:508–515, 2003.

B. Liu, W.H. Li, P.B. Kosasih, and X.Z. Zhang. Development of an MR-brake-based haptic device. *Smart Material and Structures*, 15:1960–1966, 2006.

LORD. *Engineering Note - Designing with MR-Fluids*. LORD, 1998.

R.W. Lovett and E.G. Martin. Certain aspects of infantile paralysis with a description of a method of muscle testing. *Journal of the American Medical Association*, 66:729–733, 1916.

N. Lucchesi. *Analisi e Progettazione Di un Nuovo Sistema Dattuazione Per Interfacce Aptiche a Più Gradi Di Libertà*. PhD thesis, Universita Degli Studi di Pisa, 2004.

R.J. Marley and M.R. Thomson. Isokinetic strength characteristics in wrist flexion and extension. *International Journal of Industrial Ergonomics*, 25:633–643, 2000.

C. Mavroidis, J. Nikitczuk, B. Weinberg, G. Danaher, K. Jensen, P. Pelletier, J. Prugnarola, R. Stuart, R. Arango, M. Leahey, R. Pavone, A. Provo, and D. Yasevac. Smart portable rehabilitation devices. *Journal of NeuroEngineering and Rehabilitation*, 2(18), 2005.

I.D. Mayergoyz. Dynamic preisach models of hysteresis. *IEEE Transactions on Magnetics*, 24(6):2925–2927, 1988.

Y-J. Nam, Y-J. Moon, and M-K Park. Performance improvement of a rotary MR fluid actuator based on electromagnetic design. *Journal of Intelligent Material Systems and Structures*, 00:1–11, 2007.

J. Nikitczuk, B. Weinberg, and C. Mavroidis. Control of electro-rheological fluid based resistive torque elements for use in active rehabilitation devices. *Smart Materials and Structures*, 16:418–428, 2007.

OSSUR. Rheoknee product datasheet.

L.R. Osternig. *Isokinetics in Human Performance*, chapter 4: Assessing human performance, pages 77–96. Human Kinetics, 2000.

D.H. Perrin. *Isokinetic Exercise and Assessment*. Human Kinetics Publishers, 1993.

R.W. Phillips. *Engineering Applications of Fluids with a Variable Yield Stress*. PhD thesis, University of California, Berkeley, 1969.

S. Poulis, R. Rapanakis, X. Pastra, I. Poulis, and R.W. Soames. Force-velocity relationship of the wrist flexors and extensors: The influense of small and large handgrips. *Isokinetics and exercise science*, 11:101–108, 2003.

J. Rabinow. The magnetic fluid clutch. *American Institute of Electrical Engineers Transactions*, 67:1308–1315, 1948.

J. Rabinow. Magnetic fluid torque and force transmitting device. US patent 2,575,360, 1951.

M. R. Reed. Development of an improved dissipative passive haptic display. Master's thesis, Georgia Institute of Technology, 2003.

P.M. Rothwell. Analysis of agreement between measurement of continuous variables: General principles and lessons from studies of imaging of carotid stenosis. *Journal of Neurology*, 415:825–834, 2000.

A.A. Sapega. Muscle performance evaluation in orthopaedic practice. *Journal of Bone and Joint Surgery*, 72:1562–1574, 1990.

B. Sapinski and S. Bydon. Application of magnetorheological fluid brake to shaft position control in induction motor. In *AMAS Workshop on Smart Materials and Structures*, pages 169–180, Jadwisin, 2003.

A.L. Smith, J.C. Ulicny, and L.C. Kennedy. Magnetorheological fluid fan drive for trucks. *Journal of Intelligent Material Systems and Structures*, 18:1131–1136, 2007.

B.F. Spencer, S.J. Dyke, M.K. Sain, and J.D. Carlson. Phenomenological model of a magnetorheological damper. *ASCE Journal of Engineering Mechanics*, 123(3):230–238, 1997.

J.L. Sproston, L.C. Yanyo, J.D. Carlson, and A.K. El Wahed. Controllable fluids in 2002 - status of ER and MR fluid technology. In *Proceedings of Actuator '02*, pages 333–338, Bremen, Germany, 2002.

R. Stanway, J.L. Sproston, and N.G. Stevens. Non-linear modelling of an electro-rheological vibration damper. *Journal of Electrostatics*, 20:167–184, 1987.

N. Takesue, J. Furusho, and Y. Kiyota. Analytic and experimental study on fast response MR-fluid actuator. In *Proceedings of the IEEE Int. Conf. On Robotics and Automation 2003*, pages 202–207, Tapei, Taiwan, 2003.

H. Thistle, H. Hislop, M. Moffroid, and E. Lohman. Isokinetic contraction: A new concept of resistive exercise. *Archives of physical medecine and contraction*, 48:279–282, 1967.

J.M. Vanswearingen. Measuring wrist muscle strength. *Journal of Orthopaedic and Sport Physical Therapy*, 4:217–228, 1983.

H. Wang, X.L. Gong, Y.S. Zhu, and P.Q. Zhang. A route to design rotary magnetorheological dampers. In *Proceedings of the Ninth International Conference on Electrorheological Fluids and Magnetorheological Suspensions*, pages 680–686, Beijing, China, 2004.

G.M. Webb. Exercise apparatus and associated method including rheological fluid brake. US patent 5,810,696, 1998.

K.D. Weiss, J.D. Carlson, and D.A. Nixon. Method and magnetorheological fluid formulations for increasing the output of a magnetorheological fluid device. US patent 5,900,184, 1999.

Y.K. Wen. Method of random vibration of hysteretic systems. *Journal of Engineering Mechanics Division 102*, pages 249–263, 1976.

W.M. Winslow. Induced fibration of suspensions. *Journal of Applied Physics*, 20:1137–1140, 1949.

D.A. Winter, R.P. Wells, and G.W. Orr. Errors in the use of isokinetic dynamometers. *European Journal of Applied Physiology*, 46:397–408, 1981.

K.S. Wong and W.H. Liao. Adaptive body fitness equipment using magnetorheological fluids. In *Proceedings of the IEEE International Conference on Robotics and Biomimetics*, pages 432–437, 2005.

T. Wrigley and M. Grant. *Sports Physiotherapy - Applied Science and Practice*, chapter 17: Isokinetic Dynamometry, pages 259–283. Churchill Livingstone, 1995.

Y. Yamaguchi, J. Furusho, K. Koyanagi, and S. Kimura. Development of a 2-d force display system using MR actuators. In *Proceedings of ICAT 2003*, Tokyo, Japan, 2003.

G. Yang, B.F. Spencer, J.D. Carlson, and M.K. Sain. Large-scale MR fluid dampers: Modeling and dynamic performance considerations. *Engineering Structures*, 24(3):309–323, 2002.

S. Ye and K. A. Williams. Torsional friction damper optimization. *Journal of Sound and Vibration*, 294:529–546, 2006.

T.M. York, C.D. Gilmore, and T.G. Libertiny. Magnetorheological fluid coupling device and torque load simulator system. US patent 5,598,908, 1997.